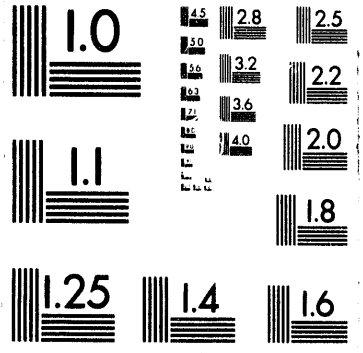
1.0
1.1
1.25
1.4
1.6
1.8
2.0
2.2
2.5
2.8
3.2
3.6
4.0
4.5
5.0
5.6
6.3

1 of 2

NORTHWESTERN UNIVERSITY

THE dE/dx CAPABILITIES OF THE DØ TRACKING SYSTEM

A DISSERTATION

SUBMITTED TO THE GRADUATE SCHOOL
IN PARTIAL FULFILLMENT OF THE REQUIREMENTS

for the degree

DOCTOR OF PHILOSOPHY

Field of Physics and Astronomy

By

SRINIVASAN RAJAGOPALAN

EVANSTON, ILLINOIS

June 1992

AC02-76CH03000

ABSTRACT

THE dE/dx CAPABILITIES OF THE DØ TRACKING SYSTEM

Srinivasan Rajagopalan

The DØ forward tracking system has been extensively calibrated using electron and pion beams in the energy range from 10 GeV to 150 GeV in the neutrino area fixed target beam line at Fermilab. The forward tracking system provides a spatial resolution of 200 μm and a two hit separation of 2.5 mm at 90% efficiency. The chamber provides 32 samples of pulse height information for a given track equivalent to a dE/dx resolution of 12.7%. The energy loss response of the chamber to low energy beam has been studied. A Monte Carlo simulation program has been developed based on the Photo Absorption Ionization model to simulate the dE/dx response of the chamber. The observations made using low energy test beam are consistent with the model's predictions. The dE/dx measurement in the DØ tracking system provides identification of electrons against gamma conversions resulting from π^0 decays. The rejection factor of distinguishing doubly minimum ionizing tracks in the chamber has been measured to be 30.5 with the requirement that singly minimum ionizing tracks be identified with a 90% efficiency. This factor improves with lower multiplicity. Using a Monte Carlo program based on GEANT, the identification efficiency of electrons and π^0's has been determined. Using the capabilities of the outer tracking system alone, the background due to isolated π^0 production is reduced by up to a factor of 60 in the central direction based on measurements made on a sample of simulated QCD two jet events.

ACKNOWLEDGEMENTS

First, I must thank all the members of the DØ collaboration. Their coordinated effort and persistence during the last nine years led us through a successful construction and installation phase to deliver a unique detector with excellent physics potential.

The Northwestern University group is responsible for the design, construction, calibration and operation of the Forward Drift Chamber. I thank Rob Avery, Jeff Bantly and Sue Blessing who have put up a tremendous effort in understanding the chamber and who were very quick in suggesting and implementing improvements. I thank Yi Cheng Liu, the most recent member of our group, for his invaluable contributions during a critical phase of the experiment. I owe a special thanks to Bruno Gobbi from whom I have learnt a great deal. His expertise and superb hardware skills made it possible for us to deliver an excellent chamber. His strong persistence and motivation helped us solve many problems and accept many new challenges. I owe a great debt to my advisor, Dave Buchholz, for his excellent guidance and encouragement throughout my graduate career. He has helped me through much of my analysis and has shared much of his knowledge not only in high energy physics, but also in everyday practical applications. His painstaking efforts in coordinating tasks inside and outside our group has helped prepare us for the collider run. I am indebted to him for his teachings and am very fortunate to have had him as my advisor.

I would again like to especially thank both Dave and Bruno for not only guiding

me in my research, but also for their immense support outside the laboratory during difficult times. I am very appreciative for their understanding and support and it has been a pleasure to have had the opportunity to work with them.

I am grateful to all the people at Fermilab who helped us in calibrating our chamber at the Fixed target experimental area. I thank Dan Owen and the members of the calorimeter group for coordinating their efforts with ours. I thank Herman Haggerty for setting us up with a photon beam which helped us in studying conversions. Many thanks to Mike Tartaglia (aka DrMikie) for his assistance with trigger and beam line operations. Marvin Johnson and his technical support crew deserve a big thanks for providing invaluable support with the electronics both at DØ and at the fixed target area.

The successful installation of the Forward Drift Chamber in the collision hall along with the other subdetectors was made possible by many people, far too many to list. I thank all of them. I thank John Featherly, Paul Russo and Kurt Ruthmansdorfer for their extensive support with the computing systems at DØ. A special thanks to the 'GEEKS' and the mentors for their tireless efforts in debugging and maintaining a working data acquisition system through unstable periods. I thank all my friends for their ideas, criticisms and help, (Jim Cochran *et al.*), from whom I have learnt a lot through informal discussions.

Finally, I wish to dedicate this thesis to my parents whose encouragement and strong support allowed me to successfully complete a degree in high energy physics. I take this opportunity to thank them for all the care and attention they have provided me through my life. I thank my brother and my sisters for their support.

Contents

List of Tables

List of Figures

Chapter 1
Introduction

"Armed with giant machines and grand ambitions, physicists spend billions in the race to discover the building blocks of matter" [1].

Since the discovery of the electron by J.J. Thomson, matter has been constantly probed to identify the basic building blocks and the forces that act upon them. The successful observation of the neutron by Chadwick led to a more detailed picture of the atomic nucleus consisting of protons and neutrons. Elastic scattering of electrons from protons in 1963 further revealed that a proton has a well defined structure. In 1964, Gell-Mann [2] proposed a theory that the nucleon is made up of three fractionally charged fermions called quarks and that the mesons are quark-antiquark bound states. With the advent of newer technology, high energy accelerators and particle detectors have further probed into matter revealing a multitude of quark bound states. This necessitated the need to have a framework which provided an understanding of the detailed structure of matter and the forces that play upon it.

The standard model [3], describing the interaction of a finite set of spin $\frac{1}{2}$ fermions mediated by spin 1 gauge bosons, provides the most satisfactory framework for all experimentally observed phenomena in high energy physics today. This finite set of fermions consists of the charged leptons, their associated neutrinos, and six flavours of quarks, each flavour coming in three colours. The family of quarks

and leptons are each arranged into three generations forming doublets. Ignoring gravitational effects, the interactions between the fermions are described by three symmetry groups. The gauge symmetry group U(1) describes the electromagnetic interaction (QED), SU(2) the weak interaction and SU(3) the strong interaction (QCD). The quarks participate in all three interactions while the leptons participate only in electromagnetic and weak interaction. Due to the parity violating nature of weak interactions which accounts for its V-A structure, only the left handed components form doublets consisting of the lepton and its corresponding neutrino. The right handed charged leptons are singlets with respect to weak interaction.

The three interactions described above are mediated by the photon, the intermediate vector gauge bosons and the gluons respectively. The photon and the gluons are massless while the vector gauge bosons acquire mass through the Higgs mechanism. An introduction of a complex scalar doublet Higgs field with a non zero vacuum expectation value spontaneously breaks the SU(2) symmetry. This is necessary in order for the vector bosons to acquire mass which is proportional to the vacuum expectation value. The minimal SU(2)⊗U(1) electroweak theory based on the Higgs field predicted [4] the existence of massive gauge bosons which were subsequently discovered at the CERN $Sp\bar{p}S$ collider in 1982 [5] [6]. Based on this theory, the electroweak force is mediated by four vector gauge bosons, γ, W^+, W^- and Z^0. The left handed fermions which form doublets and the right handed singlets are characterized by weak isospin and weak hypercharge quantum numbers. The U(1) symmetry is a linear combination of the U(1) weak hypercharge and the SU(2) weak isospin. The coupling strength of the two gauge symmetries are related by a

single parameter, Θ_W, the weak mixing angle. The model's prediction for the masses M_W and M_Z of the gauge boson is expressed in terms of the coupling strengths and the mixing angle as [7]

$$M_W = \left[\frac{\pi\alpha}{\sqrt{2}G_F sin^2\Theta_W(1-\Delta r)}\right]^{\frac{1}{2}} \tag{1.1}$$

$$M_Z = M_W/cos(\Theta_W) \tag{1.2}$$

where α and G_F are the fine structure and the Fermi constant respectively and are proportional to the squares of the coupling strengths. Δr denotes the radiative corrections [7]. Equation 1.2 is exact under the minimal standard model assumptions. A precise mass measurement would therefore test the minimal Higgs mechanism and could signal the need for a more complex Higgs mechanism. This is characterized by the ρ parameter as

$$\rho = \frac{M_W^2}{M_Z^2 cos^2\theta_W} \tag{1.3}$$

where $\rho = 1$ in the minimal Higgs model. The $O(\alpha)$ one loop corrections to Δr arise primarily due to vacuum polarization effects. The two loop [8] contributions to Δr include the top quark loop, QCD corrections and a Higgs loop and thus depends on the top quark and the Higgs mass. A precise measurement of the masses and thus Δr would test the existing model predictions. A large difference in the measured value of Δr against the predicted value may signify a need for further additional terms to the radiative correction possibly arising from a fourth generation of quarks.

1.1 Precision measurements of IVB masses

The precise mass measurement of the intermediate vector gauge bosons provides a direct test to the standard model. The W and Z bosons decay predominantly into $q\bar{q}$ final states which fragment giving rise to observable jets in the detector. The boson masses are inferred from the two jet mass spectrum. The main background contribution to this decay channel arise from QCD processes which also give rise to two jet final states. The QCD background exceeds the signal by two orders of magnitude. This yields a two jet mass resolution of the order of the mass difference between the W and Z boson masses. Thus the expected two peaks in the two jet mass spectrum due to the W and Z bosons cannot be clearly identified. Due to the large QCD background, the precision mass measurements are carried out by exploring the leptonic decay modes of the W and Z boson. Though the hadronic channel provides poor mass resolution, the multi jet mass spectrum provides a tool to search for new particles such as heavy vector bosons and test the standard model.

The leptonic decay mode of the W boson involves the observation of a high P_T lepton, where P_T is the transverse momentum, and a large missing P_T indicating the presence of a neutrino. Since the neutrino is not directly observed, its transverse momentum and direction is calculated by measuring the momentum imbalance in the detector. The transverse mass of the W boson is then calculated using the equation

$$M_{W_t}{}^2 = 2P_T(l)P_T(\nu)(1 - cos\theta_{l\nu}) \tag{1.4}$$

where $\theta_{l\nu}$ is the angle between the transverse momentum vectors of the lepton and

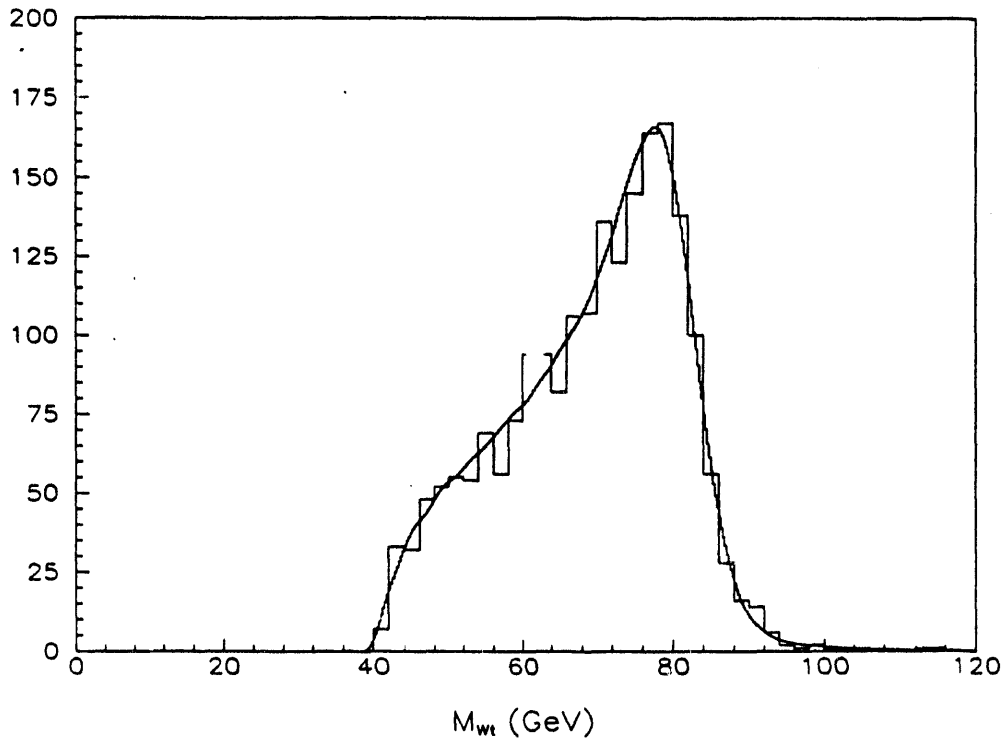

Figure 1. Transverse mass spectrum of the W boson from UA2 measurements.

the neutrino. Figure 1 shows the transverse mass distribution of the W boson for the electron channel observed at the CERN $p\bar{p}$ collider at UA2 [9]. The distribution is Jacobian having a sharp cut off at the mass value predicted by the standard model. The mass of the W boson is calculated using a Monte Carlo simulation of the detector. For a given value of M_W and the width Γ_W of the W, the transverse mass spectrum can be inferred from the Monte Carlo simulation. A three dimensional array of M_{W_t}, M_W and Γ_W is constructed which provides a continuous function representing the probability of observing a given value of M_{W_t} for the input parameters M_W and Γ_W. Using a maximum likelihood method, the value of M_W is determined by computing the product of the likelihood values for each event in the

Table 1.–Current status of electroweak parameters.

Parameter	Value	Experiment	Standard Model[a]
M_Z (GeV)	91.175 ± 0.021	LEP	input
Γ_Z (GeV)	2.487 ± 0.009	LEP	2.485 ± 0.0083
$\Gamma_{l\bar{l}}$ (MeV)	83.3 ± 0.4	LEP	83.5 ± 0.224
Γ_{had} (GeV)	1.744 ± 0.01	LEP	1.735 ± 0.006
$\Gamma_{had}/\Gamma_{l\bar{l}}$ (GeV)	20.94 ± 0.12	LEP	20.78 ± 0.016
Γ_{inv} (MeV)	493 ± 10	LEP	499.4 ± 1.34
N_ν	2.97 ± 0.0281	LEP	3.0
M_W (GeV)[b]	80.14 ± 0.27	CDF+UA2	80.05 ± 0.2
M_W/M_Z	0.8813 ± 0.0021	UA2	0.878 ± 0.0022
$sin^2\theta_W$	0.2274 ± 0.0052	CDF+UA2	0.232 ± 0.001

[a]The minimal standard model parameters are computed using the LEP Z^0 mass and with the assumption that 50 GeV < M_{Higgs} < 1 TeV.

[b]The W mass has been scaled to the Z^0 mass observed at LEP.

W sample [10].

The masses of the $W^\pm$ and the Z^0 boson have been measured by UA2 [9] and CDF [11] at CERN and Fermilab Tevatron respectively. The UA2 observed masses of the W are scaled with the measurement of the Z^0 at the Large Electron Positron collider (LEP) which operates at the Z^0 resonance and thus provides a more accurate measurement of the Z^0. The current experimentally measured values of the electroweak parameters are consistent with the standard model predictions and are shown in Table 1 [13]. The largest systematic uncertainties in the mass measurements arise from the electron energy resolution and the missing E_T resolution

Table 2.–Uncertainty in the W mass measurement.

Category	DØ[a] 5 pb^{-1}	CDF 5 pb^{-1}	UA2 13 pb^{-1}	DØ[a] 25 pb^{-1}
Statistics	250	350	330	110
Energy scale	250	190	810[b]	70
Resolution	150	230	130	60
Structure function	60	60	85	60
Background	50	50	45	25
Overall	400	465	370	160

[a] The values quoted for DØ have been predicted for an integrated luminosity of 5 pb^{-1} and scaled for 25 pb^{-1}.

[b] The W mass measurement has been scaled to the LEP Z^0 mass thus cancelling the effect of the energy scale. The overall UA2 uncertainty does not include the scale error.

contributing to a mismeasurement of the electron and neutrino transverse momentum respectively. Other systematic error contributions include lack of knowledge of the correct parton structure functions adopted in the Monte Carlo. Table 2 lists the uncertainties of the various categories contributing to the error in the W transverse mass measurement for UA2 and CDF. The DØ values for the same categories [12] are listed for 5 pb^{-1} and 25 pb^{-1} integrated luminosity. Statistical errors and resolution have been scaled as the square root of the integrated luminosity for the values quoted for 25 pb^{-1}.

Using the LEP Z^0 mass measurement and a precise W boson measurement at the Tevatron collider, the allowed mass range of the top quark can be narrowed.

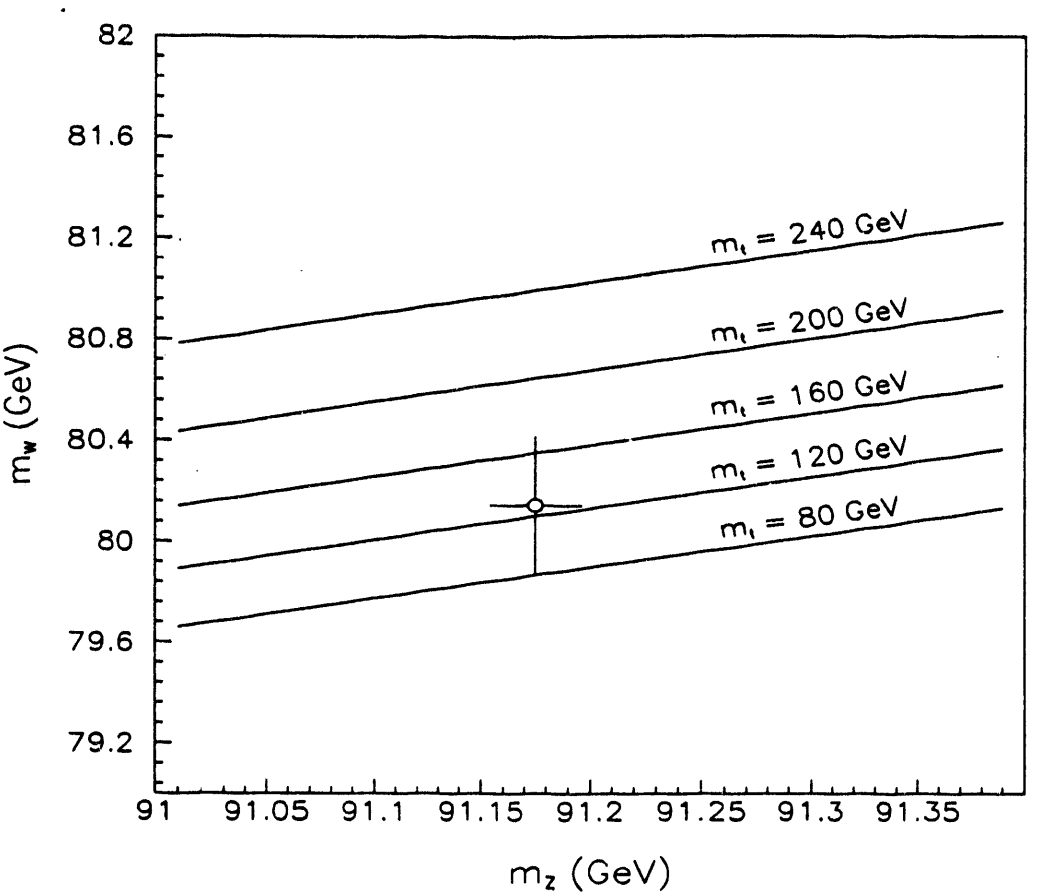

Figure 2. Dependence of M_W on M_Z for top quark mass between 80 and 240 GeV and a Higgs mass of 100 GeV. The error on the M_W are from the combined result of UA2 and CDF.

In the event the top quark is found and its mass measured to within a few GeV, the precise W measurement can be used to narrow the allowed range of the Higgs mass. Figure 2 shows the theoretically predicted dependence [14] of the mass of the W and the Z boson for various value of the top mass and a Higgs mass of 100 GeV. The error bars on the Z^0 mass are obtained from LEP results while the errors on the W mass are from the combined result of the UA2 and CDF. The bounds on the

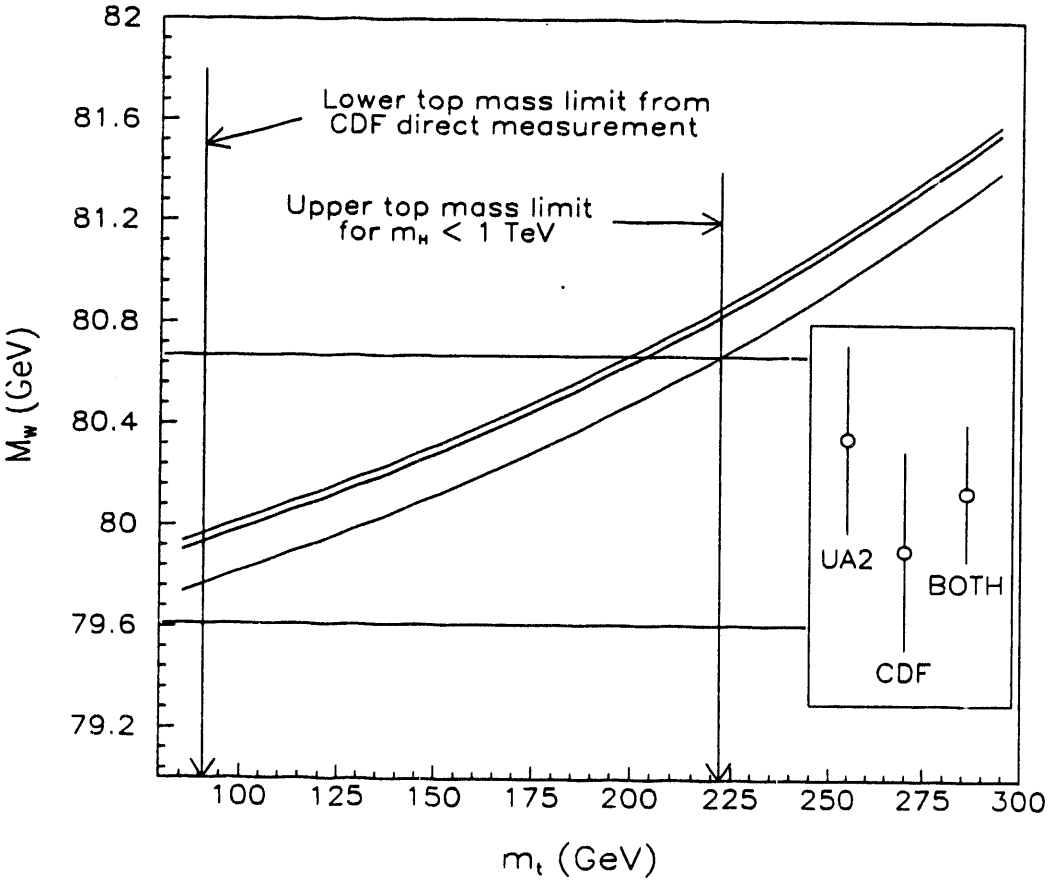

Figure 3. Standard model dependence of M_W on the top quark mass for a Higgs mass of 50, 100 and 1000 GeV (top, middle, bottom curve respectively) and M_Z = 91.175 GeV (LEP).

top quark mass for a Higgs mass of 100 GeV at 95% confidence level is 130 ± 50 GeV and is consistent with the standard model. Assuming the LEP result on the Z^0 mass, Figure 3 shows the mass of the W boson as a function of the top mass for a Higgs mass of 50, 100 and 1000 GeV [14]. The inset box shows the measured mass at UA2, CDF and the combined measurement with 1-sigma error bars. The horizontal lines shown are the range of the W mass at the 95% confidence level from the combined measurement of CDF and UA2. This sets the upper limit on the top

mass at 222 GeV for a Higgs mass below 1 TeV. The unitarity limit in the WW scattering amplitude places an upper limit on the Higgs mass at 1.2 TeV. A direct decay channel of the top quark by CDF [15] led to the quoted lower mass limit of 91.0 GeV.

1.2 Direct observation of the top

Direct searches for top quark decay have been extensively carried out at UA2, LEP and CDF which have led to the current lower limit of 91 GeV at 95% CL. Thus the decay of a real W into a top quark has been ruled out. Above the W mass, the $t\bar{t}$ production cross section dominates and the top quark primarily decays into a b quark and a virtual or real W with standard model assumptions. Non standard decays of the top quark into a charged Higgs or a fourth generation b$'$ quark if it is lighter than the top quark are conceivable.

The $t\bar{t}$ production and subsequent decay will result in two W's and two b jets, where each of the W's can decay either leptonically or hadronically. Therefore there are three possible final states:

1) Both the W's decay hadronically.

2) One of the W's decays hadronically and the other leptonically.

3) Both W's give rise to final lepton states.

Table 3 lists the branching ratios and cross sections for each of the final states for top quark masses of 100, 120 and 140 GeV.

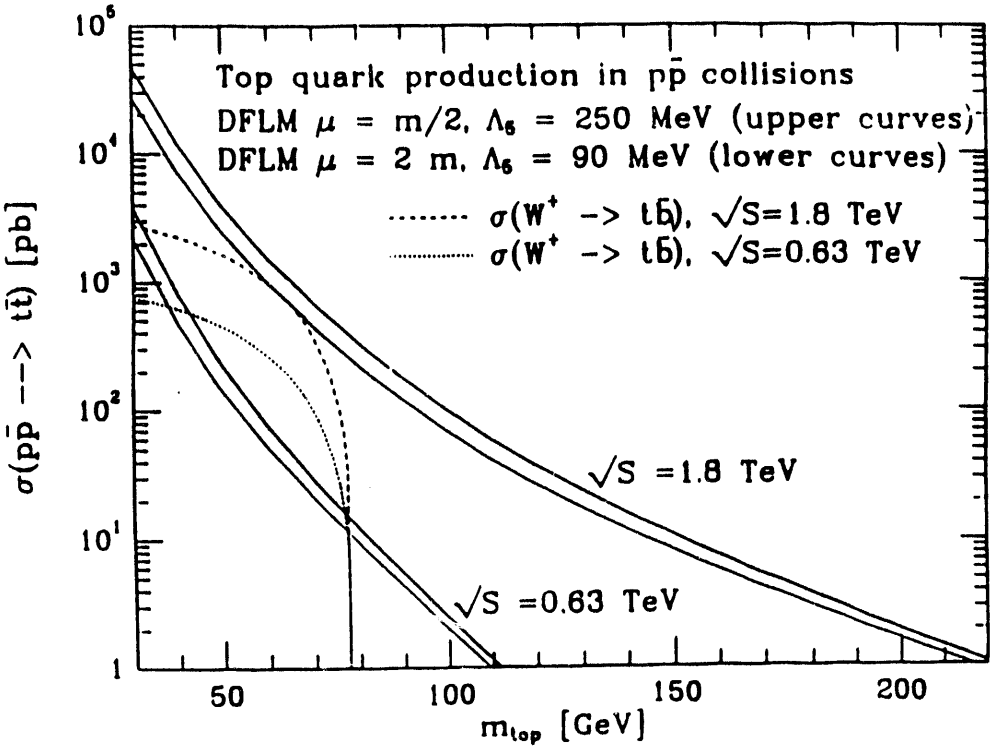

Figure 4. $t\bar{t}$ production cross section in $p\bar{p}$ collisions at CERN and Tevatron energies. The pair of curves at each energy reflect the upper and lower theoretical predictions.

Table 3.–$t\bar{t}$ production cross section at $\sqrt{s}$ = 1.8 TeV.

Decay mode[a]	Branching Ratio	Production Cross section (pb) m_t=100	m_t=120	m_t=140
$t\bar{t} \rightarrow q\bar{q}bq\bar{q}b$	$\frac{36}{81}$	39.24	15.02	6.58
$t\bar{t} \rightarrow l_i\nu bq\bar{q}b$	$3 \times \frac{12}{81}$	13.08	5.0	2.193
$t\bar{t} \rightarrow l_i\nu bl_j\nu b$	$3 \times \frac{2}{81}$	2.18	0.835	0.365
$t\bar{t} \rightarrow l_i\nu bl_i\nu b$	$3 \times \frac{1}{81}$	1.09	0.417	0.183
Total cross section	-	88.3	33.8	14.8

[a]The subscripts i and j refer to the leptons = (e,μ,τ); i $\neq$ j.

Though the cross section of the pure multijet decay mode of the top is the largest, it is dominated by the large QCD multijet background. The lepton-multijet decay channel of the top gives rise to one or more high P_T leptons, missing energy and multiple jets from W and b decay. Additionally there is an underlying event contribution. The primary background for the lepton-multijet channel arises from W + multijet production. A possible technique to reduce the background is to compute the jet-jet mass spectrum and require high E_T jets above 20 GeV [16]. Since the W-jets from $t\bar{t}$ production are more energetic, a high jet E_T cut reduces the background substantially to show the presence of the top signal. However, for a top mass much larger than the W, the higher jet multiplicity worsens the signal to background ratio and making this channel difficult for an observation. A tagged b-jet provides another possible identification technique for this channel although for a low top mass, the b-jets have a low P_T which reduces the signal to background ratio due to inefficient jet reconstruction.

The dilepton decay channel of the top has the lowest cross section but provides the cleanest signature. The channel gives two high P_T leptons and additional jets from b and underlying QCD radiation. In addition, large missing energy could possibly be observed from two undetected neutrinos. This is not a necessary observation especially in the case when the two neutrinos are back to back which cancel out to give a small observed missing E_T. The main backgrounds to the dilepton channel are from the Drell Yan processes and $b\bar{b}$, $c\bar{c}$ hadroproduction. For like leptonic final states (ee, $\mu\mu$ or $\tau\tau$), additional backgrounds arise from Z^0 decays to l^+l^-. The effect of the background can be strongly reduced by requiring two high P_T isolated

leptons each greater than 15 GeV, a high P_T jet and a P_T imbalance of greater than 20 GeV seen in the detector [17]. Z^0 decays can be reduced by cutting on the azimuth angle between the two leptons and possibly the invariant mass of two leptons, $m_{l^+l^-}$. Backgrounds due to $b\bar{b}$ and $c\bar{c}$ hadroproduction can be reduced by requiring isolated leptons and constraining the azimuth angle between the two leptons. It must however be noted that the above cuts are applicable only on a sample containing a large number of top candidate events. As seen from Table 3, only a handful of top candidate events are expected to be produced for a top mass of 120 GeV and an integrated luminosity of 25 pb^{-1}. Thus the signal may be completely wiped out by using the above indicated cuts. The approach which will be used for the initial discovery of the top with the current Tevatron luminosity is to extract a sample of possible top candidate events using minimal cuts and analyze these on an event by event basis.

Studies of backgrounds have been extensively carried out at DØ for the dilepton channel [18] using ISAJET [19]. From this study, $t\bar{t}$ production cross section and the cross section of contributing background sources have been computed using ISAJET before and after cuts for the three dilepton channels. The cuts applied required the P_T of the two highest leptons to be greater than 15 and 10 GeV respectively and required the leptons to be in the acceptance range $|\eta_e| < 2.2$, $|\eta_\mu| < 1.7$. These cuts substantially reduce the background and keep 80% of the real signal. This is illustrated in Figure 5 which shows the effect of the QCD background on the $e\mu$ channel before and after cuts for three possible top masses. The backgrounds are expected to be reduced further by requiring isolated leptons, constraining the angle

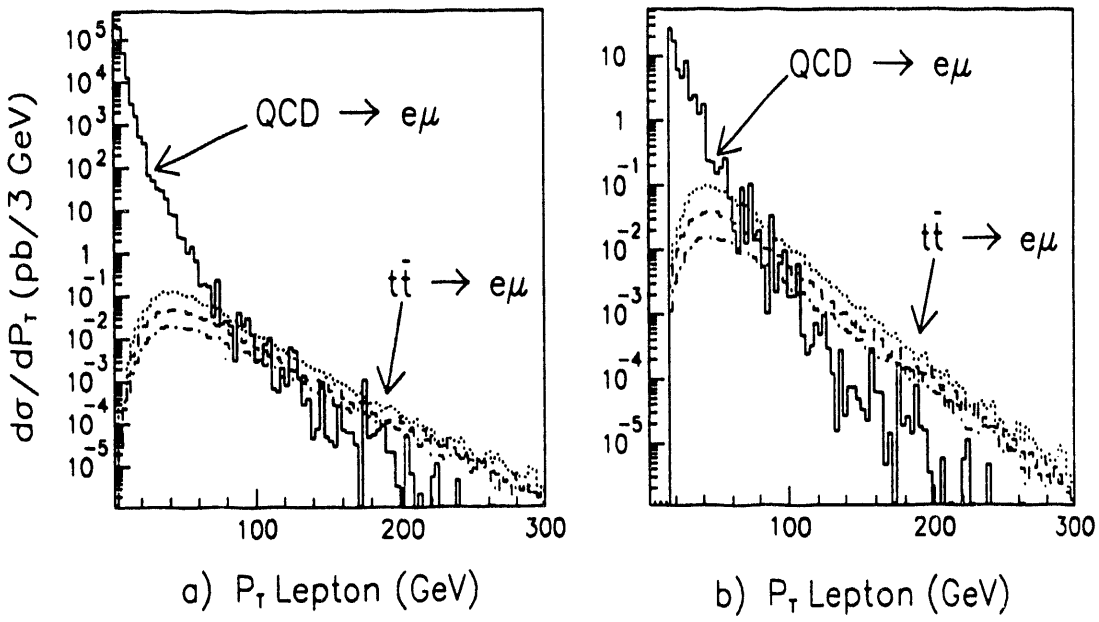

Figure 5. Cross section distribution of $t\bar{t} \rightarrow e\mu$ with QCD background before(a) and after(b) P_T cuts for top mass of 100, 120 and 140 GeV.

between the two leptons, requiring a large missing energy and possible reconstruction of the b-jet.

1.3 Lepton identification

The precision measurements described above require excellent lepton identification. The DØ detector provides almost 4π muon coverage and a highly segmented uranium liquid argon calorimeter for electron identification. Further improvements in the electron identification are provided by a transition radiation detector in the central region. The backgrounds to the electron identification mainly come from π^0 production which decays into two gammas. The tracking chambers are used to provide a rejection against π^0 background. Gammas resulting from π^0 decay which

do not convert before the calorimeter can be easily identified in the tracking chamber with an absence of a track. For those gammas which do convert, the e^+e^- pair overlap in space due to the absence of a central magnetic field. The energy loss in the tracking chambers due to e^+e^- pairs will therefore be twice the energy lost by a single charged particle. Thus gammas that convert can be identified by measuring the energy loss. In the following chapters, the performance of the tracking systems and their energy loss response will be discussed which will aid the calorimeter and the muon systems in providing good lepton identification.

Chapter 2
The Detector

The DØ detector [20] has been constructed to investigate $p\bar{p}$ interactions at the Fermilab Tevatron. This chapter will describe the detector components and the data acquisition system used to read out the detector.

The detector, shown in Figure 7 , has been designed with specific characteristics aimed at studying high P_t physics. This requires a good measurement of leptons, jets and missing energy. The DØ detector does not have a central magnetic field which allows for a compact highly segmented calorimeter with the above properties. Lepton identification is achieved with a liquid argon calorimeter, transition radiation detector and tracking system to reject backgrounds arising from gamma conversions. Additionally, muons are identified by their penetration through the calorimeter and magnetized steel. Muon coverage extends from $\Theta = 3$ degrees with respect to the beam axis. A good hadron energy resolution with a roughly equal response to both electrons and pions ($e/\pi \approx 1$) is achieved using a liquid argon uranium calorimeter. The calorimeter has been designed to emphasize coverage close to the beam axis and to minimize cracks to provide good measurement of missing transverse energy.

Table 4.–Tevatron parameters.

Main Ring/Tevatron radius	1 km
Peak beam energy	900 GeV
Injection energy	150 GeV
Luminosity	$1 \times 10^{30} cm^2 sec^{-1}$
Intensity per bunch	6×10^6 p, 2×10^6 $\bar{p}$
Number of bunches	6
Crossing angle	0°
Beam emmitance	24π mm mr
Acceleration period	44 seconds
Bunch length	50 cm
Beam radius	$43 \times 10^{-6} m$
Energy spread	0.15×10^{-3}
RF frequency	53 MHz

2.1 The Beam

Protons and antiprotons collide at the DØ interaction region at a centre of mass energy of 1.8 TeV. The main characteristics of the Fermilab Tevatron collider [21] are summarized in Table 4. A brief description of the various stages required to accelerate each of the proton and antiproton beam to 900 GeV is given below.

The first stage uses H^- ions which are released in a Cockroft Walton accelerator. The H^- ions are accelerated to 750 keV. These are then sent through a 150-metre long, 200 MeV linear accelerator which injects these into a booster synchrotron. At the entrance of the booster, a carbon foil is used to strip away the electrons from the H^- ions. The resultant protons are accelerated in the booster to an energy

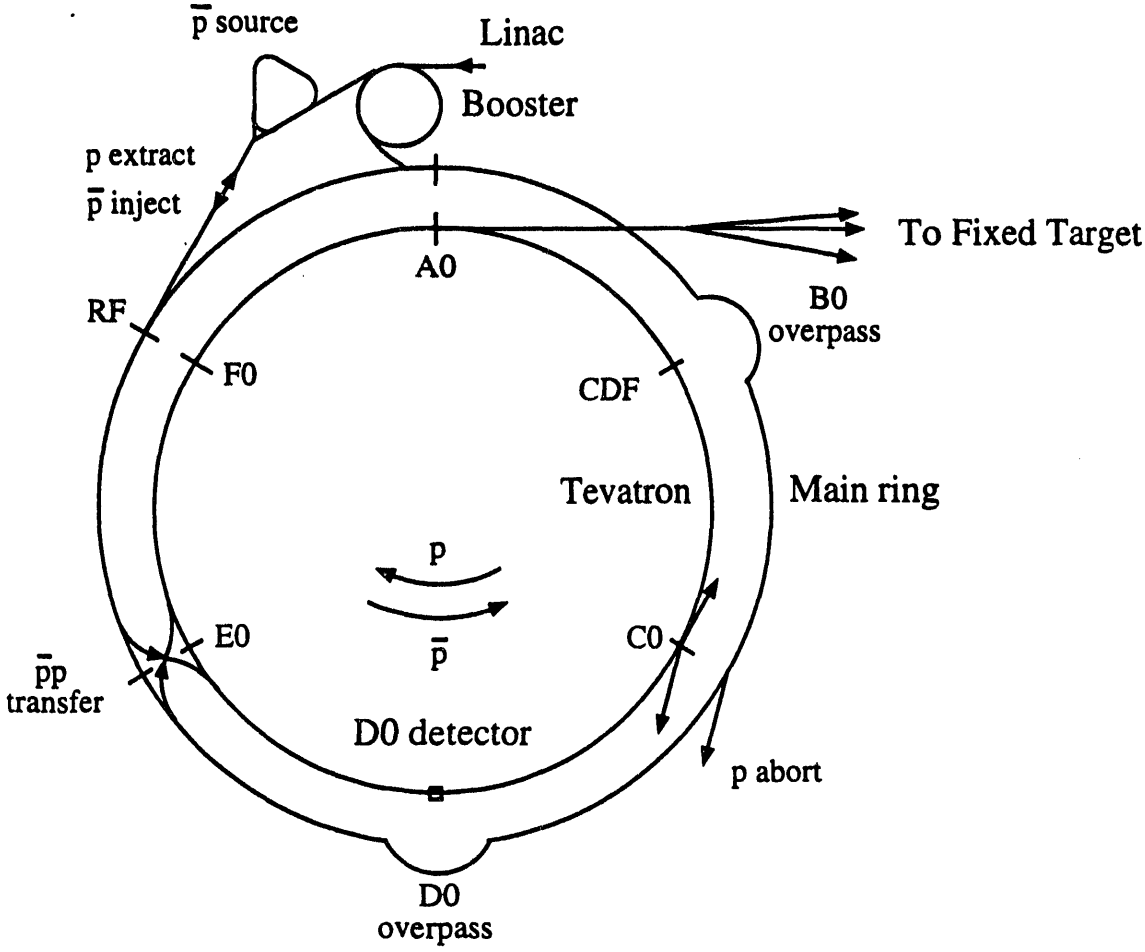

Figure 6. The Fermilab Tevatron and the location of the DØ detector.

of 8 GeV. The protons are then injected into the Main ring accelerator which accelerates the beam up to 150 GeV. The Tevatron, located under the main ring, uses a superconducting magnet system for the main guide field. The Tevatron uses the Main ring operating at 150 GeV peak energy as an injector. The Main ring is also operated at 120 GeV excitation in order to accelerate protons and to extract them to the antiproton production target. The resultant antiprotons, with an energy

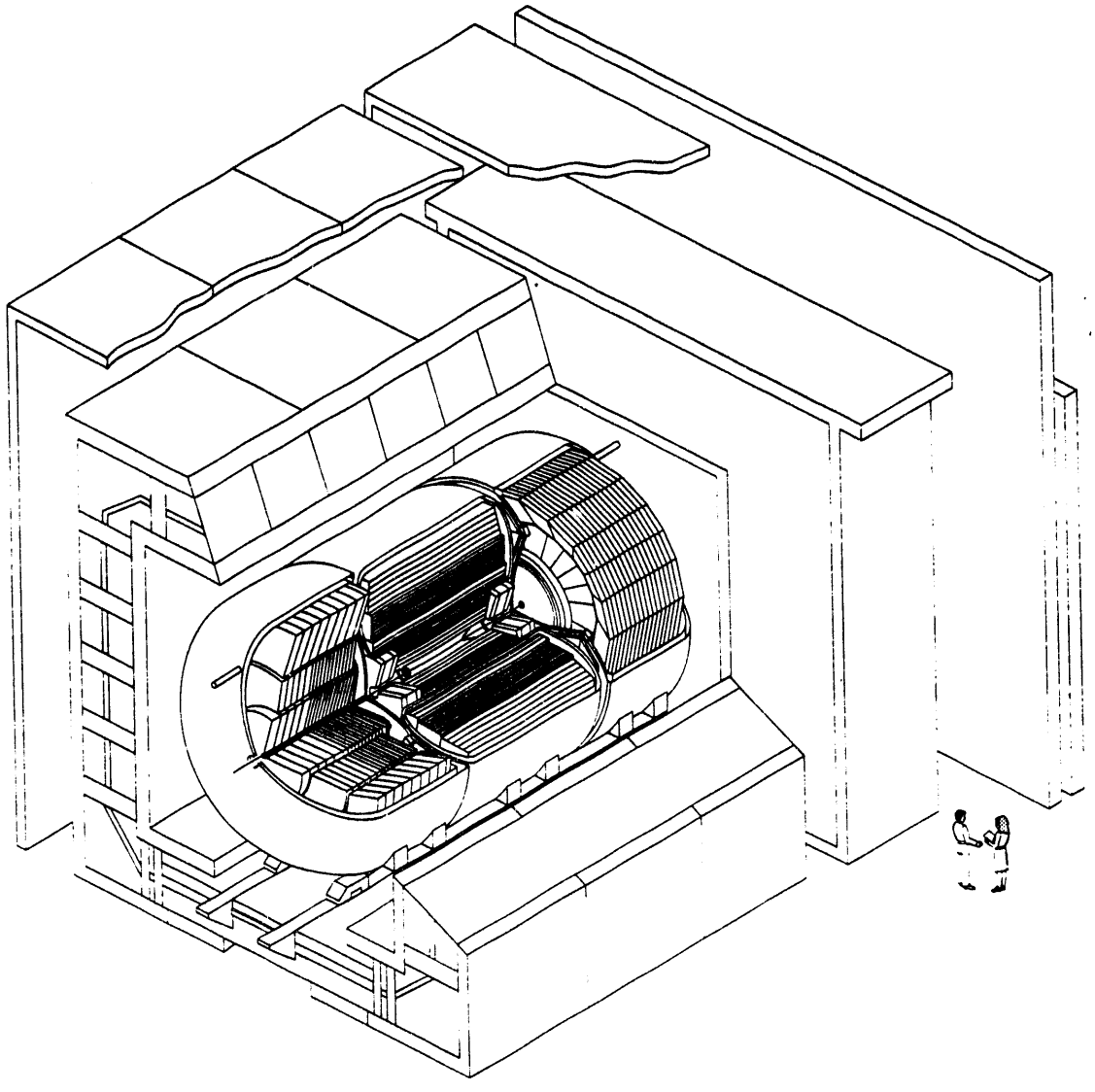

Figure 7. The DØ detector.

of 8 GeV, are collected in a debuncher source ring. They are then transferred to the accumulator source ring where the antiprotons build up for many hours. During the accumulation time, the phase space of the antiprotons is reduced by stochastic cooling. After an adequate number of antiprotons have been collected and cooled,

they are injected back into the main ring where they are accelerated to 150 GeV. Six equally spaced bunches of protons and antiprotons are injected into the Tevatron which accelerates each of the bunches to its maximum energy of 900 GeV each. Collisions occur at DØ and BØ interaction regions at a centre of mass energy of 1.8 TeV every 3.6μs.

2.2 The DØ Muon System

The DØ muon system [22] consists of magnetized toroids and three layers of proportional drift tubes (PDT). The PDT's are divided into wide angle (WAMUS) and small angle muon spectrometers(SAMUS), together having an angular coverage down to three degrees with respect to the beam pipe. The total number of interaction lengths seen by the particle as a function of the angle is shown in Figure 8. The shaded region represents the contribution from the calorimeter. The total number of interaction lengths between the calorimeter and the toroids vary between 9.5 and 18.7 at various angles. Brief descriptions of the toroids and the PDT's are given below.

2.2.1 The Muon Toroids

The muon system consists of five toroids, one central toroid (CF), two endcap toroids (EF) and two smaller toroids for the small angle muon spectrometer. All the toroids operate at 19 kG. The angular coverage of the toroids extend to 2.5 degrees with respect to the beam pipe. Table 5 gives some of the characteristics of the muon toroids.

Table 5.–Toroid characteristics.

Toroids	Central (CF)	Endcap (EF)	Small angle
Z interval(cm)	± 378.5	447.0 - 599.4	447.0 - 599.4
Angular coverage	$41 \leq \Theta \leq 139$	$9 \leq \Theta \leq 43$	$2.5 \leq \Theta \leq 11$
Mean field (Tesla)	1.9	1.9	1.9
Number of coils	20	8	4
Turns/coil	10	8	24
Current (Amps)	2500	2500	417
Voltage (Volts)	107	19	13.3
Resistance ($m\Omega$)	42.8	7.5	32

2.2.2 The Wide Angle Muon Spectrometer

The WAMUS consists of three layers, the layer A positioned before the toroid and the outer two layers B and C located outside the toroid. Each layer is made up of smaller modules positioned adjacent to each other to form a muon wall. The modules are further broken down into unit cells. The unit cell consists of 61 cm long diamond shaped cathode pads lining the top and bottom of its interior surface. The top and the bottom pads are shifted in wavelength by $\lambda/2$. In addition a sense wire is stretched across two adjacent cells and is read out from both ends.

The x-coordinate of a particle is measured using the drift time information from one end of the sense wire with a time to voltage converter (TVC). The resolution obtained in measuring the x-coordinate is 0.3 mm.

There are two steps in obtaining the z coordinate measurement. The first step involves measuring the difference in arrival time of the analog signals between the

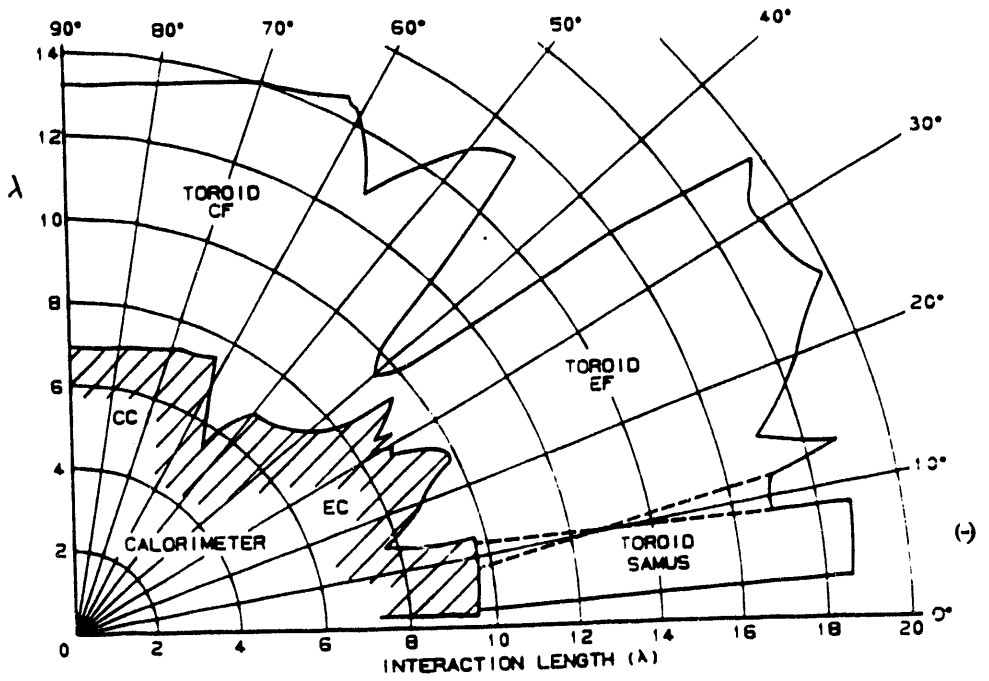

Figure 8. Interaction lengths as a function of theta.

two ends of the sense wire by using a delta-TVC. This coarse first step yields an approximate z-coordinate to within $\pm$10 cm. and locates the position of the particle to within one diamond pattern on the cathode pads. The second step involves the usage of the cathode pads. The induced signals on the pair of cathode pads inside the unit cell is digitized by an analog to digital converter (ADC). The precise position of the particle within a diamond pattern is given by (A - B)/(A + B), where A and B are the amplitude of the signal induced in each of the pads. From the information using the above steps, the z-coordinate of a particle traversing the muon chamber is measured to an accuracy of 2 mm.

Using the information from all the three layers of the muon chamber, the position

Table 6.–Muon chamber characteristics.

Number of layers	3
Number of planes	18
Number of modules	164
Number of cells	11386
Number of cathode pads	22772
Interaction lengths	9.5 - 18.7
Angular coverage	$9 \leq \Theta \leq 139$
Gas mixture	$Ar+CO_2+CF_4$ (90:5:5)
Maximum drift time	200 nsec
Drift velocity	47 $mm/\mu sec$
Transverse resolution	± 0.2 mm
Longitudinal resolution	± 2 mm
Bend angle resolution	± 0.2 mrad
$\delta p/p$	18%

and the angle of the muon is measured to an accuracy of ± 0.17 mm and ± 0.2 mrad, respectively. The characteristics of the wide angle muon chamber is summarized in Table 6.

2.2.3 The Small Angle Muon Spectrometer

The SAMUS consists of 3 planes, covering an angular range of $3 \leq \Theta \leq 11$ degrees. The three planes have the unit cells oriented at 45 degrees with respect to each other. There are 256 cells in the two outer planes oriented parallel and perpendicular to each other in the transverse plane and 360 cells in the middle plane oriented at 45 degrees with respect to the outer two. The gas mixture used is

CF_4 and CH_4 (90:10%). A coordinate resolution of 0.2 mm has been measured.

2.3 The DØ Calorimeter

The DØ calorimeter [23] as shown in Figure 9 is divided into two distinct sections, the central calorimeter (CC) and the forward/backward endcap calorimeter (EC). The electromagnetic and fine hadronic compartments in both CC and EC use depleted uranium as the absorber and the coarse hadronic compartments use copper or stainless steel. The active medium used is liquid argon. The calorimeter provides good energy resolution and segmentation with hermetic coverage. These properties allow accurate jet determination and electron identification with good missing P_T resolution. Further improvements in missing E_T resolution is provided by massless readout gaps and an inter-cryostat detector (ICD) between the central and endcap cryostats.

2.3.1 The Central Calorimeter

The central calorimeter is composed of three cylindrical layers, the electromagnetic (EM), the fine hadronic (FH) and the coarse hadronic (CH) layer. The characteristics of each of these layers is given in Table 7. Each of the layers consist of wedge shaped modules with 2π azimuthal coverage in Φ. The EM layer contains 20.5 radiation lengths of material in the range $35° \leq \Theta \leq 145°$. The hadronic layers, FH and CH, contain 6.93 absorption length of material in the range $60° \leq \Theta \leq 120°$. Each module consists of a repetitive cell structure. The basic cell structure, consists of an absorber plate, an argon gap, a readout board followed by a second argon

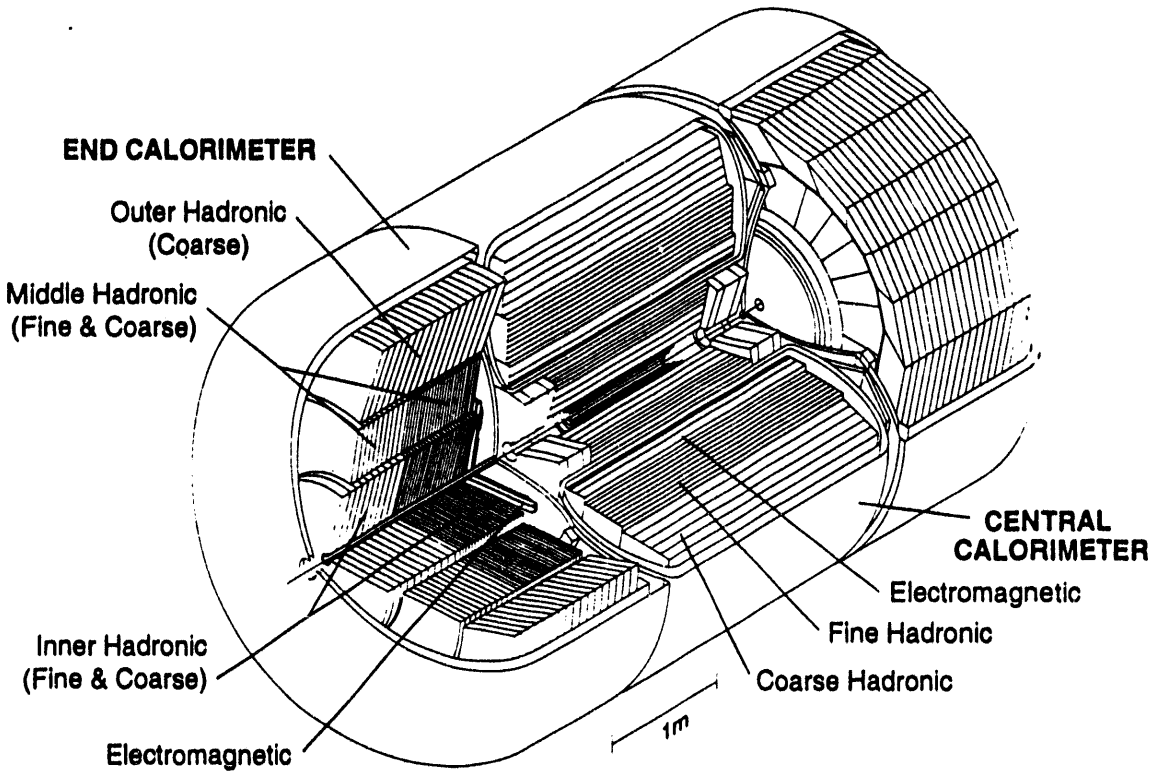

Figure 9. A cut away view of the DØ Liquid Argon Uranium Calorimeter.

gap. The readout board is constructed from two 0.02 in. G10 boards which are laminated with copper pads on the interior surface. The external surface is coated with graphite loaded resistive epoxy. An application of positive high voltage on the resistive coat, with the uranium plates at ground, causes an electric field in the argon gaps. The field causes the ionized charge left by the charged particle in the argon to flow which in turn induces a charge in the copper pads through capacitative coupling.

The readout boards are ganged together in a projective tower geometry. The CC is divided into eight depths in the radial direction, each depth consisting of repetitive

Table 7.-Central Calorimeter characteristics.

Calorimeter	Electromagnetic	Fine Hadronic	Coarse Hadronic
Number of modules	32	16	16
Absorber[a]	Uranium	Uranium	Copper
Absorber Thickness (in)	0.118	0.236	1.625
Argon gap (in)	0.09	0.09	0.09
Number of cells/module	21	50	9
Radiation length	20.5 X_0	3.24 λ_0	2.93 λ_0
Number of depths	4	3	1
Cells per readout depth	2,2,7,10	20,16,14	9
Radiation length/cell	0.975	1.92	3.29
Absorption length/cell	0.036	0.0645	0.317
Total radiation lengths	20.5	96.0	32.9
Total absorption lengths	0.76	3.23	3.17
Sampling fraction (%)[b]	11.79	6.79	1.45
$\Delta\phi$ segmentation[c]	0.1	0.1	0.1
$\Delta\eta$ segmentation[c]	0.1	0.1	0.1
Number of towers	10368	3000	1224
Rapidity coverage	$\pm$1.2	$\pm$1.0	$\pm$0.6

[a]Uranium absorbers are depleted. FH absorbers also contain 1.7% Niobium.

[b]Average sampling fraction over all depths indicated.

[c]The third layer of EM section has finer segmentation of 0.05 $\times$ 0.05.

cells ganged together. Both the electromagnetic and the hadronic sections have a transverse segmentation of $\Delta\phi \times \Delta\eta = 0.1 \times 0.1$, except for the third depth of the EM layer. This has a finer segmentation of $\Delta\phi \times \Delta\eta = 0.05 \times 0.05$ which allows a

more accurate measurement of the electromagnetic shower location where its peak is expected to occur.

The energy resolution of the calorimeter can be written as the sum in quadrature of three independent terms

$$\left(\frac{\sigma}{E}\right)^2 = C^2 + \frac{S^2}{E} + \frac{N^2}{E^2}$$

C is a constant term proportional to the energy and includes contributions from errors in gain determination of a channel, inductive or capacitative coupling between channels and variations in uranium plate and argon gap thickness. The sampling term, S, is proportional to the square root of the energy term. It includes contributions from intrinsic shower fluctuations and fluctuations between visible energy in the argon and hidden energy not sampled in the active medium. The noise term, N, is independent of the energy. It includes contributions from electronic noise, uranium radioactivity noise, pedestal drifts and other such energy independent sources.

The calorimeter modules have been calibrated using a test beam with electrons and pions. The results [24] from test beam calibration are

For electrons :

$$C = 0.003,\ S = 0.162,\ N = 0.140$$

For pions :

$$C = 0.047,\ S = 0.439,\ N = 1.28$$

The response of the calorimeter to electrons and pions has been measured using the test beam. The ratio e/π has been measured to be 1.020 ± 0.003 where the

systematic uncertainties come from the variation in the preamplifier response and uncertainty in the knowledge of the correct sampling fraction. Thus the calorimeter is compensating giving nearly equal response to both electrons and pions and thereby improving the hadronic energy resolution.

2.3.2 The Endcap Calorimeter

The endcap calorimeter consists of four distinct sets of modules, the electromagnetic (EM), inner hadronic (IH), middle hadronic (MH) and the outer hadronic (OH). The endcap calorimeter possesses a projective tower geometry like the central calorimeter. The transverse segmentation is $\Delta\eta \times \Delta\phi = 0.1 \times 0.1$ for a rapidity $|\eta| \leq 3.2$. Above $\eta = 3.2$, the pad sizes are larger corresponding to a coarser segmentation which varies with various endcap modules.

The EM and the IH use depleted uranium as the absorber. The EM calorimeter consists of 21 radiation lengths of material spanning the angular region $3° \leq \Theta \leq 27°$ with respect to the beam axis. It is divided longitudinally into four readout depths, each readout depth consisting of cells ganged together. The cell structure in the endcap calorimeter is similar to the central calorimeter. The inner hadronic consists of one module for each endcap and is located behind the EM as shown in Figure 9. It is divided into fine and coarse sections, each containing 64 and 12 cells respectively, totalling 9.3 interaction lengths of material. The fine section is divided longitudinally into four readout depths.

The middle hadronic section consists of 16 trapezoidal modules, which form an annular ring around the IH. It covers an azimuthal angle of 22.5° each. Each module

Table 8.–Endcap Calorimeter characteristics.

Calorimeter	EM	IFH	ICH	MFH	MCH	OH
Number of modules	1	1	1	16	16	16
Absorber[a]	U	U	U	U	SS	SS
Absorber Thickness (in)	0.118	0.236	0.236	0.236	1.83	1.83
Argon gap (in)	0.09	0.082	0.082	0.087	0.087	0.087
Number of cells/module	18	64	12	60	14	24
Number of depths	4	4	1	4	1	3
Cells per readout depth	2,2,6,8	4×16	12	4 × 15	12	3 × 8
Total radiation lengths	20.131	121.837	32.778	115.519	37.945	65.072
Total absorption lengths	0.949	4.912	3.573	4.045	4.084	7.006
Sampling fraction (%)[b]	11.90	5.66	1.53	6.68	1.64	1.64
$\Delta\phi$ segmentation[c]	0.1[d]	0.1	0.1	0.1	0.1	0.1
$\Delta\eta$ segmentation[c]	0.1[d]	0.1	0.1	0.1	0.1	0.1
Number of towers	7488	4288	928	1472	384+(64)[e]	896+(64)[e]
Rapidity coverage	1.3-3.7	1.6-4.45	2.0-4.45	1.0-1.7	1.3-1.9	0.7-1.4

[a]Uranium (U) absorbers are depleted. IH and MFH absorbers contain 1.7% Niobium, SS = Stainless Steel.

[b]Average sampling fraction over all depths indicated.

[c]$\Delta\phi$=0.2 and $\Delta\eta \geq 0.2$ (varies) for $\eta > 3.2$.

[d]The third layer of EM section has finer segmentation of 0.05 × 0.05 for $\eta < 2.6$.

[e]MCH and OH modules are summed together at η=1.4.

is divided into a fine (MFH) and a coarse (MCH) section. The fine section is made up of 60 cells using niobium doped uranium as the absorber, and the coarse section is made of 14 cells using stainless steel as the absorber.

The transverse segmentation of the endcap modules is $\Delta\eta \times \Delta\phi = 0.1 \times 0.1$ for $\eta < 3.2$. At small angles the pad sizes are bigger and the segmentation varies up to as large as $\Delta\eta \times \Delta\phi = 0.4 \times 0.4$. The segmentation of the third depth of the electromagnetic module, where the peak of the shower occurs, is finer with $\Delta\eta \times \Delta\phi = 0.05 \times 0.05$.

2.3.3 Massless Gaps and the ICD

A particle traversing through a region in the calorimeter, especially towards EC-MH and EC-OH modules, passes through several layers of central and endcap calorimeter support structures which contribute to the dead regions. This can cause large fluctuations between visible and undetected energy which will directly effect the missing E_T resolution. To minimize these effects, massless gaps and ICD's are introduced on the outer surface of the central calorimeter and the inner surface of the endcap calorimeter. The massless gaps are a set of readout boards ganged together with only the active media, liquid argon between them. A significant visible energy deposition would indicate possible large amounts of energy deposited in the dead region of the calorimeter and thus provides a good tag against these poorly measured candidates.

2.4 The DØ Central Tracking System

The central tracking system [25] consists of four distinct subdetectors as shown in Figure 10. The vertex chamber consists of three layers of cylindrical drift cells and occupies the region closest to the interaction point. Following the vertex chamber

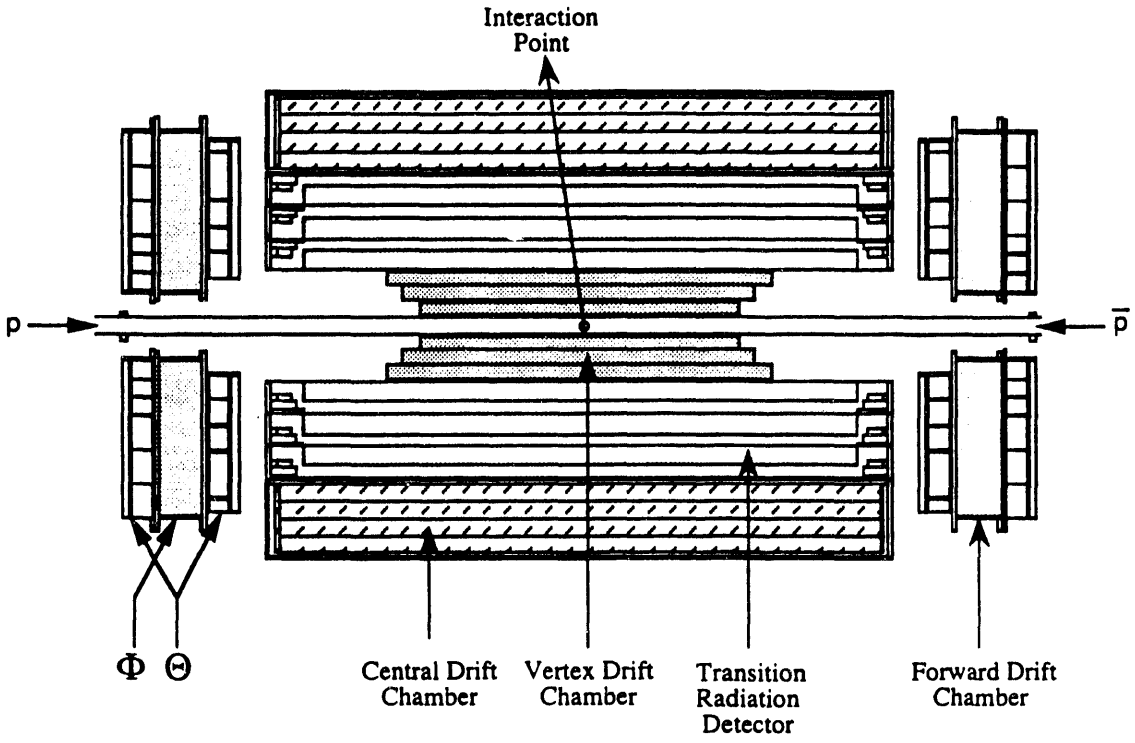

Figure 10. The DØ central tracking system.

are three concentric layers which make up the transition radiation detector. The outer central drift chamber consists of four layers of cylindrical drift cells and lies in the region outside the transition radiation detector. The endcap region is equipped with forward/backward drift chambers. Each of these detectors is explained below in detail.

The three tracking chambers provide good spatial resolution and two track separation. dE/dx is used to distinguish between singly and doubly ionizing particles. These features allow matching of tracks from impact points given by the calorimeter and the muon chambers and the reconstructed tracks from the central tracking system. It also allows detection of gamma conversions which give rise to non prompt

electrons, detection of kinks from decays in flight of pions and kaons and identification of multiple vertices. In addition, the transition radiation detector provides complimentary electron identification to the calorimeter.

2.4.1 The Vertex chamber

The vertex chamber provides precise track information close to the interaction region and uses the inner layer to identify secondary vertices. It also identifies charged tracks and vetos photons that convert entering the transition radiation detector. The walls of the vertex chamber are made up of a low radiation thickness material, carbon fibre cylinder, to minimize production of e^+e^- from photon conversions.

The vertex chamber [26] consists of three mechanically independent layers of drift cells possessing a jet chamber geometry. The outer two layers of the chamber are broken into 32 sectors, while the inner layer is made up of 16 sectors. The wires in each layer of the drift tubes are supported by G-10 bulkheads mounted on the carbon fibre cylinder on either side. Each sector consists of eight sense wires which are read out on both ends to measure charge division. The sense wires, made of NiCoTin, are staggered by ± 100 μm to resolve left right ambiguity. Each of the sectors also contain 18 grid wires which shape the electric field near the sense wire plane. There are 16 cathode wires in each sector which provide a uniform drift field outside the grid zone and 16 fine field wires which maintain field uniformity away from the centre of the cell. Longitudinal information obtained by charge division is measured by comparing the integrated pulse height from each end of the sense

Table 9.–Characteristics of vertex and central drift chamber.

Drift Chamber	VTX	CDC
Maximum length (cm)	116.8	135.0
Number of layers	3	4
Phi sectors/layer	16,32,32	32
Sense wires/sector	8	7
Total number of sense wires	640	903
Number of alternate readout channels	832[a]	256
Sense wire stagger (μm)	100	200
Maximum drift distance (mm)	13.7	70.8
Gas mixture	CO_2/C_2H_4	$Ar/CH_4/CO_2$
Pressure of gas (atm)	1	1
Drift velocity ($\mu m/nsec$)	8	34
Sense wire resolution (μm)	60	200
Charge division resolution (cm)	± 1	-
Alternate readout resolution (mm)	± 4[a]	20
Pair resolution (mm)	7	10

[a]The readout of the cathode pads providing the alternate coordinate measurement for the vertex chamber has been disabled due to oscillation problems [27].

wires. The chamber uses a 95:5% gas mixture of CO_2 and C_2H_4 and is operated at atmospheric pressure. Table 9 summarizes the characteristics of the chamber.

2.4.2 The Transition Radiation detector

Transition radiation is produced when a charged particle passes through two media of different dielectric constants. In a highly relativistic environment, most of the transition radiation is emitted at X-ray frequencies. The intensity of the X-rays produced is proportional to $\gamma = E/m$, where m is the mass of the charged particle. The X-rays are produced in a small cone Θ which is inversely proportional to γ. These features allow discrimination of electrons from pions under relativistic conditions. The intensity emitted by a single interface between two media is small. Therefore, a radiator consists of a large number of thin foils separated by a medium of different dielectric constant. The total intensity of the emitted X-rays due to the large number of foils is the sum of the intensities emitted at each interface and the interference effects ignoring losses due to absorption in material. The interference effects largely depends on the choice and thickness of the radiator foil and the spacing between them.

The transition radiation detector [28] consists of three cylindrical layers and lies outside the vertex detector. Each layer consists of a radiator and an X-ray detector. The radiator is made of many layers of 18 μm thick polypropylene (C_2H_2) foils with 150 μm gap spacing. The gaps are produced by an indentation technique. This involves placing the C_2H_2 foil over a polyethylene net and heating the foil while pumping on it [29]. This causes the foil to take the shape of the polyethylene net and when rolled forces each layer to be separated by 150 μm. The radiator in each layer of the TRD consists of 382 layers of foils flushed with dry nitrogen which acts as the second dielectric medium. The radiator is followed by a longitudinal drift

chamber. The radiator and the chamber are separated by a 3 mm gap which is filled with CO_2 to prevent contamination of Xenon in the adjacent layer. The drift chamber consists of a 16 mm drift zone followed by an amplification zone, consisting of 20 μm anode wires and 50 μm field wires. The X-ray detector in each layer of the TRD consists of 256 anode wires separated by 8 mm. It uses Xe/C_2H_6 gas mixture which has a low electron attachment relative to other gases and has a reasonable probability of detecting the few keV photons typical of transition radiation.

The detector has been tested at CERN [30] using an electron and a pion beam. A probability distribution of both pions and electrons has been measured separately. Based on the probability distributions, the maximum likelihood of one or more parameters such as the total energy deposited, the number of clusters and the cluster - drift time correlation is calculated. A cut using the Neyman Pearson technique [31] is applied to identify electrons. This method gives a pion rejection factor of 50 at 90% electron efficiency.

2.4.3 The Central Drift chamber

The Central drift chamber [32] covers a rapidity of -1 to +1 in eta and surrounds the TRD as shown in Figure 10. It provides radial and longitudinal spatial information for tracks before their entry into the central calorimeter.

The Central drift chamber (CDC), is a cylindrical shell consisting of four distinct radial layers. Each layer is divided azimuthally into 32 cells. Cells from adjacent layers are staggered by a half-cell. Each cell consists of seven sense wires and two delay lines. The sense wires in each cell are staggered by $\pm 200 \mu m$ to resolve the left

right ambiguity. The delay lines are located on the inner and outer shelves of each cell adjacent to the first and the seventh sense wire. Charge induced on the delay line by the nearest sense wire propagates in both directions. The arrival time of the pulse in each direction is then used to provide the longitudinal position of the track. Each cell is made with Rohacell coated with epoxy and Kevlar. Field shaping is provided by resistive strips printed on Kapton which cover the Rohacell.

The CDC is operated with DØ gas (93% Ar, 4% CH_4, 3% CO_2) at atmospheric pressure. The chamber has been extensively studied [33] using test beam and cosmic rays. Spatial resolution of $180\mu m$ and z-resolution using delay lines of $\pm 2mm$ have been measured. Table 9 highlights the characteristics of the chamber.

2.5 The DØ Forward Tracking System

The forward drift chambers provide coverage for low angle tracks prior to their entrance into the end calorimeters. The coverage extends from 30 degrees down to 5 degrees with respect to the beam axis in both forward and backward directions. Each forward drift chamber is located symmetrically about the interaction point as shown in Figure 10.

Each forward drift chamber consists of three layers as shown in Figure 11. The outer two layers are the Theta chambers which measures the theta of the track. The inner layer is the Phi chamber and measures the phi of the track. This section explains the construction and operation of these chambers.

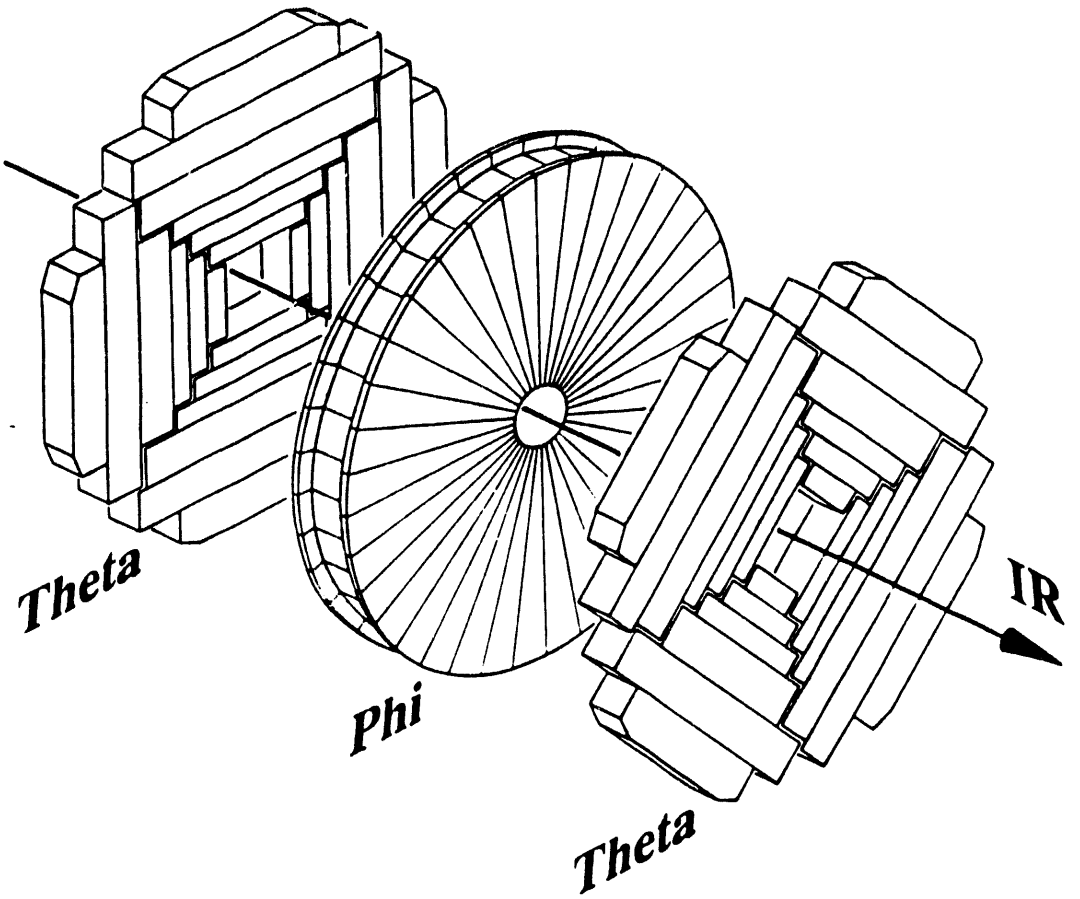

Figure 11. The Theta and Phi forward drift chamber.

2.5.1 The Θ chambers

Each layer of the Theta chamber consists of four quadrants. Each of the four quadrants is made of six rectangular cells located at increasing radii. The three cells located at the outer radii limits are 10.6 cm wide. The inner three cells are half the width of the outer three cells. Each of these cells have eight sense wires and a delay line. The sense wires in the two outer half cells are strung at their inner radius limits, the middle at its outer radius limit and therefore the electron drift is

unidirectional. The full cells have the sense wires strung at the centre of the cell and are staggered to resolve left right ambiguity. The sense wires measure the position of a charged track along the plane perpendicular to itself. The inductive delay line consists of a carbon fibre epoxy core wound with copper. It is located underneath the first sense wire in each cell and are read out from either ends. An opposite polarity charge is induced on the delay line by the nearest sense wire. Measurement of the signal on each end provides the position of the track along the direction of the sense wire. Using both the sense wire and the delay line information, the theta angle of the track is calculated. The sense wires are separated by 8 mm spacing. There are two guard wires between each pair of sense wires which are kept at ground. These provide fine field shaping near the sense wires.

The top and bottom panels of each theta quadrant is made of Rohacell coated with Kevlar. They are covered with Kapton on which copper traces are etched to provide field shaping. The side walls of the theta quadrant are made of 0.008 in. aluminium foil on Nomex honeycomb. The end plates of the theta chamber which support the sense and the guard wires are made of G10. They are precision drilled and etched with copper traces to carry the signal lines to a preamplifier board mounted on the chamber. The sense and the guard wires are soldered and glued to one end plate. A weight is hung on the other side to apply tension to the wires and then soldered. The tension is checked by oscillating the wire in a fixed magnetic field to find the characteristic frequency of the wire. The tension was chosen such that the sagitta of the wire generated by the electrostatic forces and gravity is less than 25 microns. The theta cell walls are initially prestressed to prevent slack in

Table 10.–FDC Wire Tensions.

Chamber	Prestress	Wire Tension			
		SW0	SW2-SW6	SW7	Guard wire
	(kg)	(gr)	(gr)	(gr)	(gr)
Theta -					
A0,A1,A2	3.6	50	50	50	150
A3,A4	5.5	100	50	100	150
A5	5.5	100	50	50	150
Phi -					
Chamber 1[a]	10.0		100		150
Chamber 2[a]	10.0		100		200

[a]All 16 Phi chamber sense wires are strung with the same tension.

the wires after they are strung. The sense wires are made of gold plated tungsten. The guard wires are gold plated aluminium.

2.5.2 The Φ chambers

The phi chamber is sandwiched between two layers of theta chambers as shown in Figure 10. Each phi chamber consists of 36 azimuthal cells with 16 sense wires strung radially along the longitudinal coordinate of a traversing particle. The sense wires are separated by 8 mm and staggered by $\pm$ 200 μm to resolve the left right ambiguity. A single guard wire in between the sense wires provides the fine field shaping.

The top and bottom panels of the phi chamber are made of Nomex honeycomb coated with Kevlar. Like the theta chamber, they are covered with Kapton etched

with copper traces to provide field shaping. The cell walls are etched 0.001 in. aluminium strips on 0.005 in. G10 to form field shaping electrodes. The outer and inner hubs of the phi chamber are made of aluminium. They are precision drilled to support the sense and the guard wires. After prestressing, the wires are strung with the appropriate tension and crimped.

2.5.3 Operating environment

Both the theta and phi chamber are operated with DØ gas. This gas consists of 4% CH_4, 3% CO_2 and the rest Argon. A mixture of CO_2 and CH_4 acts as a good quenching agent. The fraction of each of the agents is kept low enough so as to avoid polymerization and eventual breakdown in the chamber while running in a high radiation environment [34]. The gas mixture provides a gain of $O(10^4)$ and a constant drift velocity over a wide range of operating voltage. The chamber is operated at atmospheric pressure.

The maximum drift distance in both the theta and phi chamber is 5.3 cm. The field shaping electrodes provide constant drift field across this region. The theta chamber is operated at 950 V/cm and the phi chamber is operated at 750 V/cm. The guard wires in both the theta and the phi chamber are kept at ground voltage. Various studies have been performed to find the optimum operating sense wire voltage which will be discussed in the next chapter. The sense wires in phi and theta chambers are operated at +1.5 and 1.55 kV respectively. The sense wire closest to the delay line is operated at a higher voltage than the other sense wires to obtain a better resolution in the delay line. This is operated at 100 V above the

Table 11.–Specifications of the forward drift chamber.

	Theta Chamber	Phi chamber
Radial interval	11-62 cm	11 - 61.3 cm
Sense wires per cell	8	16
Sense wire staggering	$\pm$ 200 μm	$\pm$ 200 μm
Delay lines per cell	1	0
Sense wire separation	8 mm	8 mm
Sense wire diameter	30 μm	30 μm
Guard wire diameter	163 μm	163 μm
Drift field	950 V/cm	750 V/cm
Sense wire potential	1.55[a] kV	1.5 kV
Gas, pressure	$Ar/CH_4/CO_2$(atm)	$Ar/CH_4/CO_2$(atm)
Readout channels per end	480	576

[a]The sense wire adjacent to the delay line is operated at 1.65 kV.

other sense wires. Table 11 summarizes the characteristics of the forward tracking system.

2.6 Electronics

This section explains the three stages of the electronics chain which carry the analog signal from the central tracking chambers. The chambers have more than eight thousand wires which are processed in parallel. Each wire is connected to a preamplifier, followed by shaping circuitry which provide pulse shaping and second stage amplification. The analog signals are then digitized by a 106 MHz waveform digitizer [35] and zero suppressed. Digitized waveforms are sent to the second level

trigger where they are filtered and sent to the host computers.

The tracking chambers use a quad common base MB43458 charge preamplifier sold by Fujitsu [36] . A hybrid chip is constructed with 8 channels mounted on a ceramic substrate and then plugged into a printed circuit board installed on the chamber. Each channel consists of a common base input stage followed by a two stage emitter follower. Extensive studies [37] [38] on linearity, gain, cross talk and signal to noise ratio have been made. The hybrid also contains two test pulse inputs, each connected to odd and even channels respectively.

The single ended output of the preamplifier is connected to the shaping circuitry [39] through a flat ribbon of 18 coaxial cables. Each channel in the shaping circuitry consists of two parts, a shaper hybrid amplifier and a header with invidualized shaping components. The amplification and shaping is done in 3 stages. The first and the last stage use differential video amplifiers mounted on the hybrid, each with one pole zero filter located on the header. The components of the pole zero filters are tuned to provide optimal rise and fall times of the pulses. Typical rise and fall times for pulses are 15 nsec and 35 nsec respectively. An intermediate stage consists of a single ended amplifier with an RC network which provides cable compensation. Each shaper module consists of 32 such channels and is mounted in a VME based crate. The crate also contains a programmable test pulse module which is used to generate and direct test pulses for calibration purposes.

The shaped analog signals are carried over coaxial cables and fed as input to a 106.208 MHz FADC system [40]. The first stage of the FADC consists of a bilinear buffer amplifier which provides a dual gain to extend the 8 bit range of the FADC.

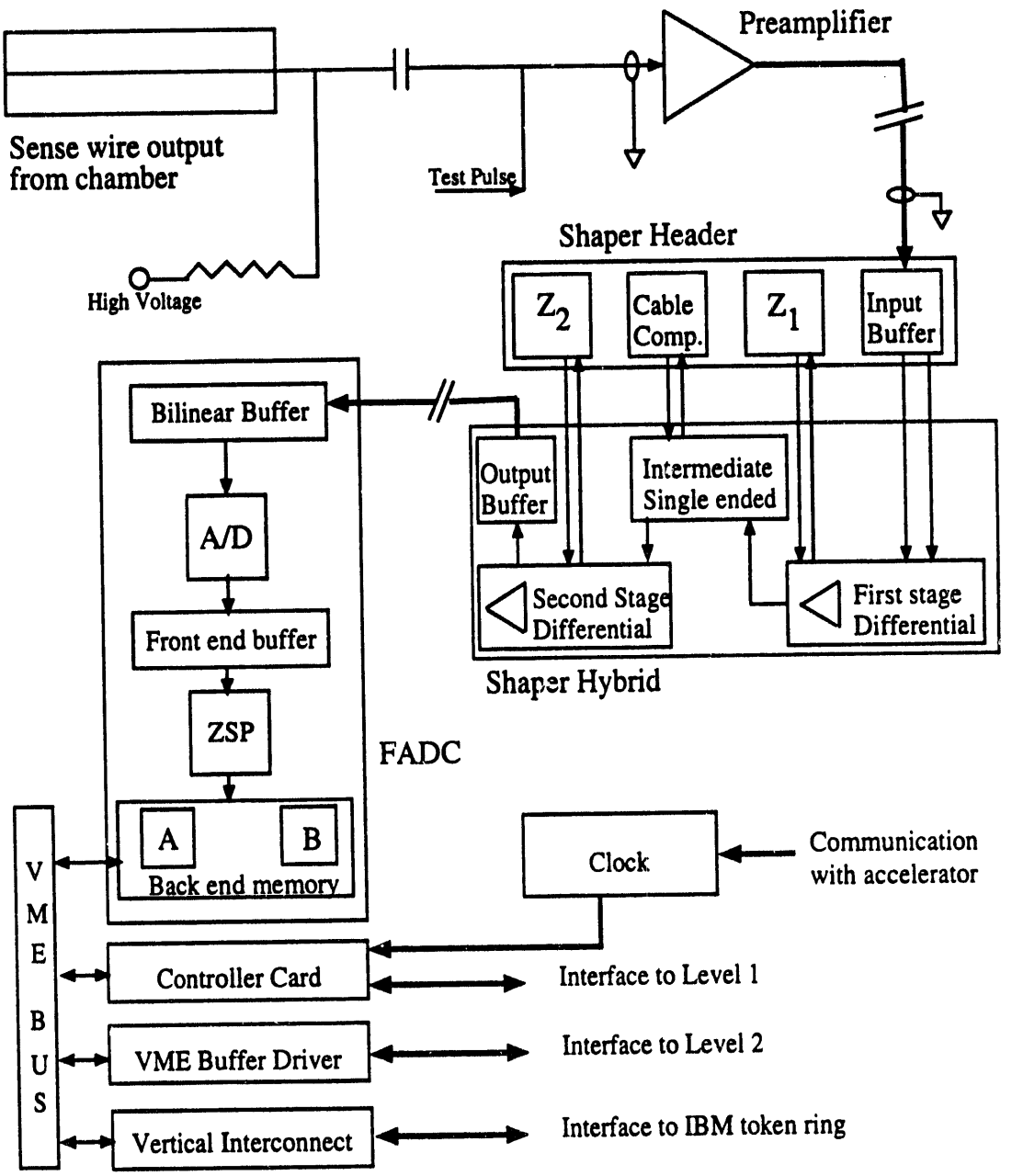

Figure 12. DØ central tracking electronics readout path and controls.

Analog signals above a break point voltage level are subjected to a lower gain than those below the break point voltage level. The buffer hybrid has programmable gain control which can be varied up to a factor of two. The second stage consists of an 8 bit Sony CX20116 flash analog to digital converter. Together with the bilinear amplifier, it effectively provides a $9\frac{1}{2}$ bit range. The digitized outputs are then stored in the front end buffer and passed through a semi-custom zero suppression chip (ZSP) operating [41] at 26.552 MHz. The chip is programmed to recognize leading and trailing edges of a pulse and to suppress the pedestal data between the pulses. A leading or a trailing edge is recognized by comparing the pulse height of each digitized bin with preset thresholds. It also uses a combination of thresholds and slopes which is the difference between pulse heights of two adjacent digitization bins. The data recorded as clusters is stored in the back end memory. Each cluster is tagged with a time stamp which indicates the time location of the first bin of the cluster during its digitization.

Each FADC crate may contain up to 16 FADC modules. Each FADC module consists of 16 identical channels described above. The FADC's are housed in a VME crate. The crate also contains a vertical interconnect which allows access to memory locations in the VME crate over a local network token ring system [42] . Each FADC channel is programmed with pedestal offsets, gain and zero suppression thresholds and slopes which result from electronic calibration.

The FADC crate also contains a controller card [43] which controls the digitization and readout of the crate. It provides an interface with the first and second level trigger systems. A clock system which runs synchronously with the accelerator

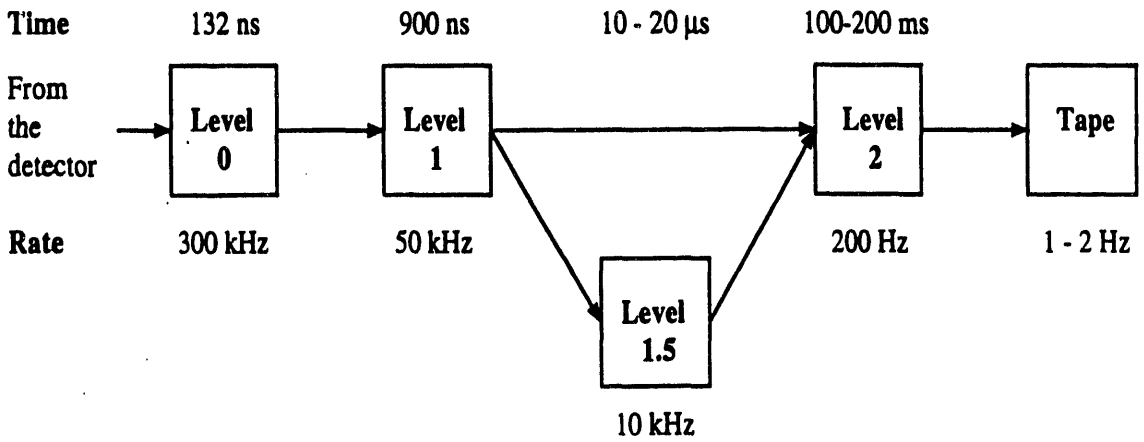

Figure 13. Data rates and processing time at each trigger level.

provides the 106.208 MHz signal for digitization. The digitization of the FADC start synchronously with each beam crossing. The resultant data stored in the front end buffer either go through the suppression cycle or are dumped depending on the response received from the first level hardware trigger. After the suppression cycle is complete, the data is stored in the back end memory. Each FADC crate houses a VME buffer driver which reads the data from the back end FADC memory and transfers them to the Level 2 microvax farm.

2.7 The DØ Trigger system

DØ has four distinct hierarchical trigger levels, Level Ø, Level 1, Level 1.5 and Level 2. The first three of these levels make a decision on the basis of hardware and the fourth utilizes software filter programs running on a farm of microvax based

computers. At a luminosity of $10^{30} cm^{-2} s^{-1}$ and with the accelerator operating with six bunches, the rate of beam interactions is expected to be 300 kHz. The four levels of the DØ trigger provides a mechanism for selecting interesting candidates and reducing the output trigger rate to 1-2 Hz. Figure 13 shows the rates and the average processing time by each of the four levels.

2.7.1 The Level Ø trigger

The Level Ø decision is made on the basis of counter hodoscopes located in the forward regions. Each end of the beam axis consists of two layers of plastic scintillating material perpendicular to each other. The counters are read out through photomultiplier tubes. The Level Ø is mounted on the inner surface of the end calorimeters and has an angular coverage of 10 degrees about the beam axis.

The Level Ø [44] relies on the presence of low angle jets produced in a $p\bar{p}$ interaction to reliably signal an interaction. The arrival time of the signals at the two ends of the detector is used to locate the interaction point to within ± 3 cm. Beam gas events can be identified by the presence of signals at only one end and can consequently be rejected. In addition, the Level Ø has the capability of identifying multiple interactions and monitoring the luminosity.

2.7.2 The Level 1 trigger

The Level 1 framework [45] [46] receives its inputs from the Level Ø, Calorimeter and Muon systems. In addition, it has the capability of receiving direct-in triggers which are essential for debugging the detector. A total of 256 trigger terms can be programmed to fire on either a set of conditions satisfied by the detector or on

a direct-in trigger. These trigger terms are latched on every beam crossing and used as inputs to an AND-OR network. A set of 32 specific trigger bits are further programmed to require the presence or absence of one or more trigger terms. Further digitization of all front end electronics associated with a specific trigger bit occurs if and only if that specific trigger bit has fired.

The DØ detector is split into 32 geographical sectors. Each of these sectors has one or more digitizing crates associated with it. A specific trigger is also programmed to send digitization signals to one or more of these geographical sectors. A microvax (the trigger control computer) which resides in the Level 1 framework, handles all such programming messages delivered to it from the host computer. Apart from coordinating the digitization of all crates, the framework builds its own data block which contains all the conditions under which the event was read out. The data block is passed to the Level 2 system, where they are filtered and sent to tape. The framework also manages a large number of scalers which provide essential online monitoring of the trigger system.

The analog signals from the calorimeter are digitized by an 8 bit FADC within the framework in order to arrive at a quick decision. The information from the calorimeter is used to calculate global quantities such as total electromagnetic and hadronic energies, transverse energies and missing transverse energy. Local cluster triggers are also formed by counting the number of individual electromagnetic and hadronic towers which exceed a given threshold. Each trigger term is programmed to look at these specific details of the calorimeter at various thresholds.

The muon trigger system further supplies inputs to the trigger AND-OR net-

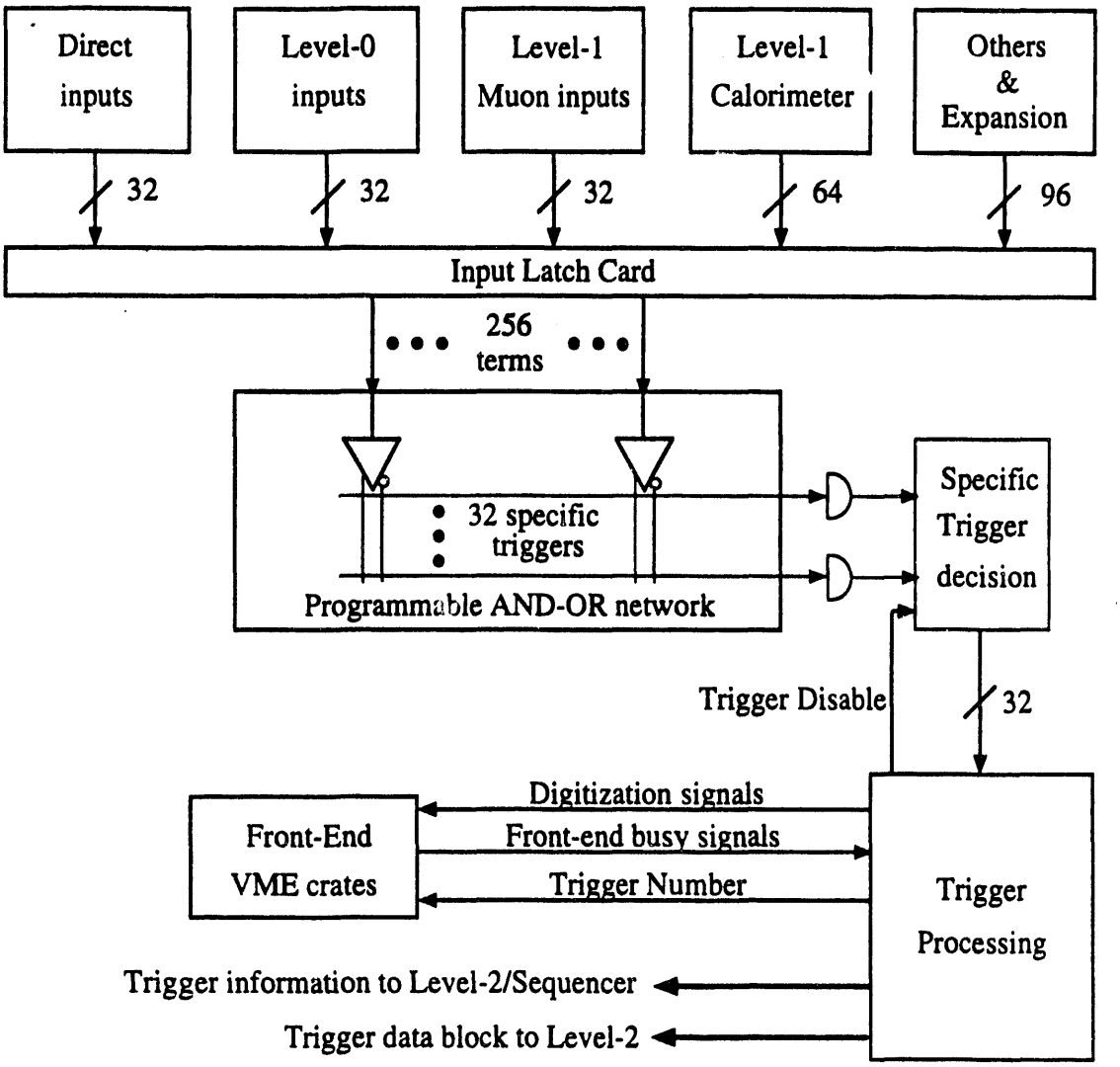

Figure 14. Level 1 trigger processing stages.

work. The muon trigger system is not a part of the general framework but supplies inputs which reflect the presence of one or more muons.

The above specified conditions are the first stage of the Level 1 trigger and initiate a digitization in the front end electronics. The Muon and the TRD systems

also provide a second stage (Level 1.5) trigger. The TRD calculates the integrated charge on each of its wires. This information is compared against a preset threshold and a list of electromagnetic shower candidates in the calorimeter. The muon system provides information on the transverse momentum. These are then compared to various thresholds which set the corresponding trigger term if the threshold condition is satisfied. Since this information arrives late, this cannot inhibit the front end electronics from digitizing and thus causes a minimal dead time. However it can veto the readout by the Level 2 system.

2.7.3 The Level 2 system

The Level 2 system [47] [48] is based on a farm of microVAX computers and uses its software capabilities to reduce the recorded event rate to 1-2 Hz. The DØ detector is divided into 8 readout sections, each readout occurring in parallel.

The digitizing crates are equipped with a VME buffer driver (VBD). The VBD is a VME based multiported memory whose function is to readout the data from the local ADC memory, store it in an onboard memory unit and then provide the current gain to drive a data cable. The data cable consists of two twisted pair cables, a 32 and a 13 pair, which carry the data and control signals respectively. There are 8 such data cables, one for each readout section. All VBD's within a readout section are connected with the data cable serially. Each data cable has an associated sequencer control card which interfaces with the Level 1 and the Level 2 system and controls the readout of the digitizing crates. After serially connecting all the VBD's with the data cable, the two ends of the data cable are connected to the sequencer to complete a circular loop.

The Level 2 framework consists of 50 identical systems. Each system consists of a VAXstation 4000 model computer [49] with 8 MB of on board memory. In addition, each system is equipped with 8 VMEMPM mulitport memories, one per readout section, which receives the data into the Level 2 nodes from the data cables. The use of multiport memories allows processors to access data over a private memory bus and thus eliminate the necessity of retransferring data to the local computer memory. The Level 2 farm is controlled by a supervisor processor. All microvax nodes use Digital's VAXELN as a real time operating system. Each system is capable of supporting floating point coprocessors to speed up the time used to analyze an event. This is envisioned as a possibility at a later date.

Upon receiving a request to be readout from the Level 1, the Supervisor processor assigns one or more Level 2 nodes to accept the data. It then passes the sequencer the necessary information required for it to read out the data. The sequencer is programmed with a look up table containing information on the digitizing crates to be read out for each specific trigger. The sequencer also receives the event number from the Level 1 which is used for synchronization. The sequencer uses this to build a readout token which is then circulated on the data cable. VBD's which are ready to transfer the data pick up the token. It compares the event number on the token with that in its pending buffer. If a match occurs, it transfers the data over the data cable at 40 MBytes per second and modifies the token appropriately to indicate its success. The token is circulated until all required crates have been read out. The data is shipped to the multiport memory on the assigned Level 2 node. The data is then available for further event processing by software filters running

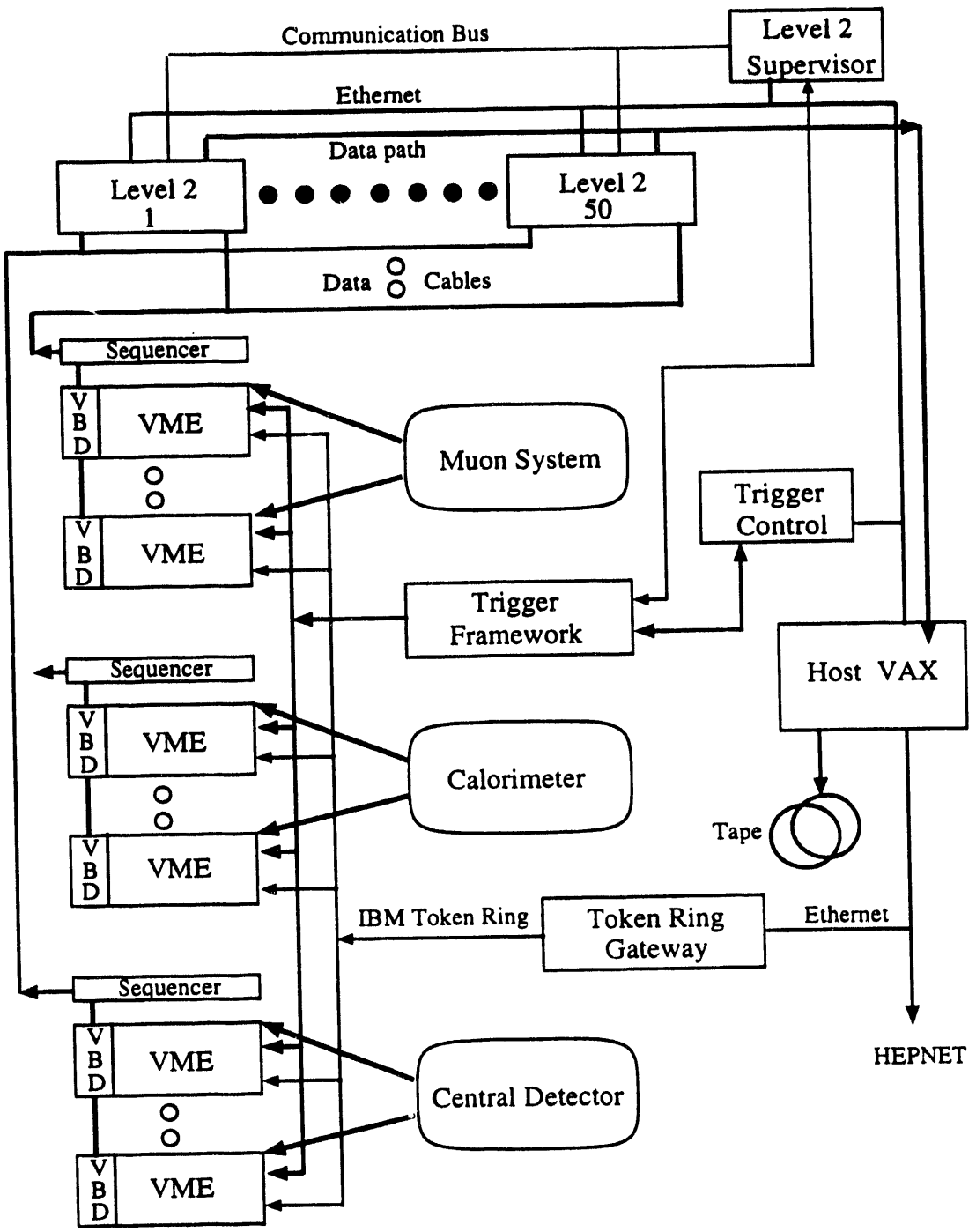

Figure 15. DØ data acquisition path and controls.

on the Level 2 node. If the event passes the filter, the data is then transferred to the host computers over a high speed link between the Level 2 framework and the host computer.

2.7.4 Coordination of systems

The coordination of various tasks and trigger systems is done from the host computer. A coordinating task runs as a detached process and interfaces with other online processes with specific tasks through ITC. ITC (inter task communication) is a custom software package which uses the VMS mailbox driver as a means of allowing two independent processes to communicate. The coordinating tasks also interfaces with the trigger systems. Various configuration files are set up through which the user makes a request to the coordinating task. The configuration file specifies the digitization crates to be read out, the trigger terms which should be considered and the software filters which must be acted on the trigger at the Level 2 stage. They also specify any initialization that needs to be performed on the requested crates before a begin run command is processed.

The coordinating task begins by requesting a download to the front end crates for initialization to a specific process which governs this task. It then programs the Level 1 and Level 2 systems with the necessary information. It instructs the data logging task, which gathers incoming data from the Level 2 system and directs it to disks and other online tasks. Once a begin run command has been issued, the coordinating task enables the requested specific triggers in the Level 1 and as explained in the previous section, the data acquisition cycle begins. When the requested trigger bit has been satisfied, the Level 1 initiates a start digitization to

the front end VME crates associated with the trigger bit. It builds its own event data block and sends out a request to the Level 2 system. The Level 2 system assigns a node, and reads out the data into its memory. Software filters running on the Level 2 node process the event and pass interesting candidates. If the event passes the necessary filter conditions, the event is sent to the host where it is gathered by the data logging task. These events are further examined on the host and written to tape.

Chapter 3
FDC Performance

The forward drift chamber has been extensively tested with electrons and pions in the Neutrino-West fixed target Area (NWA) at Fermilab from March 1990 through July 1990. Further tests with low energy beams were performed during the 1991 fixed target run. These tests included a study of the performance of the chamber which included efficiency measurements in a high multiplicity environment and the dE/dx response of the chamber. This chapter explains the performance of the chamber and the calibration and monitoring tools used for this study.

3.1 Electronic calibration

The digitized FADC output is typically 264 bytes of data for each channel equivalent to 2 MB of data per event for the entire DØ tracking system. The zero suppression chip reduces the large data block size by 80% by suppressing the pedestals and storing only clusters of data containing the pulse information. This not only enhances the rate with which data can be transferred to the host computers from the VME crate and thus minimize the dead time in the system, but also makes the data size manageable to deal with during offline processing. The zero suppression parameters [41] as explained in the previous chapter consists of four thresholds and three slope parameters per channel. These thresholds and slopes are used by the

zero suppression chip in the FADC hardware to determine the leading and the trailing edge of the pulse. The algorithm used by the zero suppression chip uses the following equations

$$\text{Leading Edge} = (C_1 \bullet C_5) + C_2$$

$$\text{Trailing Edge} = (C_3 \bullet C_6) + C_4$$

where the conditions C_i are defined as

$$C_1 = (B_{i-2} > T_1) \bullet (B_{i-1} > T_1) \bullet (B_i > T_1)$$

$$C_2 = (B_{i-2} \geq T_2) \bullet (B_{i-1} \geq T_2) \bullet (B_i \geq T_2)$$

$$C_3 = (B_{i-2} < T_3) \bullet (B_{i-1} < T_3) \bullet (B_i < T_3)$$

$$C_4 = (B_{i-2} < T_4) \bullet (B_{i-1} < T_4) \bullet (B_i < T_4)$$

$$C_5 = (D_{i-1} > S_1) \bullet (D_i > S_1)$$

$$C_6 = (S_2 < D_{i-1} < S_3) \bullet (S_2 < D_i < S_3)$$

B_i is the absolute FADC value for the time slice i and D_i is the difference between two consecutive time slices i and $i-1$. T_i and S_i are the thresholds and the slopes downloaded to specific memory location to each FADC channel over the local area network token ring system. The determination of these thresholds and slopes is performed before beginning a data run by measuring the baseline and its fluctuations. Baseline samples are collected with a random trigger for each channel. The pedestal averages and their standard deviation is computed. Figure 16 shows the average pedestal value and the standard deviation for a sample of channels in the Theta chamber. The absolute baseline pedestal value can be electronically preset

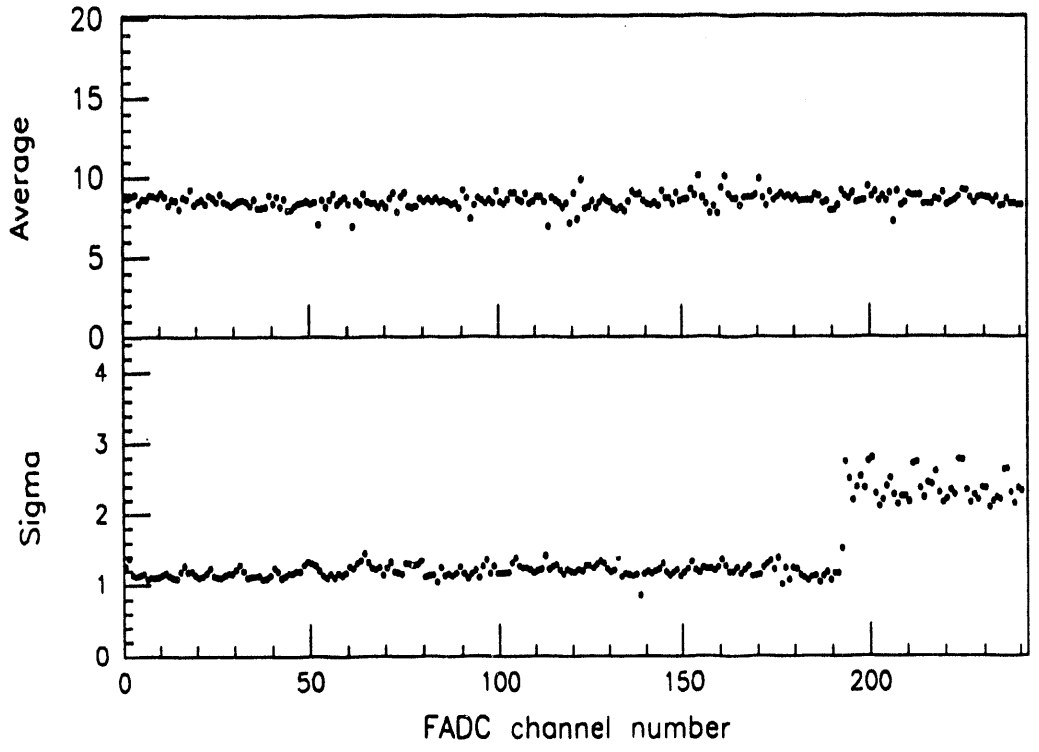

Figure 16. Pedestal average and sigma in units of FADC counts.

for each FADC channel. Typically they are set to 9 FADC counts on a scale of 0 to 255. The standard deviation reflects the background noise on that channel. The group of channels with a large sigma shown in the figure are delay lines which are operated at larger gain. The zero suppression thresholds T_i and slopes S_i for a given channel are determined as a function of the average pedestal value and its standard deviation. The parameterization used for their determination are

$$T_i = \text{Pedestal} + L_i \times \text{Sigma}$$

$$S_i = M_i \times \text{Sigma}$$

The coefficients L_i and M_i were determined using an offline program simulating

the FADC zero suppression chip. Non zero suppressed data were suppressed using the simulation program with a range of coefficient values. The coefficients L_i and M_i are chosen so as to minimize the amount of data collected and maximize the number of real hits found. The parameterizations are then used by the online calibration program to determine new zero suppression parameters at regular intervals.

It should be noted that when the trailing edge of a pulse has a very slow slope, the zero suppression algorithm is occasionally not triggered. The chip algorithm requires three consecutive bins, the difference between adjacent bins being an integral number of FADC counts. Thus the minimum difference allowed is one FADC count. If the trailing edge slope is slower, the chip algorithm fails to trigger resulting in occasionally long tails. The shaping functions have therefore been optimized to provide faster fall time of the analog pulse in order to avoid long trailing edges.

Channel to channel fluctuation in the pedestal baseline is within a few percent of the average. The pedestals have been monitored over a long time range and no significant pedestal shifts have been observed. The pedestal average and sigma are also used in the offline analysis for determination of the thresholds needed for locating a hit. The standard deviation of the pedestal distribution is typically 1.2 counts with the whole chain of electronics connected. This can be compared with 0.5 counts when all input signals from the FADC are disconnected.

Calibration of the relative gain of each channel is essential for the dE/dx corrections. The electronic calibration involves pulsing the preamplifier with various known inputs and measuring the output integrated area and peak pulse height. This has been done to study the bilinear properties of the FADC where above a certain

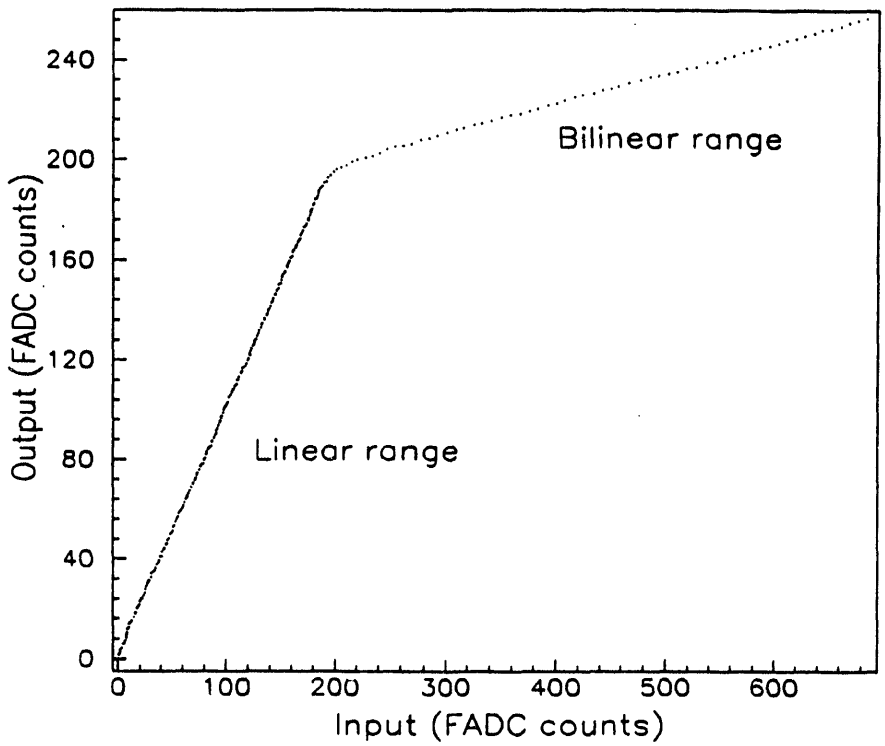

Figure 17. Bilinear characteristics of a FADC channel.

breakpoint, the pulse amplitude is attenuated to achieve an overall $9\frac{1}{2}$ bit FADC resolution. Figure 17 shows the output peak height as a function of the input pulse. The two regions above and below the breakpoint amplitude are clearly visible. The relative gain corrections applied to data has however been done by measuring the energy lost by minimum ionizing particles in the chamber. This technique includes fluctuations in gas gain in addition to the relative variations in electronic gain.

Variations in differences in cable lengths and relative electronic delays between channels can contribute to the mismeasurement of the absolute arrival time of the electrons at the sense wires. The TØ measurements, which provide a relative time

correction for each channel have been extensively studied using both electronic pulses and data. A test pulse injected at the input of the preamplifier at a known time to all channels can be used to determine the relative time offsets between channel. The TØ thus determined is used to correct the relative arrival time of the pulse at the sense wires. The TØ's can also be found from data by plotting the arrival time distribution over the length of the cell. The distribution for each wire is flat with sharp cut offs at the cell boundary and the sense wire plane. Linear correlations between the TØ's determined using both the above mentioned techniques have been observed. Extensive studies have been performed to understand the TØ measurements and its effect on data and are described in detail elsewhere [50].

3.2 Calibration of FDC

The forward drift chamber has been extensively tested in the Neutrino-West Area (NWA) located in the neutrino line at Fermilab. The accelerator operating in fixed target mode, supplies electron and pion beam in the energy range from 10 GeV to 150 GeV to NWA. The data were taken during the period from March 1990 through July 1990. A total of 3 million triggers were taken during this period. Measurements of spatial resolution, two track separation and energy loss response have been made under various conditions. The experimental setup and the performance of the chamber will be discussed in this section.

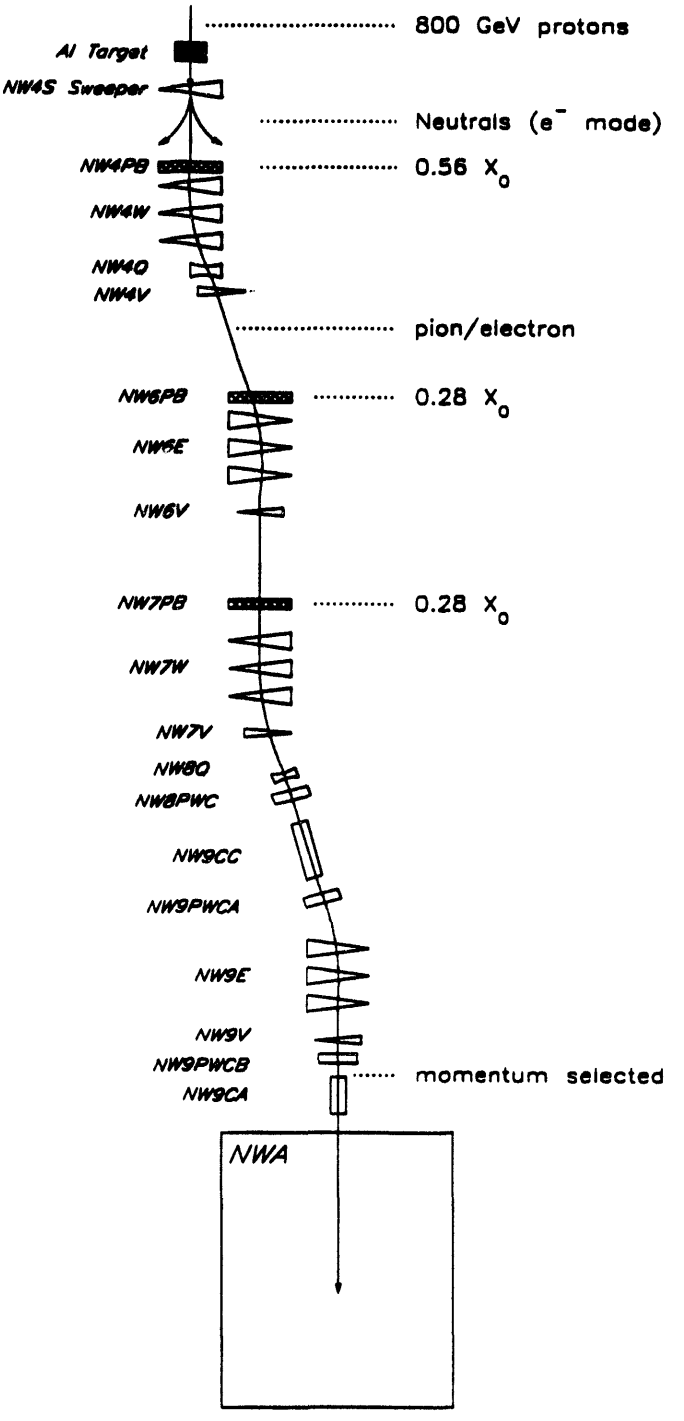

Figure 18. Layout of the neutrino secondary beam line at Fermilab.

3.2.1 Beamline

Primary protons at 800 GeV/c from the Tevatron are extracted into the neutrino beamline [51] on to an Aluminium production target. The secondary beam produced is used to provide a clean hadron and electron beam. The secondary beam line, shown in Figure 18, consists of dipole bend magnets and quadrupole focussing magnets to steer the beam. Target wheels with thin lead sheets mounted on them are located at appropriate points along the beam line. A sweeper magnet at the entrance of the secondary beamline sweeps away the charged particles. The resultant gammas convert in lead sheets producing pairs. Negatively charged particles (electrons) are then steered down the beamline to NWA. The background contamination in the electron beam is negligible over the mentioned energy scale. A small fraction of the background comes from muons. A pion beam is produced by shutting the sweeper magnet off and inserting thin lead sheets into the secondary beam line to scatter off the electrons. The negatively charged pions are then steered to NWA. At energies below 10 GeV, there is a large contamination coming from electrons.

Proportional wire chamber (PWC) measure the coordinates of the track along the beamline. Each PWC consists of 64 parallel wires separated by 2 mm and oriented in the plane perpendicular to the beam. A pair of PWC's located adjacent to each other are oriented perpendicular to each other to measure the x and the y coordinate. The PWC's located upstream and downstream of the bend magnet (NW9E) were also used to measure the momentum of the beam. Individual segment fits from PWC measurements in the upstream and downstream sections yield the bend angle of the track. The momentum of the beam is given by $p = 0.3\rho \int Bdl$

where B is the magnetic field in Tesla, ρ is the radius of curvature in metres and the integral is over the length of the bend magnet in metres.

Particle identification was provided by two Helium Čerenkov counters. The NW9CC and the NW9CA Čerenkov counters are located upstream and downstream of the last bend magnet prior to the particle entrance into NWA hall. The NW9CC and NW9CA counters are 70m and 30m respectively with a 12 inch diameter pipe. For threshold gas counters, the angle θ of emission of Čerenkov light is given by the relation [52]

$$sin^2\theta = \beta_t^2\left(\frac{1}{\beta_t^2\gamma_t^2} + \frac{1}{\beta^2\gamma^2}\right)$$

$\beta_t\gamma_t$ is the threshold momentum of the charged particle and can be expressed in terms of the pressure of the gas.

$$\beta_t\gamma_t = \frac{1}{\sqrt{n^2-1}} = \frac{1}{\sqrt{2\eta}} = \left(\sqrt{\frac{2\eta P}{P_0}}\right)^{-1}$$

$\eta = n - 1$, n is the refractive index of the gas, P is the pressure and the subscript 0 refers to the values at atmospheric pressure. From the above expression, the threshold momentum of the particles falls with increasing pressure. For most of the operations, the Čerenkov pressures were set such that they were just below the pion threshold.

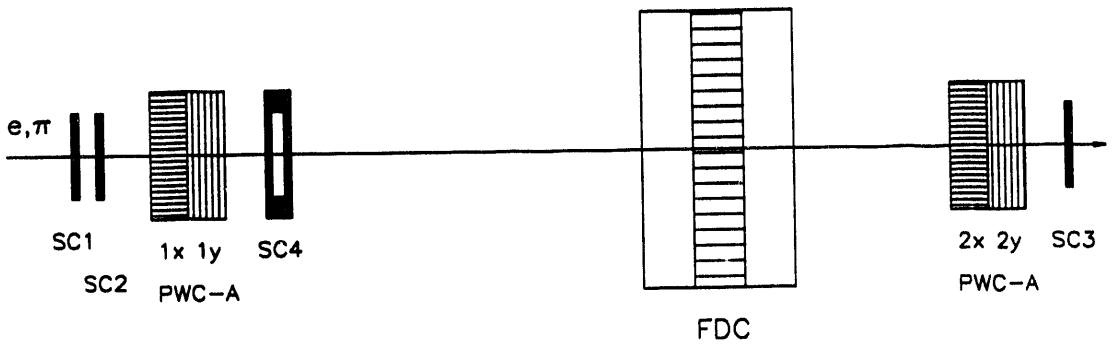

a) Experimental setup for performance study of the FDC

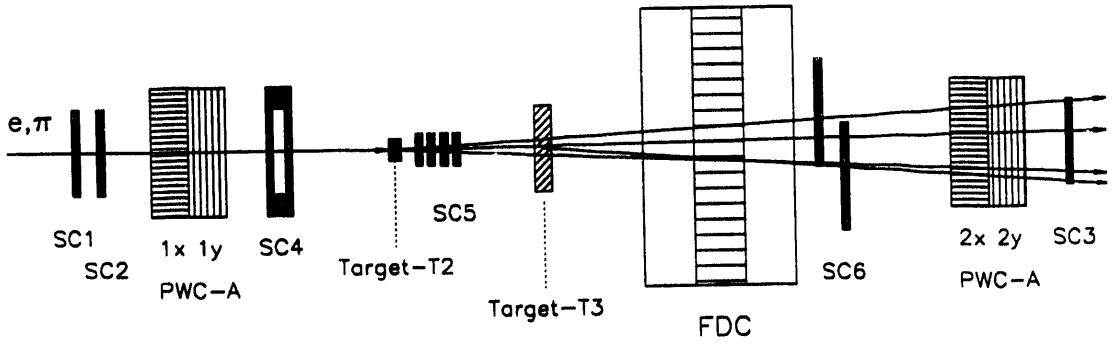

b) Experimental setup with targets in beam line

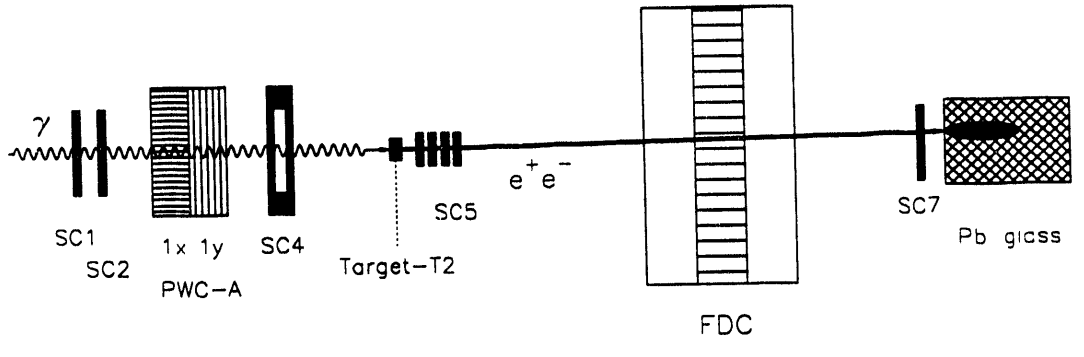

c) Experimental setup with photon beam

Figure 19. Forward drift chamber setup for various configurations at the test beam experimental hall.

3.2.2 Trigger

The data collected over the three month period is divided into three broad categories. Each category, shown in Figure 19, used a different set of trigger condition involving scintillation counters SC1 through SC7 placed in the beam line. Each of these categories is explained in detail below.

Data were collected to study the performance of the forward drift chamber. This included measurement of efficiencies, spatial resolution and high voltage scans to determine the optimum operating voltage. The trigger for this study (Figure 19a) used three scintillation counters, SC1 and SC2 located upstream of the chamber and SC3 located downstream of the chamber, in coincidence. A halo counter SC4 was used as a veto to reject stray particles coming down the beam line.

The second type of trigger (Figure 19b) was employed for data collected with targets in the beam line. The Target T2, located at the equivalent interaction point during the collider running, was used to simulate an interaction. This provided a mechanism to study high multiplicity events. A second target T3 was placed in front of the chamber to simulate the amount of material, principally in the vertex chamber electronics and supports, that would be present during the collider operation. This is helpful in estimating pair production from gamma conversions occurring before the FDC. Data was collected with target T2 alone and with both Targets T2 and T3. An array of four 2" x 2" scintillation counters (SC5) located immediately after the target T2 was used in coincidence with SC1 and SC2 located upstream and SC6 located downstream of the chamber. The discriminator threshold setting for the SC5 counters were set higher than nominal to ensure a higher probability of the

incident particle interacting with the target.

A photon beam was generated to study the efficiency of identifying overlapping pairs from gamma conversions. The Target T1, located before the last bend magnet (NW9E) prior to the particle entrance into NWA, was used to generate a photon beam. The bremsstrahlung of electrons incident on the target T1 produced gammas which were converted using the Target T2. Charged particles were swept away by the last bend magnet. The trigger (Figure 19c) involved a veto of the upstream counters SC1 and SC2 and a coincidence of the counters downstream of the target T2, SC5 and SC7. A lead glass calorimeter was placed behind the counter SC7 to obtain the photon energy spectrum.

The final trigger into the Level-1 framework used an additional beam gate. A free running clock operating at 200 kHz initiated a digitization of the FADC every five microseconds. The trigger window, shown in Figure 20, vetoed any trigger that would arrive later than 2.5 microseconds after digitization of the FADC has begun. This was done to ensure that the maximum electron drift time of 2.5 μs in the chamber would always be included in the readout.

3.2.3 Low energy mode

During the 1991 fixed target run, the response of the chamber to low energy pions was studied. The energy loss measurements and comparison to predictions is discussed in the next chapter. The test beam line was further modified to generate electron and pion beams with energies between 1 and 10 GeV. The low energy beam [53] was obtained by retargetting the beam in the NW8 enclosure. An ad-

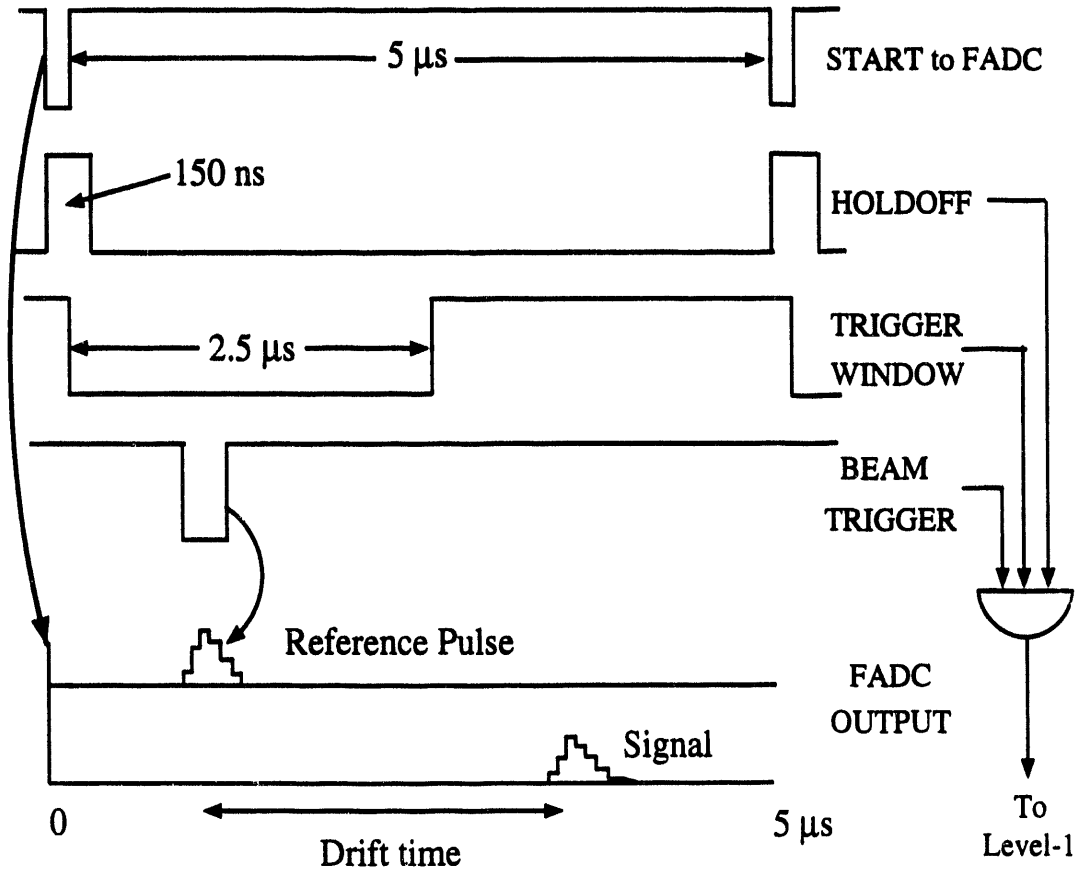

Figure 20. Trigger synchronization at the test beam.

ditional dipole bend magnet was added in that enclosure to select the momentum of the particle. Upstream targets could not be used for this purpose since the pion survival rates become negligible at low energies. The existing Čerenkov counters operating just below the pion threshold provided good separation between pions and electrons. At these low energies, muons were an additional source of background arising from pion decays. A Freon Čerenkov counter was added downstream of the tracking chamber which provided additional rejection against muons. A scintilla-

tion counter based trigger was used as before while operating in the low energy node similar to that shown in Figure 19a.

3.2.4 Track reconstruction

The data analysis uses a sophisticated hit finding and track fitting algorithm. The zero suppressed FADC output contains clusters of data as described previously. Figure 21 shows a typical raw FADC output containing such clusters for 16 wires of a Phi chamber cell.

Each cluster consists of pulse height information for each FADC bin (9.434 nsec). The software hit finding utility determines the beginning and end position of a pulse by looking at differences between adjacent bins and comparing them to threshold conditions. Each FADC bin is weighted by $(0.6)^n$, where n is the FADC bin number from the start of the pulse. This gives more importance to FADC bins from the first drift electrons in the cluster which improves the resolution. The leading edge of the pulse is determined by obtaining the centre of gravity of the cluster between the beginning and the peak of the pulse. This technique obtains the position of the pulse to better than the width of a FADC bin. The pulse area of a given cluster is obtained by integrating the pulse height information between the start and the end of the cluster. A reference trigger pulse, indicating the time of occurrence of the trigger during a digitization cycle is digitized by a separate FADC channel. This is used to correct the time to give the absolute time of arrival of the pulse. The process is repeated for all channels and the hit information on each channel is stored.

The next step of the analysis uses the above hit information to fit tracks. The

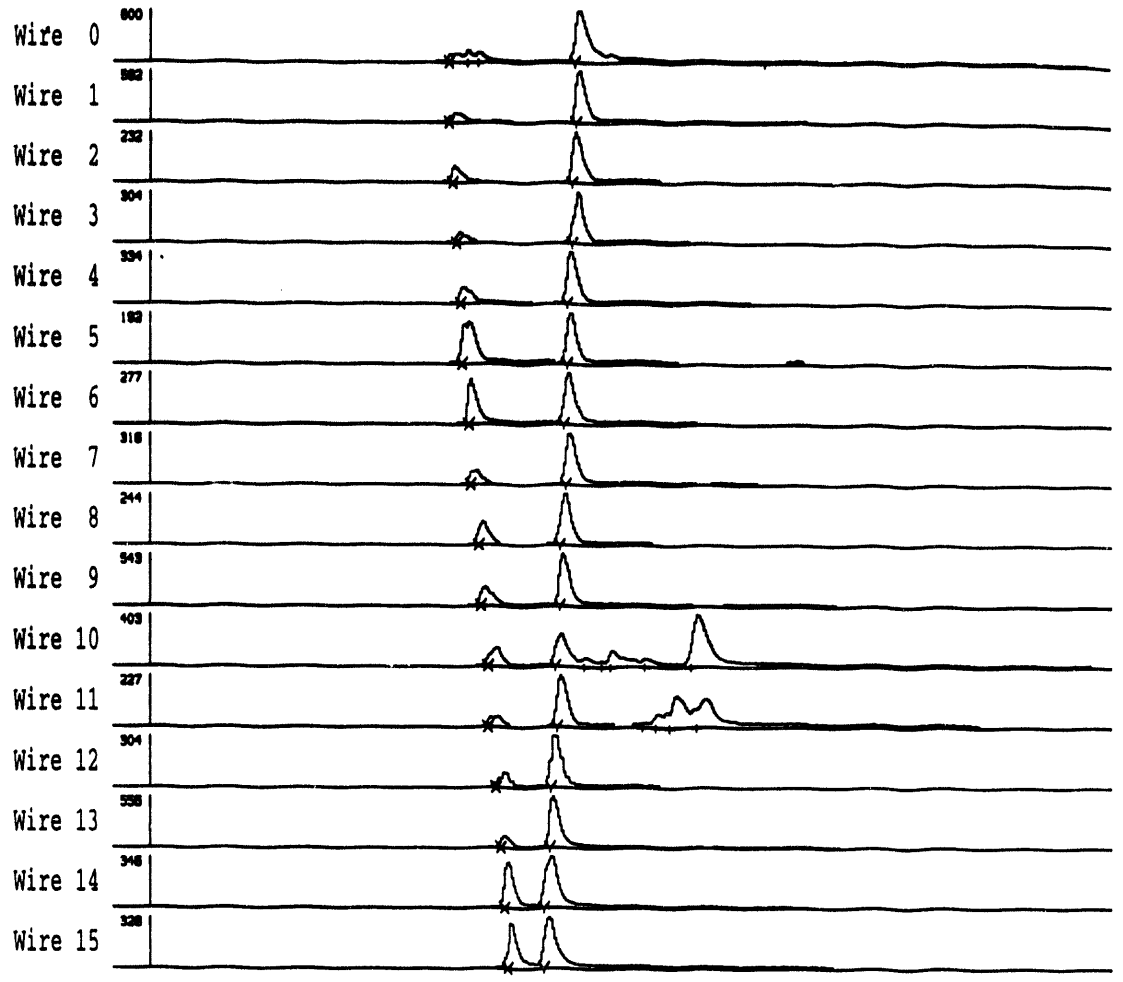

Figure 21. Typical raw zero suppressed FADC output. The above display shows two track segments in a Phi Chamber cell, the left segment is a singly ionizing track, the right segment is an e^+e^- pair corresponding to a doubly ionizing track.

details of track fitting are discussed elsewhere [54]. Tracks are formed across the three layers of the FDC, the two outer Theta layers and the Phi layer. The technique adopted for track reconstruction utilizes the road method. This technique uses two hits, one each on the first and the last wire in a cell to form a road. If more than 75% of the maximum number of hits in a given layer is found on the road, the hits

are then used to form a track segment in a layer. A given track requires a track segment to be present in at least two out of the three layers. The number of hits in a track can therefore vary between 18 and 32. The hit by itself does not carry the information from which side of the sense wire it originates. Due to the staggering of wires, the hits on the mirror side of the cell would be staggered more than the real side. Fewer hits would lie on the formed road on the mirror side than on the real side. A further cut on the chi square of the track ensures with a high efficiency that the track on the correct side of the cell is formed.

3.2.5 Performance

The spatial resolution of the chamber is determined by identifying a track in the chamber and computing the residual to each sense wire, which is the difference between the position of the hit found by fitting a track without including the hit in question and its measured position. The standard deviation of the residual yields the spatial resolution. There are three main contributions to the spatial resolution.

The main contribution to the resolution is a constant term which comes from the electronics. The limitations in digitization resolution (10 nsec) has a direct effect on the time resolution. Other sources such as electronic noise and cross talk effect the precise location of the arrival time of the pulse.

The second contribution comes from electron diffusion which varies with drift distance. A localized cluster of charges drifting in the chamber diffuses by collisions with other atoms in the gas. The fraction of charges found after a given time t follows a Gaussian distribution in the absence of other effects. The time spread of

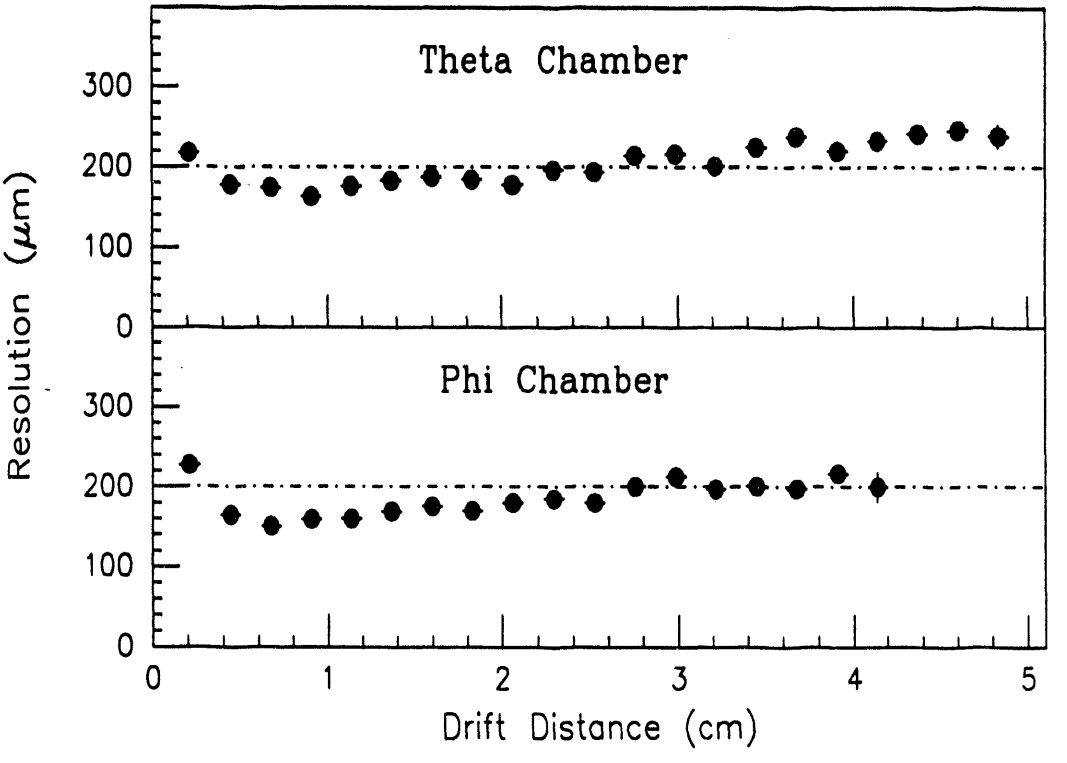

Figure 22. FDC spatial resolution as a function of drift distance.

the charges is then given by $\sqrt{2Dt}$, where D is the diffusion constant. It follows that the resolution of the chamber will worsen as the square root of the drift distance in the chamber.

The third contribution is the finite statistics of the primary production ion pairs. The primary ion production follows a Poisson distribution and fluctuations in the production statistics can cause the centroid of the pulse to shift leading to a mismeasurement of timing. Further complications are caused by the presence of large clusters produced due to the Landau effect.

Other systematic contributions such as non uniform electric field especially at

cell boundaries, small fluctuations in gas composition, changes in pressure and temperatures contribute to the spatial resolution of the chamber.

The resolution for both the Phi and the Theta chamber have been measured against drift distance and is shown in Figure 22. At drift distances less than 1 cm, the resolution worsens with small drift mainly due to primary ionization statistics caused by non uniform field between the sense and the guard wires. At drift distances larger than 1 cm, the effect of diffusion with larger drift is clearly visible. The overall spatial resolution for both the Phi and Theta chamber is better than $200\mu m$.

The three main individual contributions to the spatial resolution as described above are related with the equation [55]

$$\sigma^2 = \sigma_E^2 + \sigma_D^2 + \sigma_S^2 \tag{3.1}$$

where the subscripts E, D and S refer to the contributions from the electronics, diffusion and ionization statistics respectively and σ is the overall spatial resolution. For large drift distances, the statistics term does not make a contribution. The electronics term is independent of the drift distance and is mainly due to the finite resolution of the FADC's and noise sources. The data was fit with the function of the form

$$F(t) = \sqrt{C_1^2 + C_2^2 t + C_3 exp(-C_4 t)} \tag{3.2}$$

C_1 represents the electronic contribution, C_2 is related to the longitudinal diffusion and the last term describes the statistical flutuations in the number of ions produced close to the sense wire. The results of the fit and individual contributions are shown

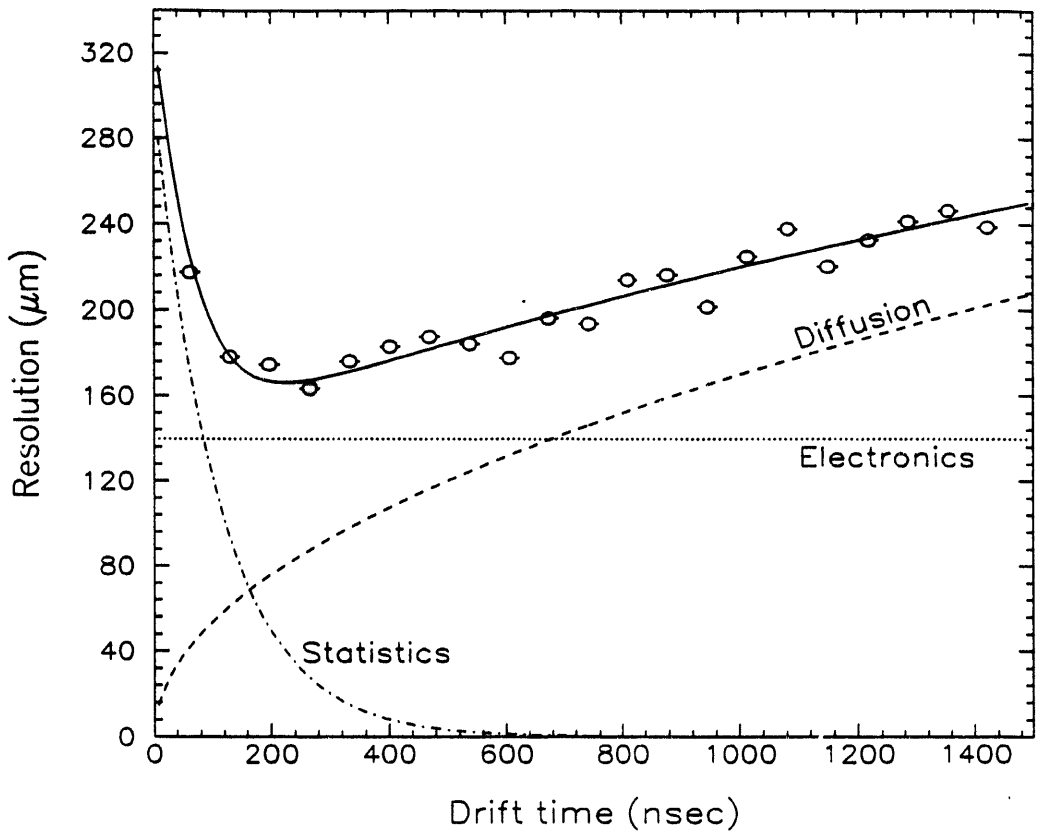

Figure 23. Individual contributions from electronics, diffusion and ionization statistics to the spatial resolution. The fit to the data is done by adding up the contributions in quadrature as indicated in equation 3.1.

in Figure 23. From the fit, we obtain

$$\sigma_E = 139.73 \pm 9.57\ \mu m.$$

$$\sigma_D = \sqrt{28.815(\pm 0.114)t} \qquad (3.3)$$

From equation 3.3, we obtain σ_D of 90 μm for a 1 cm drift operating at 1 atm. pressure. These observations are consistent with the earlier observations made with the prototype drift chamber [35].

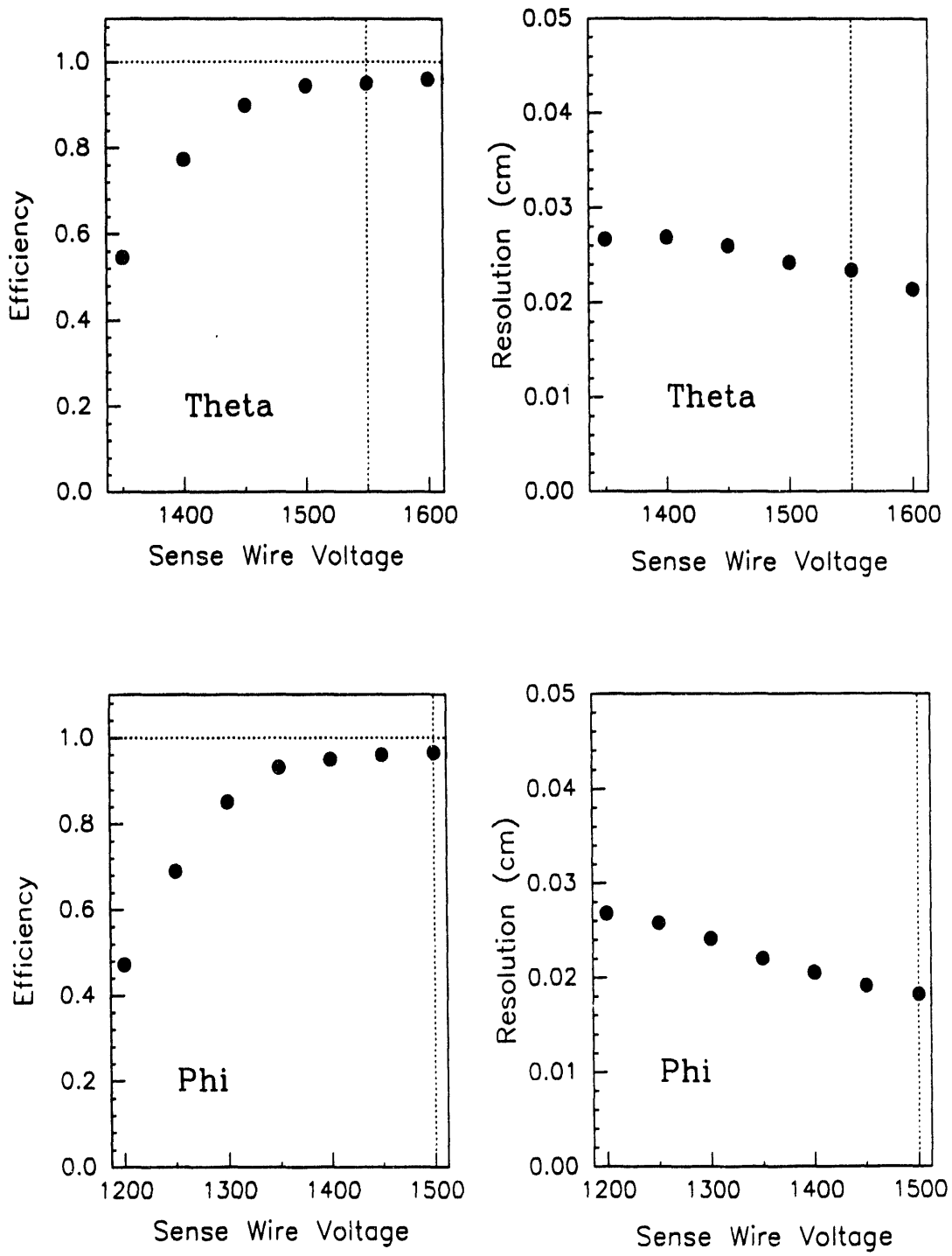

Figure 24. FDC efficiency and resolution as a function of high voltage.

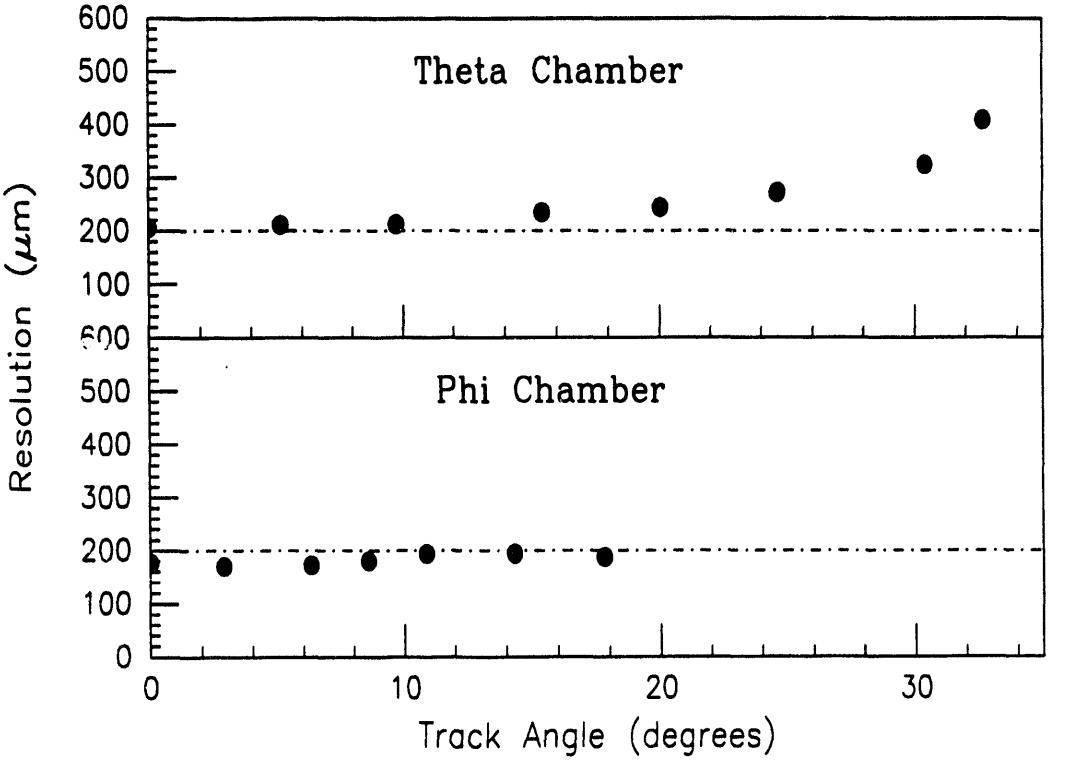

Figure 25. FDC spatial resolution as a function of track angle.

Figure 24 shows the efficiency and the spatial resolution of the chamber as a function of the sense wire high voltage. The vertical dashed line reflects the nominal operating point of the chamber. The average hit efficiency drops with lower sense wire voltage due to a smaller charge collected at the sense wires and less gain such that the signal is overwhelmed with the noise. With an increase in the charge collection at the sense wires, the hit efficiency is 95% at the nominal operating point. The spatial resolution of the chamber improves with more charge collected at the sense wires. Figure 25 shows the resolution of the chamber as a function of the angle of the track with respect to the sense wire plane. The resolution is fairly uniform up to an angle of 20° where it starts to worsen since the arrival time of the

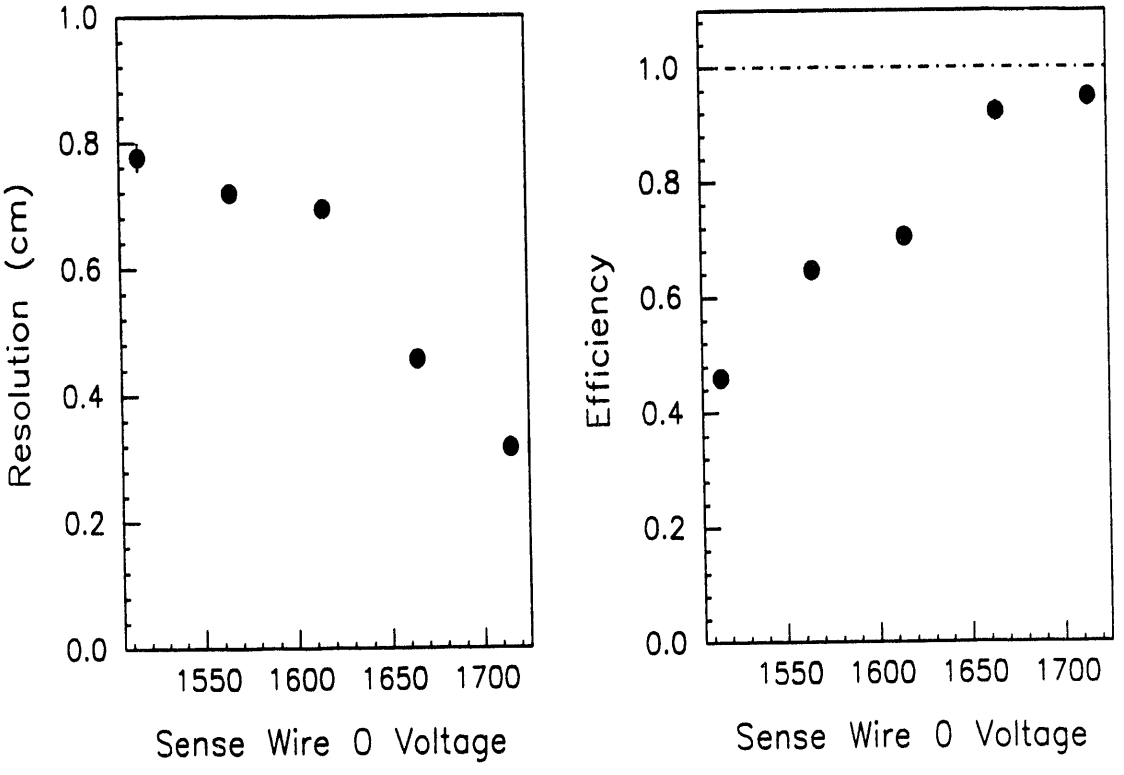

Figure 26. Delay line resolution and efficiency.

electrons is spread out more.

Each Theta cell has one delay line which measures the position of the track along the sense wire plane. Each Theta cell has eight sense wires (SW) numbered 0 through 7. The delay lines are located at one end of the cell closest to SW0. The accumulation of charge on SW0 induces an opposite polarity charge on the delay line. For this reason, SW0 is operated at a higher voltage than the other sense wires in the same cell. This considerably improves the efficiency and the resolution of the alternate coordinate readout as shown in Figure 26. A delay line resolution of 2 mm at 95% efficiency is obtained with SW0 operating at 10% above the nominal

operating point of the other sense wires.

The measurement of electron drift times to obtain the spatial coordinates of a track requires a uniform electric field and a constant drift velocity. The drift velocity in DØ gas attains a constant value and is insensitive to small fluctuations in electric field. This allows a linear space time correlation over the full length of the chamber. Figure 27 shows the drift distance as measured by the PWC system against drift time measured in the chamber. The relationship is linear over the length of the cell. The slope of the curve yields an electron drift velocity in DØ gas of 34.5 μm/nsec. The nonlinear region of this curve for drift regions less than 1 mm corresponds to the drift region between the sense and the guard wires.

Extensive studies [54] have been done in measuring the efficiency with which two hits can be resolved. Figure 28 shows the hit efficiency as a function of the separation between two hits on a given wire. The two hit separation at 90% efficiency has been determined to be 2.5 mm.

3.2.6 dE/dx resolution

The truncated mean pulse height is calculated for each reconstructed track using the following steps.

- √ The integrated pulse area for each hit lying on a track is computed.
- √ Each pulse area is corrected for relative gains previously determined by using clean single minimum ionizing tracks.
- √ The average of the lowest 70% of the pulse height samples is determined. The higher pulse height samples are rejected to minimize the effect of the Landau

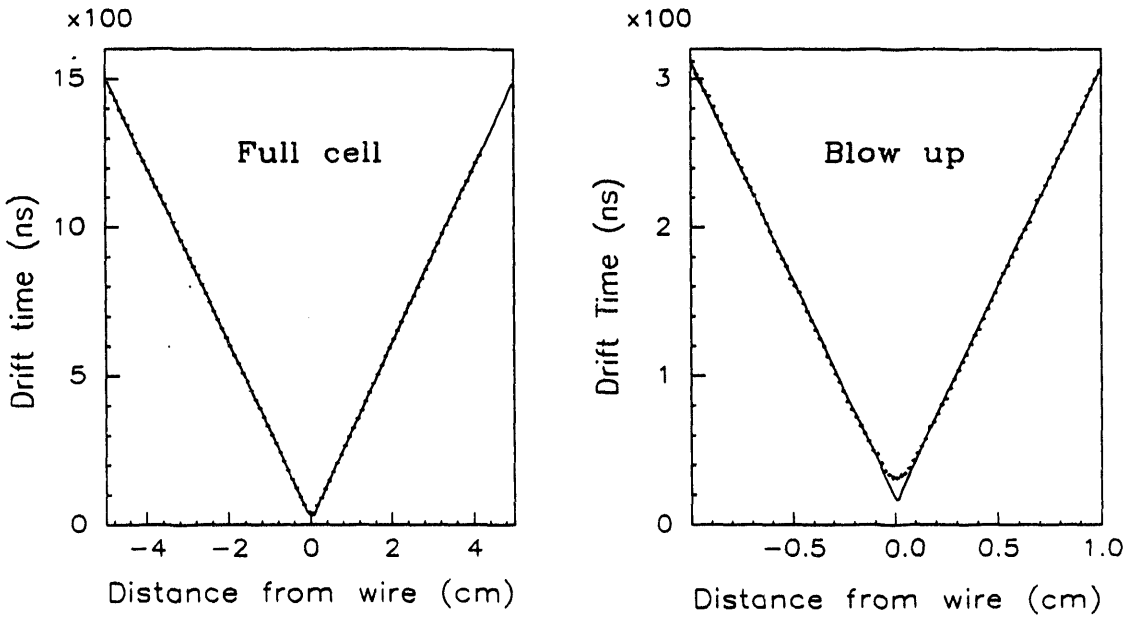

Figure 27. Space time correlation in FDC.

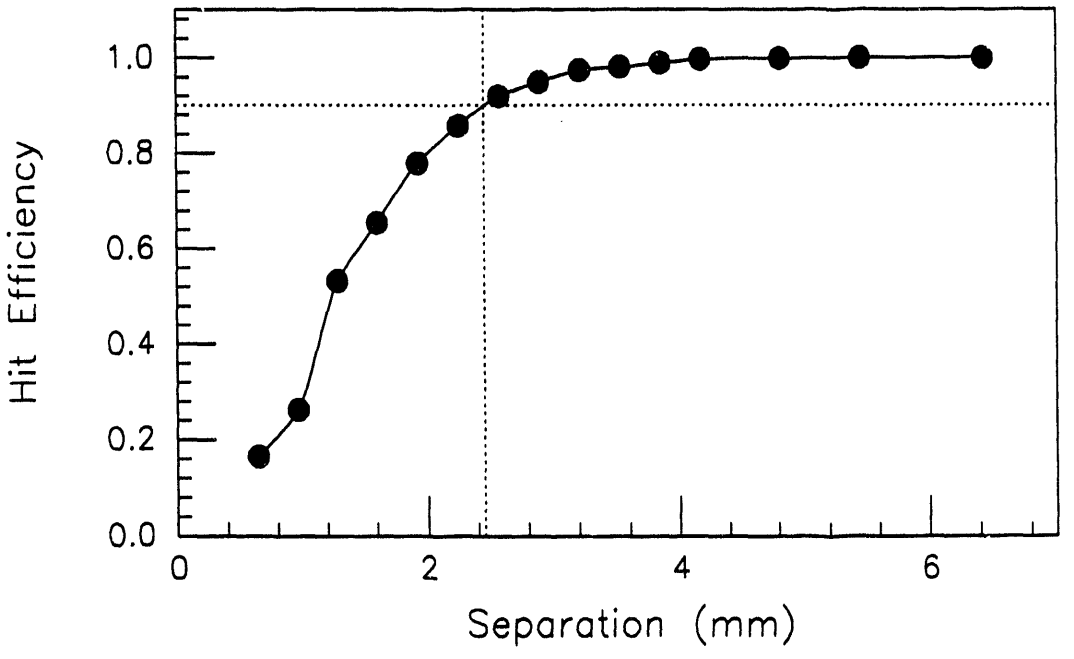

Figure 28. Two hit efficiency as a function of the separation of the two hits. The horizontal and vertical lines reflect the separation at 90% efficiency.

tail mainly caused by delta ray production.

- √ A geometric correction is applied to account for longer paths for tracks at an angle with respect to the sense wire plane.

- √ The average pulse area is further corrected for its dependence on the drift distance.

- √ The fit to the Landau distribution employs a combination of a Gaussian and an exponential function. The rising edge is approximated with a Gaussian function and the falling edge of the distribution with an exponential. The mean of the gaussian fit yields the most probable value of the distribution.

The dE/dx resolution $\frac{\sigma}{E}$ is determined by the scaled thickness of the sample $\frac{\alpha t}{I}$ where αt measures the number of primary ionization in the gas layer of thickness t. I is the effective ionization potential and corrects for the atomic shell effects. For a single sample, the resolution is given by [56]

$$\left(\frac{\sigma}{E}\right)_{FWHM} = 81\left(\frac{\alpha t}{I}\right)^{-0.32} \tag{3.4}$$

For a chamber with n samples, Walenta et al [56] demonstrated using a truncated mean analysis that

$$\left(\frac{\sigma_n}{E_n}\right)_{FWHM} = g(n)\left(\frac{\sigma_1}{E_1}\right)_{FWHM} \tag{3.5}$$

where $g(n) = n^{-0.428}$, n is the number of samples. The dE/dx resolution therefore improves as the $\sqrt{n}$. Using these equations, the r.m.s. resolution for n samples can

Table 12.–Characteristics of DØ gas.

Gas	Z	A	I_0 (ev)	ρ $(g-cm^{-3})$
Ar	18	39.9	15.8	1.66×10^{-3}
CH_4	10	16	13.1	6.70×10^{-4}
CO_2	22	44	13.7	1.86×10^{-3}
DØ[a]	17.8	39.067	278.2[b]	1.63×10^{-3}

[a]Effective values for DØ gas weighted by composition

[b]Effective ionization potential = $I_0 Z$

be expressed as

$$\left(\frac{\sigma}{E}\right) = 31.953 n^{-0.428} \left(\frac{\alpha t}{I}\right)^{-0.32} \tag{3.6}$$

Using Table 12, the expected r.m.s. resolution can be calculated in terms of n for the DØ gas, 93% Ar, 4% CH_4, 3% CO_2.

$$\alpha t = 0.153 \rho t \left(\frac{Z}{A}\right) = 0.0907 \times 10^{-3}\ \text{MeV}$$

$$\left(\frac{\sigma}{E}\right)_{predicted} = 49.234 n^{-0.428} \tag{3.7}$$

The maximum number of samples for a given track in the forward drift chamber is 32. The predicted r.m.s. resolution using equation 3.7 with 32 samples and 75% truncation is 12.63%. Figure 29 shows the pulse height distributions obtained at the test beam facility with 50 GeV pions with and without truncation. The effect of the Landau tail in the non-truncated distribution is clearly visible. The

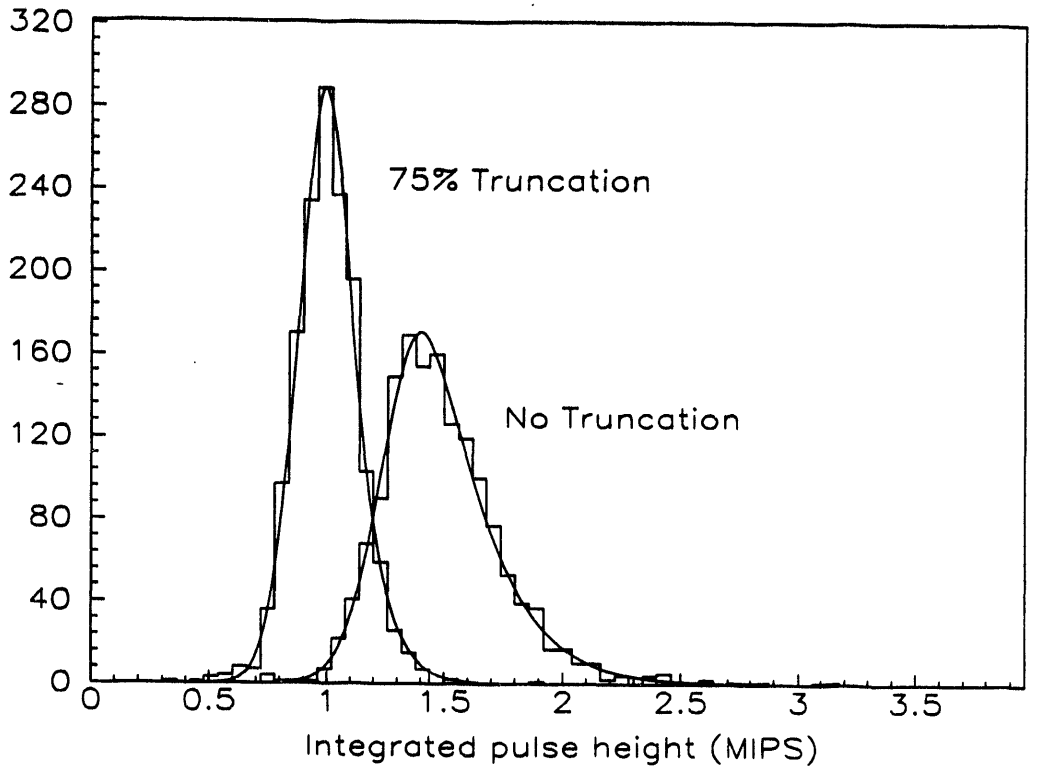

Figure 29. Pulse height distribution with 50 GeV pions.

truncated distribution retains 75% of the samples in a given track through the chamber. The resolution measured with 75% truncation is 13.3% which is very close to the predicted value. The number of samples in a given track is not fixed as it varies depending on the efficiency and other effects. Selecting events with the number of samples per track greater than 30, the measured resolution is 12.67% which is amazingly close to the predicted value. The most probable value of the truncated pulse height distribution shown in the figure has been normalized to one. The most probable value of the non-truncated distribution is greater than one which is an artifact of the normalization procedure.

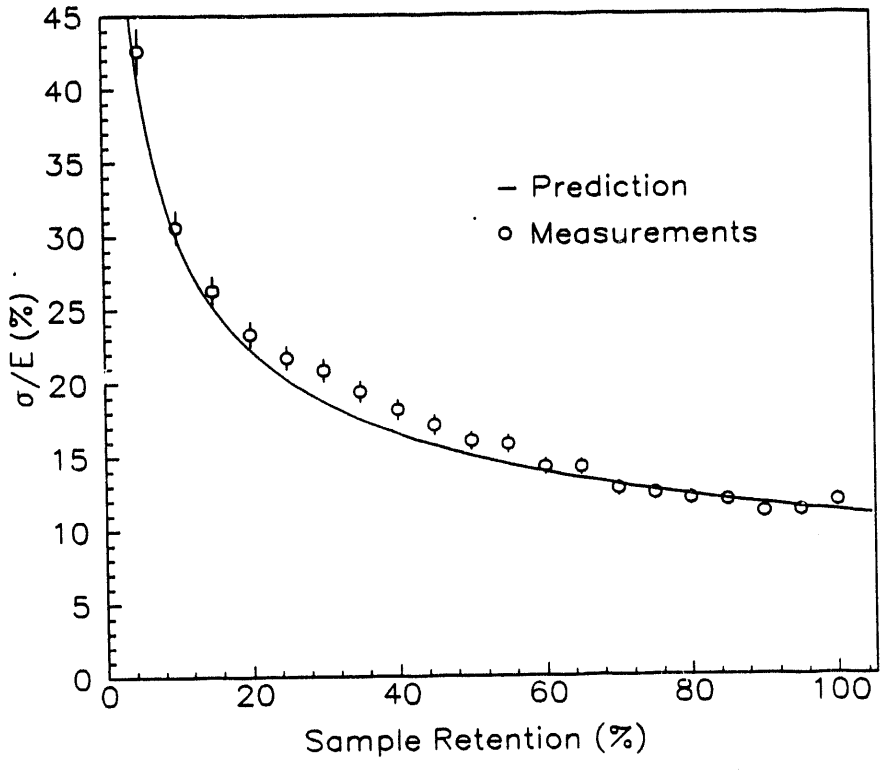

Figure 30. dE/dx resolution as a function of sample retention.

Figure 30 shows the r.m.s. resolution as a function of the sample retention. The solid line is the function (equation 3.7) describing the dE/dx resolution as a function of the number of samples . With the assumption that there are a maximum of 32 samples, the dE/dx resolution is calculated using equation 3.7. The open circles are the measured resolution with 50 GeV pion data. The resolution is slightly worse than predicted since a track in a given event may not always have 32 registered hits. As described in the previous section, a track may be formed with as few as 18 samples or as many as 32. For three layer tracks, where the track was successfully identified as going through the Phi and two outer Theta chambers, the average

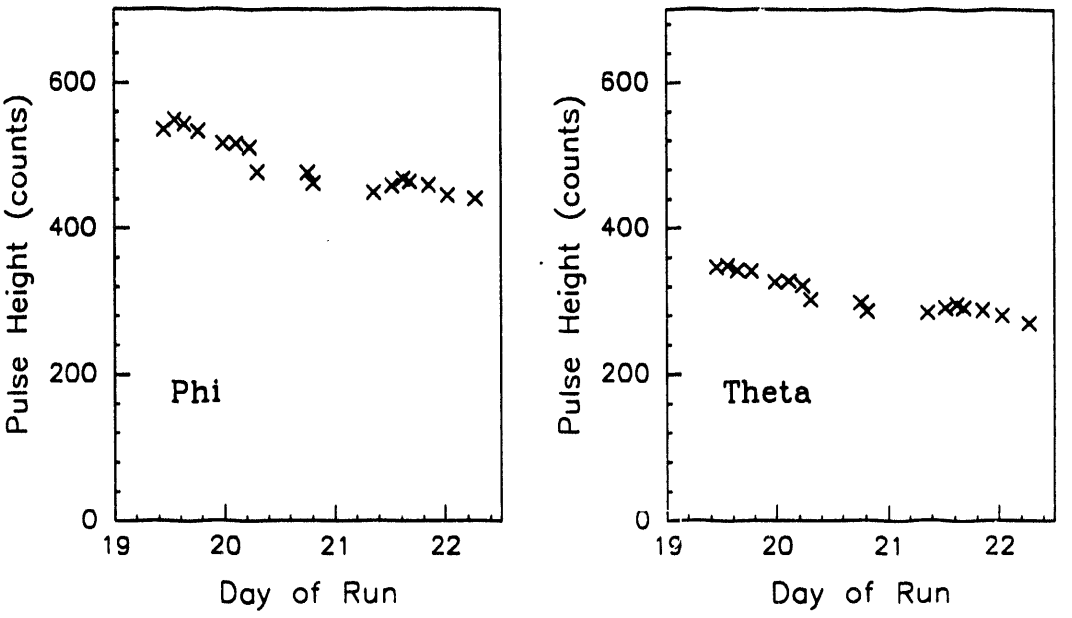

Figure 31. Fluctuation of pulse height with time.

number of samples is typically 30. The error bars shown in the plot are the errors in the mean and the standard deviation of the pulse height distribution added in quadrature and does not include the spread in the number of samples per track.

3.2.7 dE/dx corrections

The theta of the track generated by the track fitting algorithm was used to correct the angular dependence of the energy lost by an incident particle. A simple cosine theta dependence has been assumed for the correction.

Pressure fluctuations, gas flow and other effects lead to fluctuations in pulse height with time. Figure 31 shows the average truncated pulse height in the Phi and the Theta chamber over a three day period. The data was collected with 50 GeV pions. Fluctuations in pulse height by as much as 10% have been observed. In

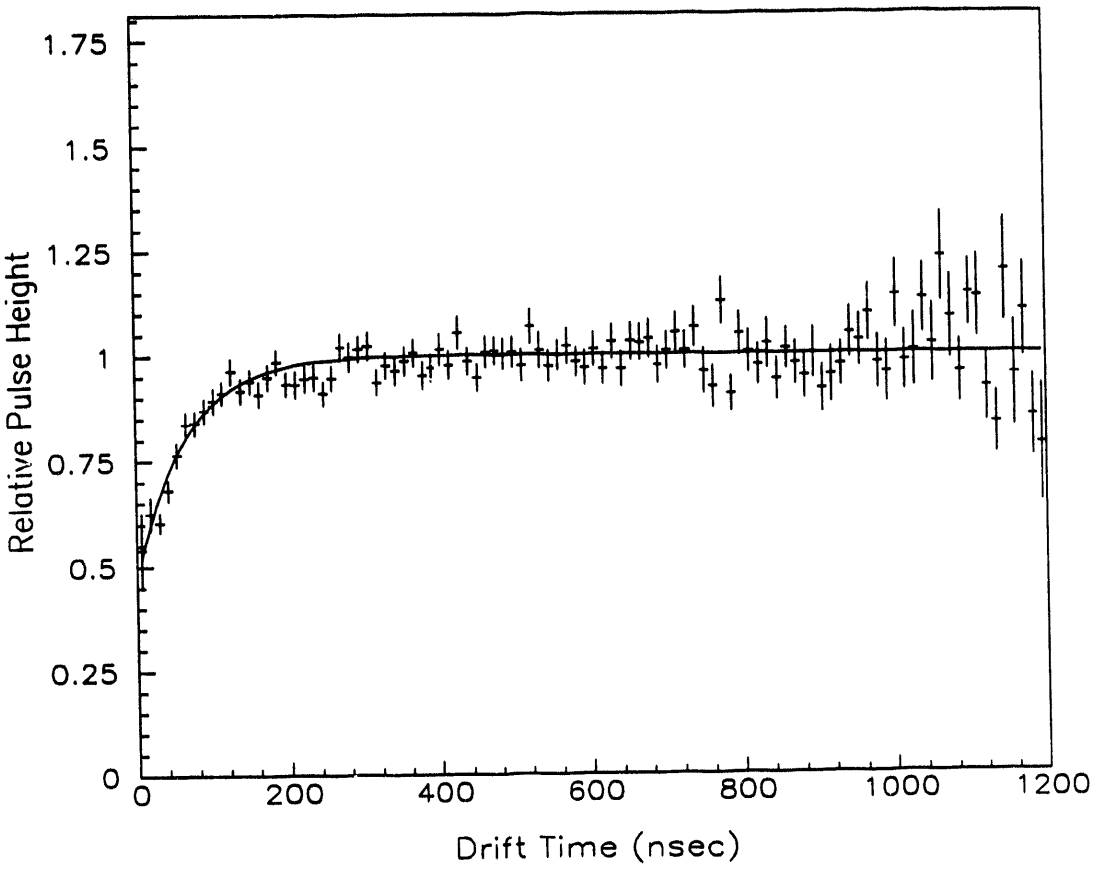

Figure 32. Dependence of pulse height on drift distance.

the real collider run these fluctuations would be corrected with the canary chamber connected to the same gas line which feeds the chamber. For the test beam data, information from the canary was not used as it was still under development. Corrections were made by reevaluating the relative wire to wire gain corrections using minimum ionizing particles with time.

The pulse height distribution over the length of the Phi and Theta cell is flat as shown in Figure 32. Close to the sense wire, the average pulse height drops due to a decrease in the secondary ionization production statistics. The variation is slightly

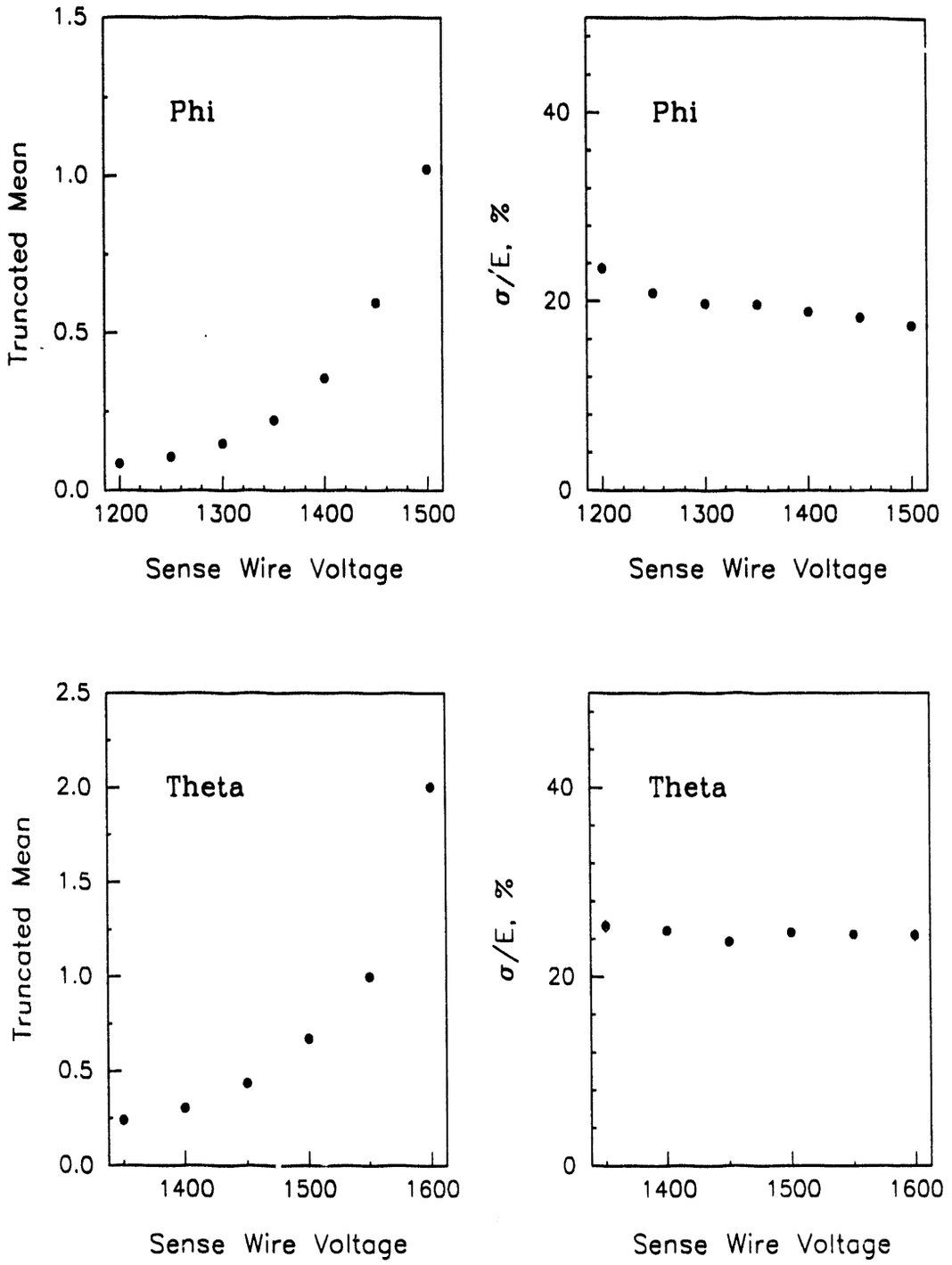

Figure 33. Pulse Height dependence on sense wire voltage.

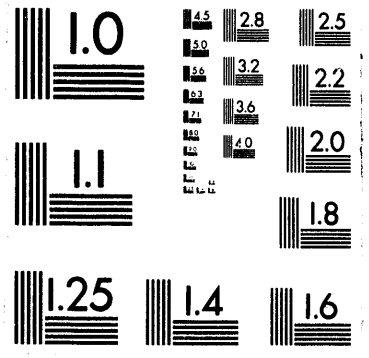
1.0
1.1
1.25
1.4
1.6
1.8
2.0
2.2
2.5
2.8
3.2
3.6
4.0
4.5
5.0
5.6
6.3
7.1

2 of 2

different from wire to wire. An average correction has been applied for the data reported here by parameterizing the dependence on drift distance with

$$F(t) = 1 - e^{-(0.643 + 0.03t)}$$

where t is the drift time in nsec. The average parameterization is shown superimposed on the figure.

The truncated mean pulse height has been calculated for various sense wire high voltage settings for the Phi and the Theta chamber. There is an exponential increase in the pulse height with an increase in the high voltage (Figure 33) due to an increase in the gas gain at the sense wire. The resolution shown is worse than what has already been quoted since these samples were collected either from the Phi or the Theta chamber and hence had fewer samples. The maximum number of samples in the Phi chamber is 16 and in the Theta chamber is 8. There are no significant changes in pulse height resolution seen in the chamber with changes in the high voltage.

3.3 Canary monitoring system

The forward drift chamber utilizes a separate standalone system to monitor variations in drift velocity and gas gain with time. The canary is a drift chamber connected to the same gas line which supplies the FDC. It uses radioactive sources located at precisely measured distances from the sense wire. This section explains the construction and operation of the canary.

3.3.1 Description

A Theta full cell was used as the canary for monitoring purposes. This gives the advantage of having the same electrostatic properties in both the canary and the FDC. The Theta cell as in the FDC consists of eight sense wires and a delay line. The sense wires are staggered to resolve left right ambiguity. Three Bismuth sources are placed at precisely measured distances on each side of the sense wire plane. A pair of finger scintillation counters are used to provide the trigger for each of the six sources. Each pair of counter are located on either side of the cell boundary in line with the bismuth source.

Figure 34 shows the canary and the location of the sources and counters. Bismuth was chosen as the source primarily because of its long half life of 32.2 years. Its primary β emissions are peaked at 0.482 and 0.976 MeV.

3.3.2 Trigger

The canary analog signals are shaped and digitized by the same electronics used for the FDC. The 106 MHz clock signal for the FADC is provided by a crystal oscillator. The digitization of the FADC occurs every 5 μs. A trigger is accepted if it occurs within the first $3\mu s$. Since the maximum drift time is $2\mu s$, this trigger window prevents occurrences where the signal would lie outside the digitization period. The signals from the counters are shaped with an RC circuit and also digitized by the FADC. This provides a reference time for the signals. A coincidence is required for each pair of counters corresponding to the six sources. These provide six possible trigger inputs to a VME based prescaler card [57]. The prescaler card has two

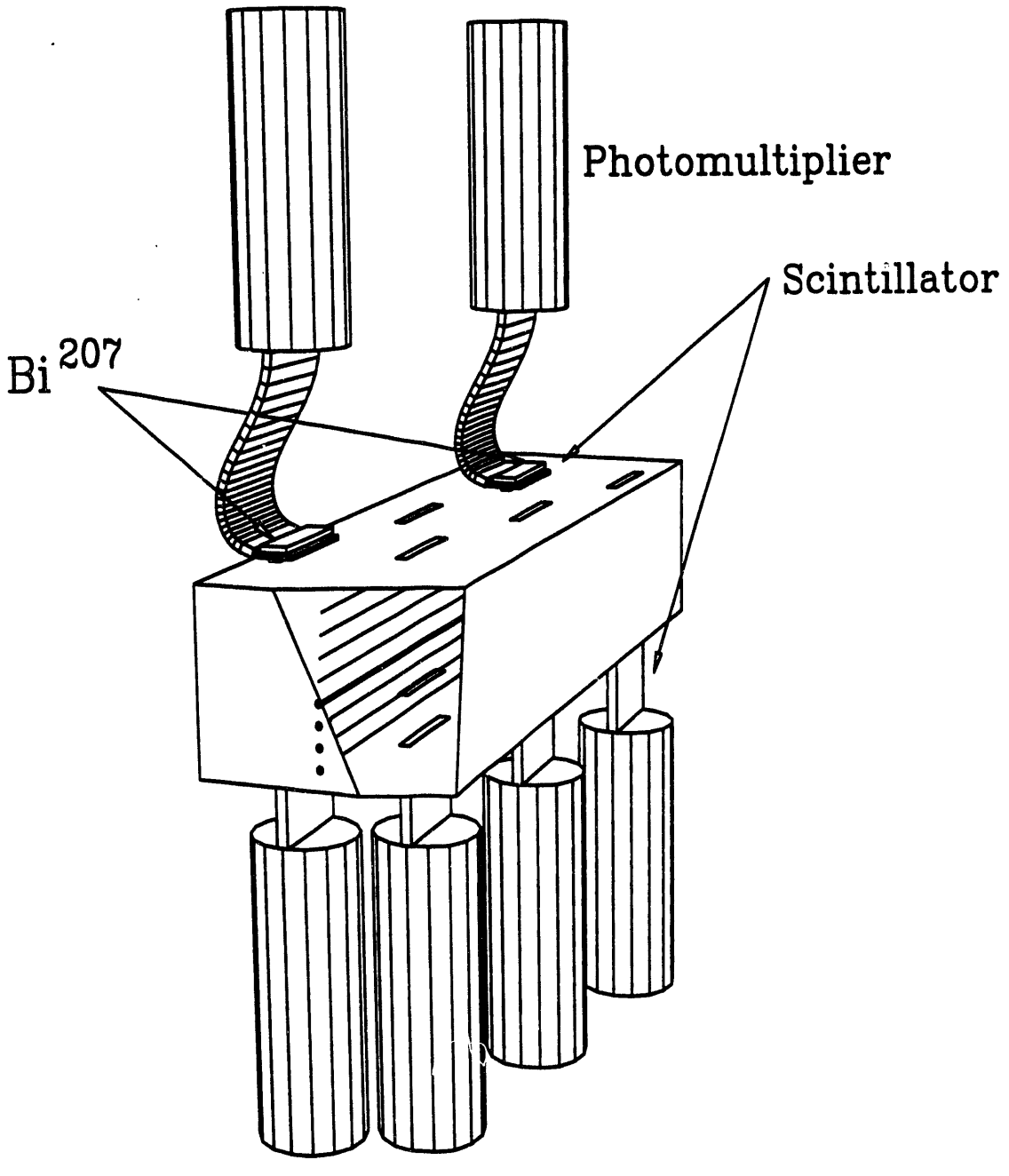

Figure 34. The FDC canary chamber. Six pairs of scintillators (not all shown) are placed on either side of a Theta Full cell. The sense wire in the cell are seen in the end view. The six Bismuth sources are placed on the top surface of the cell as shown.

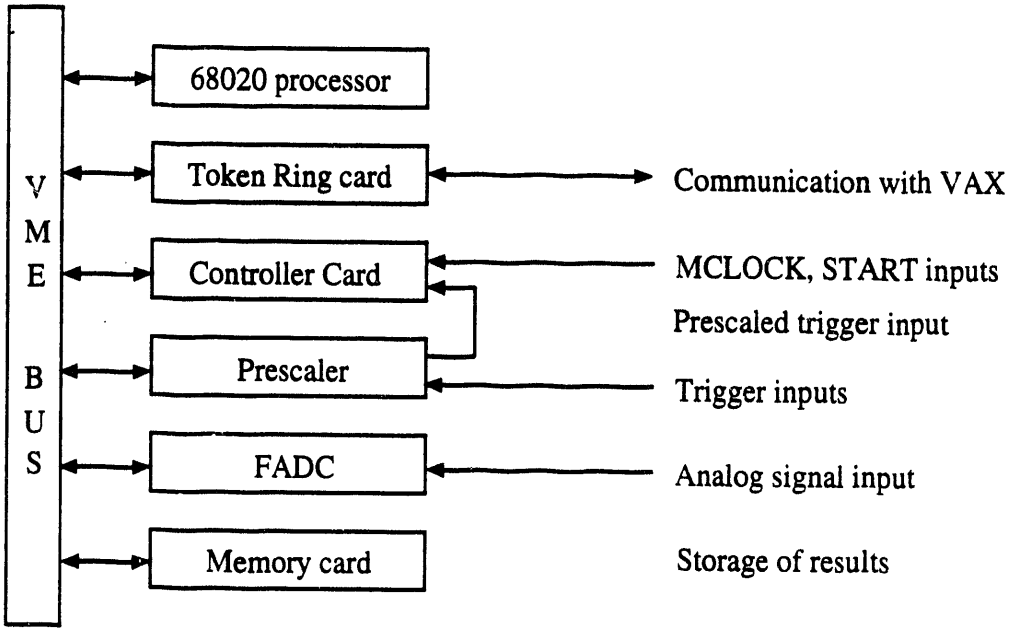

Figure 35. The canary data acquisition system.

functions. It prescales the incoming trigger by a preset programmable number. It also sets a bit in a 16 bit register which indicates which of the six counter pairs fired. The output of the prescaler card is a single OR condition of the above triggers which is fed into the controller card. Upon receiving the trigger, the controller card raises a busy signal which prevents occurrences of other triggers and initiates a suppression cycle. The busy signal is dropped after the completion of analysis of the current trigger.

The data from the FADC is stored in the back end memory on the FADC card. A schematic of the readout employed for the canary is shown in Figure 35. The token ring card shown in the figure allows communication between the VME crate and the host VAX program over an ethernet and token ring local area network.

3.3.3 Data collection process

The data collection and analysis task is performed by an application program running on a VME based Motorolla 68020 processor. The function of the application program is described in the following steps.

- Wait for a begin run command to be issued from the Host VAX.
- Determine whether a trigger has occurred by checking the status of the controller card.
- Read the data over the VME bus backplane from the back end FADC memory.
- Structure the data and store it in a memory card.
- Determine which of the six counters fired.
- Process the data to determine drift time and pulse height.
- Save results as histograms in the memory card.
- Increment memory counters to indicate its success.
- Clear latches and inform the controller card of its completion and wait for the next trigger.
- Repeat this process until the requested number of events have been analyzed.

The data control and monitoring is performed by another process running on the host VAX system. This process initiates a new run by downloading instructions to a memory location in the VME crate which is picked up by the application program. The application program increments a memory counter to indicate its progress and completion. The VAX program monitors this state and upon completion reads the

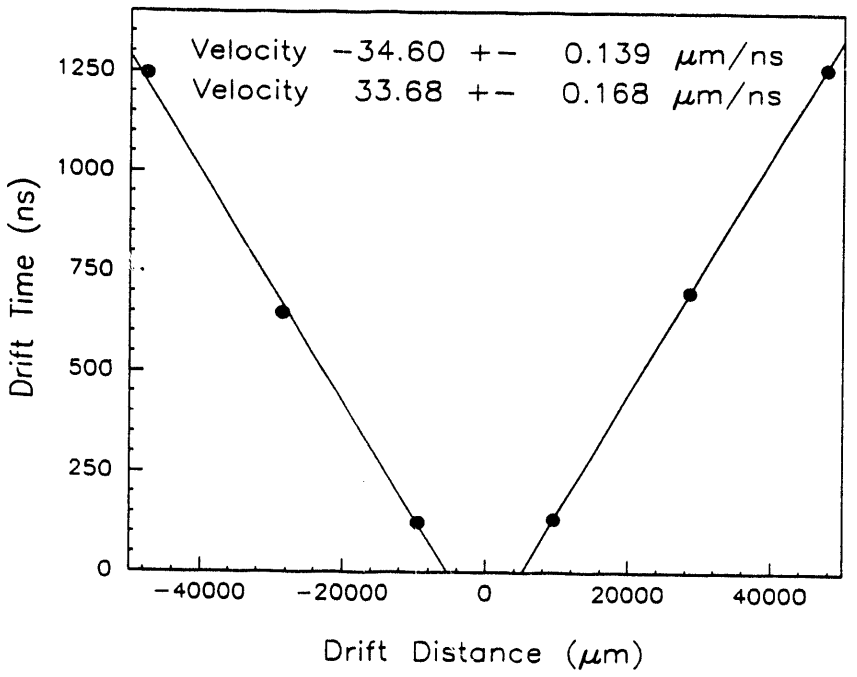

Figure 36. Drift velocity measured with the canary system.

histograms from the memory board over the local area network token ring system. The histograms are analyzed and measurements of drift velocity and gas gain are performed. The results are stored in a database with a time stamp.

3.3.4 Results

The drift time is calculated by requiring at least 6 of the 8 sense wires in the canary cell to have registered a hit. Any wires with multiple hits, most likely due to delta ray production, are rejected. A Gaussian fit of the drift time distribution for each of the six sources yields the average drift time. The position of the sources have been precisely measured a priori. The average drift time versus the source position is shown in Figure 36. The ordinate axis represents the sense wire plane and the

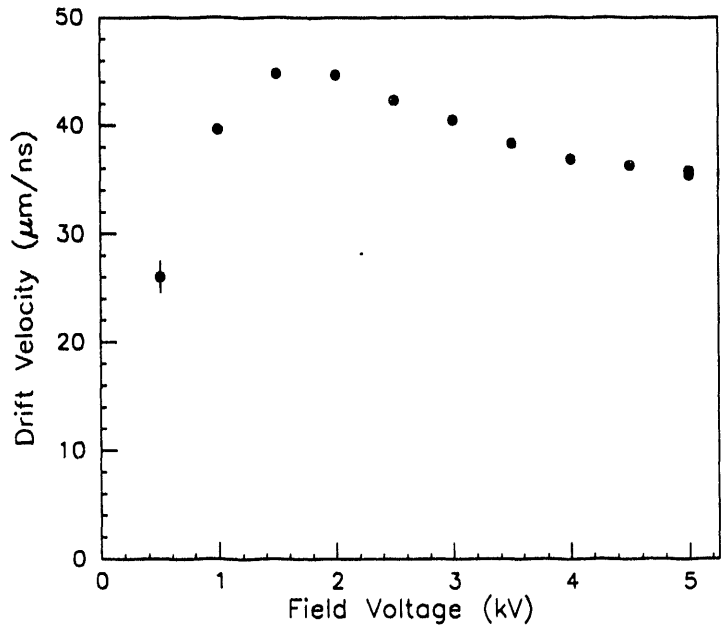

Figure 37. Dependence of drift velocity on electric field.

three points on each side of the axis represents the sources on each side the sense wire plane. A straight line fit yields two measurements of the drift velocity for each side of the sense wire plane.

The drift velocity has been measured as a function of the electric field with the canary and is illustrated in Figure 37. For large values of the field voltage, the drift velocity saturates and is not effected by small fluctuations in the electric field. This provides a linear space time correlation for the full width of the cell which improves the spatial resolution of the detector. The FDC theta chambers are operated with a field voltage of 5 kV.

Chapter 4
Energy loss in FDC

A charged particle traversing a gaseous medium interacts electromagnetically with atomic electrons of gas molecules constituting the medium. The resulting excitation and ionization of the atoms produces electrons and positive ions. The primary electrons produced drift towards the sense wire at positive high voltage in a uniform electric field. In the process they collide with other gas molecules creating secondary electrons. Both primary and secondary electrons give rise to an avalanche multiplication close to the sense wires. The resulting charge deposited is related to the momentum of the charged particle.

The energy loss of a charged particle traversing the medium can be described by the Bethe-Bloch [58] formula as

$$< \frac{dE}{dx} > \approx \frac{4\pi r^2 mc^2 N e^2}{\beta^2}\left(\frac{Z}{A}\right)\left[ln\left(\frac{2mc^2\beta^2}{(1-\beta^2)I}\right) - \beta^2\right] \qquad (4.1)$$

where

x = thickness of material

N = Avogadro number

m = mass of the electron

β = velocity of the charged particle

Z,A,I are the atomic number, atomic mass and mean ionization

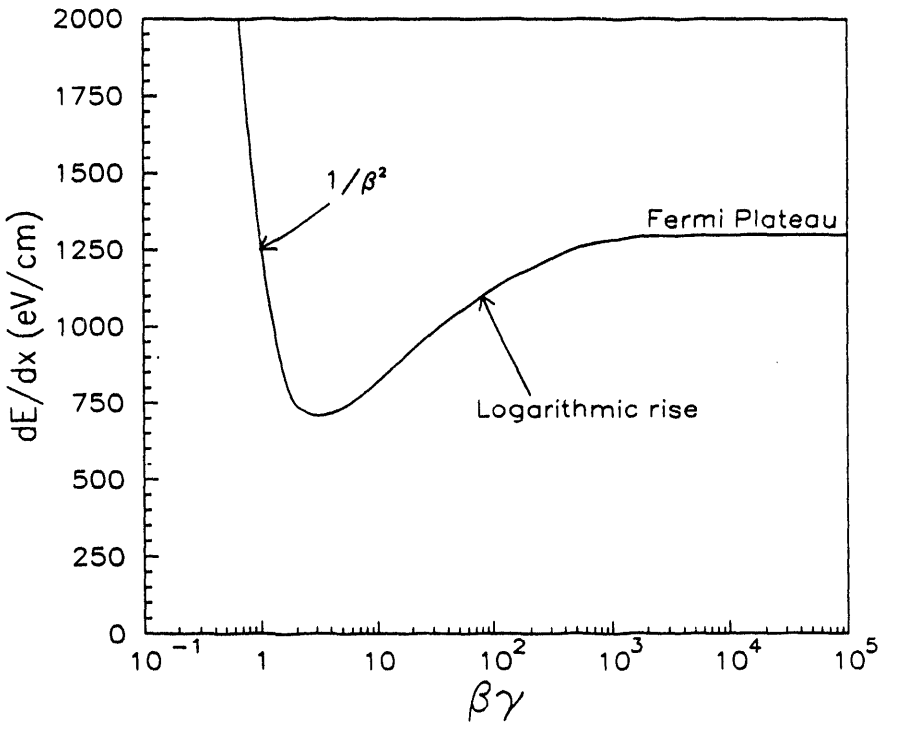

Figure 38. Dependence of energy lost by a charged particle on $\beta\gamma$.

potential of the medium.

It follows from the above equation that at low values of $\beta\gamma$, the energy loss is characterized by a $1/\beta^2$ dependence with a minimum at $\beta\gamma \approx 4$. The energy loss then rises logarithmically until the Fermi plateau is reached as shown in Figure 38. The magnitude of the relativistic rise depends on the atomic structure and density of the medium through which the particle is traversing.

Since DØ has no central magnetic field and a photon converting to an e^+e^- pair overlap in space, dE/dx is primarily used to distinguish between singly and doubly ionizing particles. A measurement of the total charge deposited can be used

to identify photons converting before the tracking chambers.

In this chapter, we shall derive the most probable energy loss using the photo absorption model [59] and compare it to data taken with a test beam. Various characteristics of pulse height, including efficiencies of separating singly ionizing against doubly ionizing tracks, will be discussed.

4.1 Energy loss cross section

The energy loss differential cross section for a charged particle passing through a medium is expressed as

$$\left(\frac{d\sigma}{dE}\right) = \left(\frac{d\sigma}{dE}\right)_{cer} + \left(\frac{d\sigma}{dE}\right)_{ion} + \left(\frac{d\sigma}{dE}\right)_{exc} \tag{4.2}$$

The first term is due to emission of Čerenkov radiation which is negligible for our purposes and will therefore be ignored.

The second term is the ionization term and is dominant when energy transferred is large compared to the atomic binding energy. In such cases, the atomic electrons as seen by the charged particle are virtually free and can be represented in terms of the Rutherford scattering cross section as

$$\left(\frac{d\sigma}{dE}\right)_{ion} = \frac{2\pi e^4}{mc^2}\frac{(1-\beta^2/E_{max})}{\beta^2 E^2}\int_0^E f(E')dE' \tag{4.3}$$

where $f(E)$ is the oscillator strength density and is proportional to the photo absorption cross section. E_{max} is the maximum possible energy that can be transferred.

The third term in equation 4.2 is the excitation cross section term and is dominant where energy transferred is comparable with the binding energy. In the model presented by Landau, he assumes that the energy transferred is very large compared to the binding energy of the atomic electrons. The Landau model was therefore described by the Rutherford term in the cross section and described the behaviour in the region of binding energies with a mean ionization potential. Since at relativistic energies, most of the energy transferred is peaked around the binding energy of various atomic levels, Landau's model incorrectly explained the behaviour at the relativistic limits. The photo absorption ionization model [PAI] takes into account the various atomic levels of the medium and agrees well with experimental observation. The primary decay modes in Argon due to excitation is described in the appendix. The excitation term can be expressed as

$$\left(\frac{d\sigma}{dE}\right)_{exc} = \frac{2\pi e^4}{mc^2}\frac{f(E)}{\beta^2 E}\left[ln\left(\frac{2mc^2\beta^2\gamma^2}{E}\right) - \beta^2\right] \tag{4.4}$$

The above term does not include the density effects. This phenomena is due to large electric fields which can polarize the medium causing a dielectric screening. Hence an atomic electron sees a smaller electric field caused by the moving charged particle in the medium than in vacuum. The density effect is represented by

$$\left(\frac{d\sigma}{dE}\right)_{density} = \frac{2\pi e^4}{mc^2}\frac{f(E)}{\beta^2 E}\left[ln\left(\frac{1}{|1+\beta^2\gamma^2(1-\epsilon)|}\right) + \beta^2(1 - Re(\epsilon))\right]$$

$$+ \frac{2\pi e^4}{mc^2}\frac{1}{\beta^2}\frac{2}{(\hbar\omega_p)^2}\left(\beta^2 - \frac{Re(\epsilon)}{|\epsilon|^2}\right) \tag{4.5}$$

where ω_p is the plasma frequency and ϵ is the dielectric constant of the medium. The last term in the density effect correction is due to Čerenkov radiation and can

be ignored. Combining the density effect term into the excitation cross section term in equation 4.4, the cross section can be rewritten as

$$\left(\frac{d\sigma}{dE}\right)_{exc} = \frac{2\pi e^4}{mc^2}\frac{f(E)}{\beta^2 E}\left[ln\left(\frac{2mc^2\beta^2\gamma^2}{E|1+\beta^2\gamma^2(1-\epsilon(E))|}\right) - \beta^2 Re(\epsilon(E))\right] \quad (4.6)$$

4.2 Energy loss distribution

For Mark-II gas, the ionization and the excitation cross sections must be summed over each gas type and atomic level. From equations 4.3 and 4.6

$$\left(\frac{d\sigma}{dE}\right)_{ion} = \frac{2\pi e^4}{mc^2}\frac{1}{\beta^2 E^2}\sum_{i=gas}\sum_{j=level}\int_0^E W_{ij} f_{ij}(E')dE' \quad (4.7)$$

$$\left(\frac{d\sigma}{dE}\right)_{exc} = \frac{2\pi e^4}{mc^2}\sum_{i=gas}\sum_{j=level} W_{ij}\frac{f_{ij}(E)}{\beta^2 E}\left[ln\left(\frac{2mc^2\beta^2\gamma^2}{E|1+\beta^2\gamma^2(1-\epsilon)|}\right) - \beta^2 Re(\epsilon)\right] \quad (4.8)$$

where E_{max} has been assumed to be large in equation 4.7. The oscillator strength density $f_{ij}(E)$ has been parameterized using the method of Lapique and Piuz [60] as

$$f(E) = \sum_{i=gas}\sum_{j=level} W_{ij} f_{ij}(E)$$

where $f_{ij}(E)$ is defined to resemble the photo absorption cross section [59] as

$$f_{ij}(E) = \begin{cases} \frac{(s_{ij}-1)}{E_{ij}}\left(\frac{E}{E_{ij}}\right)^{-s_{ij}} & , E \geq E_{ij} \\ 0 & , E < E_{ij} \end{cases} \quad (4.9)$$

Table 13.–Ionization potentials of atomic levels in Ar and CH_4.

Shell	W_i	E_i (ev)	S_i	E_i' (ev)	E_i'' (ev)
Ar - K	0.111	3206	2.75	5677.17	5038
Ar - L	0.444	248	2.29	538.41	440.25
Ar - M	0.133	52	3.2	81.92	75.64
Ar - Outer	0.311	15.8	3.2	24.89	22.982
CH_4 - K	0.20	283	2.52	546.39	469.18
CH_4 - Outer	0.80	11.5	2.15	27.44	21.5

The mean number of collisions per unit length is given by

$$\left(\frac{dN}{dx}\right) = \int \rho \frac{d\sigma}{dE} dE$$

where ρ is the number of electrons per unit volume of the medium.

The number of collisions per unit length is obtained by integrating equations 4.7 and 4.8. The following approximations are made to simplify the calculations:

1) The energy dependence in the logarithm term is replaced with the mean ionization potential to a good approximation, where the mean ionization potential E' is given by [61]

$$lnE' = \int_0^\infty ln(E) f(E) dE$$

which after substituting for $f(E)$ from equation 4.9 yields

$$E_{ij}' = E_{ij} e^{\frac{1}{s_{ij}-1}}$$

2) With the assumption that $1 - Re(\epsilon) \gg Im(\epsilon)$, ϵ can be approximated as

$$(1-\epsilon) = \frac{\omega^2 P}{(E')^2} = \frac{\omega^2}{(E')^2}$$

where P is the pressure of gas = 1 atm, ω is the plasma frequency.

3) Since the dielectric constant is close to unity, $\beta^2 Re(\epsilon)$ is substituted with β^2.

With the above approximations, equations 4.7 and 4.8 an be trivially integrated to yield

$$\left(\frac{dN}{dx}\right)_{ion} = \frac{2\pi e^4}{mc^2}\frac{1}{\beta^2}\sum_{i=gas}\sum_{j=level}\rho_i\frac{W_{ij}}{E_{ij}}\frac{(s_{ij}-1)}{s_{ij}} \tag{4.10}$$

$$\left(\frac{dN}{dx}\right)_{exc} = \frac{2\pi e^4}{mc^2}\sum_{i=gas}\sum_{j=level}\frac{\rho_i}{\beta^2}\frac{W_{ij}}{E_{ij}}\left(\frac{s_{ij}-1}{s_{ij}}\right)\left[ln\left(\frac{2mc^2\beta^2\gamma^2}{E'_{ij}+\frac{\omega_i^2\beta^2\gamma^2}{E'_{ij}}}\right)-\beta^2\right] \tag{4.11}$$

An effective mean ionization potential E'' can be defined from the above equations.

$$E''_{ij} = E_{ij}\left(\frac{s_{ij}}{s_{ij}-1}\right) \tag{4.12}$$

The most probable energy loss for the Rutherford scattering term has been derived by Landau with corrections by later authors [62].

$$(\Delta_{mp})_{ion} = \sum_{i=gas}\sum_{j=level} W_{ij}\xi_{ij}\left(ln\frac{\xi_{ij}}{E''_{ij}}+0.198\right) \tag{4.13}$$

The most probable energy loss for the excitation term is given by

$$(\Delta_{mp})_{exc} = \sum_{i=gas}\sum_{j=level}\left[\left(\frac{dN}{dx}\right)_{ij}x-\frac{1}{2}\right]E''_{ij} \tag{4.14}$$

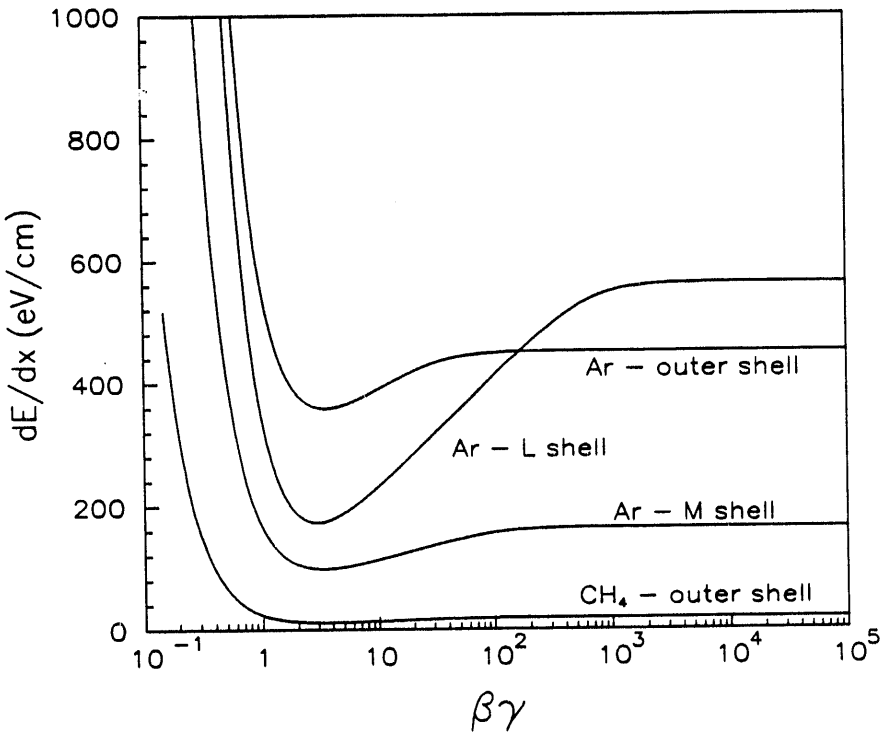

Figure 39. Energy loss dependence on $\beta\gamma$ for atomic shells.

where x is the sampling thickness. E''_{ij} is as defined in equation 4.12 and

$$\xi_{ij} = \frac{2\pi e^4}{mc^2}\frac{x}{\beta^2}\rho_i$$

The factor 1/2 in the most probable value of the excitation term is due to the Poisson nature of the distribution.

The coefficients s_{ij}, the weights w_{ij} and the ionization potential for each atomic shell are obtained from reference [61] and are listed in Table 13. In the calculation of the dE/dx spectra based upon the above discussed model, the effect of CO_2 has been neglected. At atmospheric pressure, the K-shell of argon and methane make

no contribution to the energy loss and have also been neglected. The density of gas (number of electrons per unit volume) used have been appropriately weighted according to the gas mixture to obtain $\rho_{Ar} = 3.55 \times 10^{20}\ cm^{-3}$ and $\rho_{CH_4} = 0.85 \times 10^{19}\ cm^{-3}$. Using equations 4.13 and 4.14, the most probable energy loss has been calculated for each atomic shell and is shown in Figure 39. The major contributions to the energy losses come from collisions with the outer most shell.

4.3 Monte Carlo simulation

The above equations 4.13 and 4.14 yields the most probable energy lost by a charged particle in an $Ar - CH_4 - CO_2$ gaseous mixture. However for a Monte Carlo simulation it is necessary to calculate the total number of electrons arriving at the sense wire and subsequently to digitize the charge collected. A procedure similar to the one described by Lapique and Piuz has been adopted for this Monte Carlo. The number of secondary electrons for each atomic shell are calculated according to the following steps.

- Using equations 4.10 and 4.11, the mean number of collisions per unit length is calculated for a given $\beta\gamma$ for each atomic shell.
- The number of collisions is obtained by generating a Poisson random number distributed about the mean number of collisions.
- It follows from equations 4.7 and 4.8, that the energy loss cross section is proportional to $E^{(-s-1)}$ for excitation collisions and E^{-2} for Rutherford type collisions. A random number is generated using this functional behaviour of the energy loss to give the amount of energy transferred for each collision.

Table 14.–Most probable decay modes in Argon and Methane.

E (eV)	Probability	# of e^-	Kinetic energy (eV)
Argon:			
15.8 - 248	1.0	1	K_1 = E - 15.8
248 - 280	1.0	2	K_1 = 200
			K_2 = E - 248
280 - 316	0.8	2	K_1 = 200
			K_2 = E - 248
	0.2	3	K_1 = 200
			K_2 = E - 265
			K_3 = E - 265 - K_2
326 - 3206	0.65	2	K_1 = 200
			K_2 = E - 248
	0.35		K_1 = 50
			K_2 = 200
			K_2 = E - 326
> 3206	0.88	3	K_1 = 200
			K_2 = 2670
			K_2 = E - 3206
	0.12	2	K_1 = 2870
			K_2 = E - 3206
Methane:			
11.5 - 283	1.0	1	K_1 = E - 11.5
> 283	1.0	2	K_1 = 243
			K_2 = E - 283

- The number of primary electrons produced and their kinetic energies can be deduced using the most probable decay modes of argon and methane given by Lapique and Piuz [60] [63]. Table 14 lists the kinetic energy of electrons produced as a function of the energy transferred in the collision (See Appendix-1).

- The mean number of secondary electrons produced is given by the equation $NS = \frac{K-K_0}{W}$ where K is the kinetic energy of the electron, K_0 is the ionization potential of the outer most shell of argon (15.8 eV) and W is the mean work required to produce an ion pair (26.4 eV for argon, 28 eV for methane).

- The mean number of secondary electrons obtained is distributed using the Fano factor [60]. A Gaussian random number is generated with a mean equal to NS and the standard deviation equal to $\sqrt{(F * NS)}$ where F is the Fano factor taken to be 0.18 to yield the number of secondary electrons.

The effect of diffusion by electrons and fluctuations in amplification near the sense wire plane have been ignored. This is justified based on the results shown in the previous chapter. The number of secondaries obtained from the above calculation is proportional to the amount of charge deposited on the sense wire.

Using further simulation [54], the charge is converted into a pulse shape and the digitized output is stored for each sense wire. Energy scans by generating events with electrons and pions at various energies have been simulated. Figure 40 shows the Monte Carlo prediction superimposed on the model. The ordinate axis is the relative ionization with the Fermi Plateau defined as equivalent to one minimum ionizing particle (1 MIP). Under the current the actual minimum (MIP) is redefined

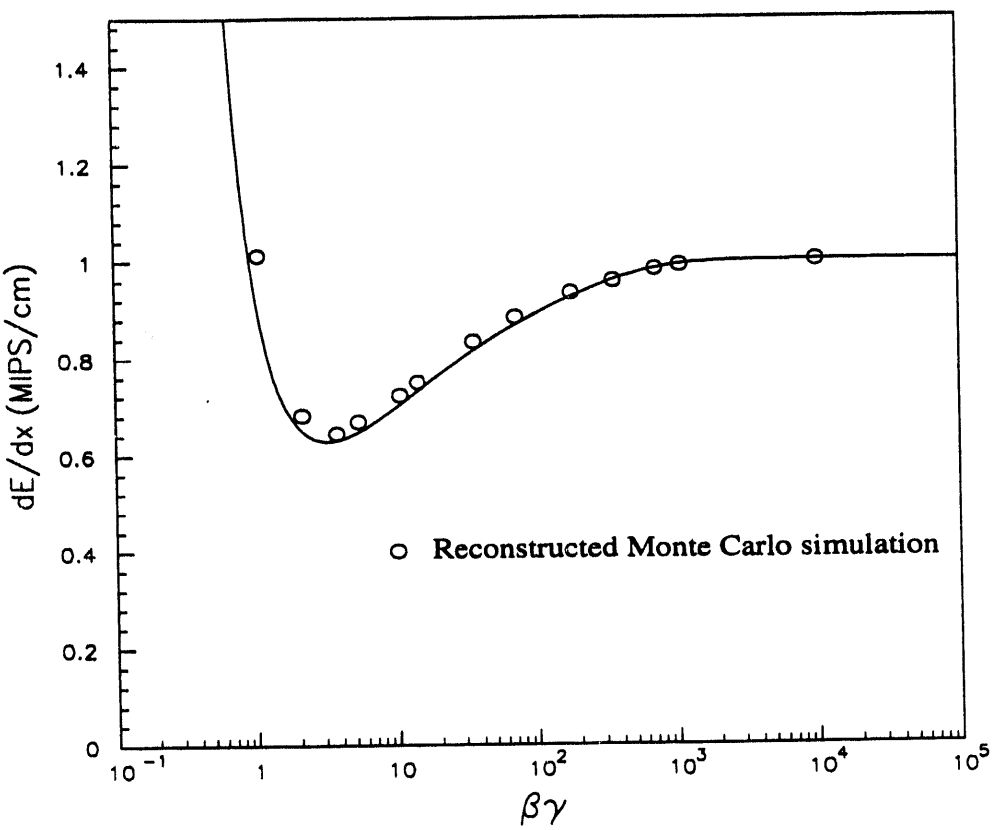

Figure 40. Monte Carlo simulation of dE/dx for DØ gas.

to occur at 0.625 MIP. The convention has been so adopted since the use of dE/dx in DØ is primarily to identify electrons (1 MIP) from gamma conversions (2 MIP). Henceforth the word MIP will be used for particles on the Fermi Plateau. The truncated pulse height distribution of simulated pion samples are normalized to the electron sample. The solid lines are the predictions using equations 4.13 and 4.14. The circles which are reconstructed predictions of the Monte Carlo are in good agreement to within a few percent.

4.4 Measurement of relativistic rise

The relativistic rise was measured with a low energy pion test beam at NWA with a Theta quadrant. Data for this study could not be done with the full forward drift chamber as it was being prepared for installation in the full DØ detector. The Theta quadrant placed in the beam line was built as a spare and is identical to the Theta quadrant in the FDC. However, the Theta quadrant provided only 8 measurement samples compared to 32 samples with the full FDC. The measurement resolution was poor since the dE/dx resolution depends strongly on the number of samples used.

The test beam line was modified to provide low energy beams between 1 and 10 GeV as explained in the previous chapter. Data samples were collected between 2.0 GeV and 10.0 GeV, each sample consisting of 5000 events at a given energy setting. The electron background in the pion beam was used to normalize the pion data sample. This technique reduced the systematic uncertainties such as fluctuations of pulse height with time and small changes in atmospheric pressure which were not monitored. Each sample of data was analyzed separately as follows:

- Using the Čerenkov information, electron and pion events were separated for a given sample.
- Punch through events, where the muon counter fired were rejected.
- Due to inefficiencies of the camac system, events where the ADC's failed to digitize were rejected.
- Track were reconstructed using the PWC's to provide a momentum measure-

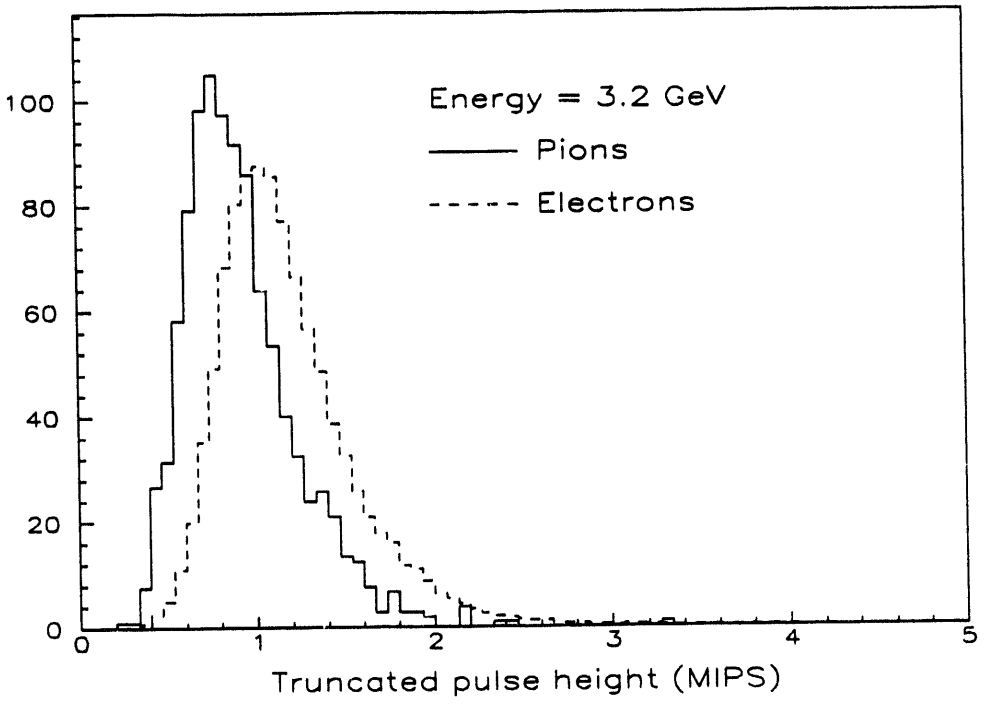

Figure 41. Electron and pion distribution at 3.2 GeV.

ment.

- Tracks were reconstructed in the theta chamber using eight sense wires and delay line information. Track reconstruction required at least six hits in the chamber.
- Events with multiple tracks in the chamber were rejected.
- Pulse height information for hits lying on a track were corrected for relative gains between channels using minimum ionizing tracks.
- Using hits on a given track, a truncated mean pulse height was calculated with the lowest 70% of the pulse height samples on a track.

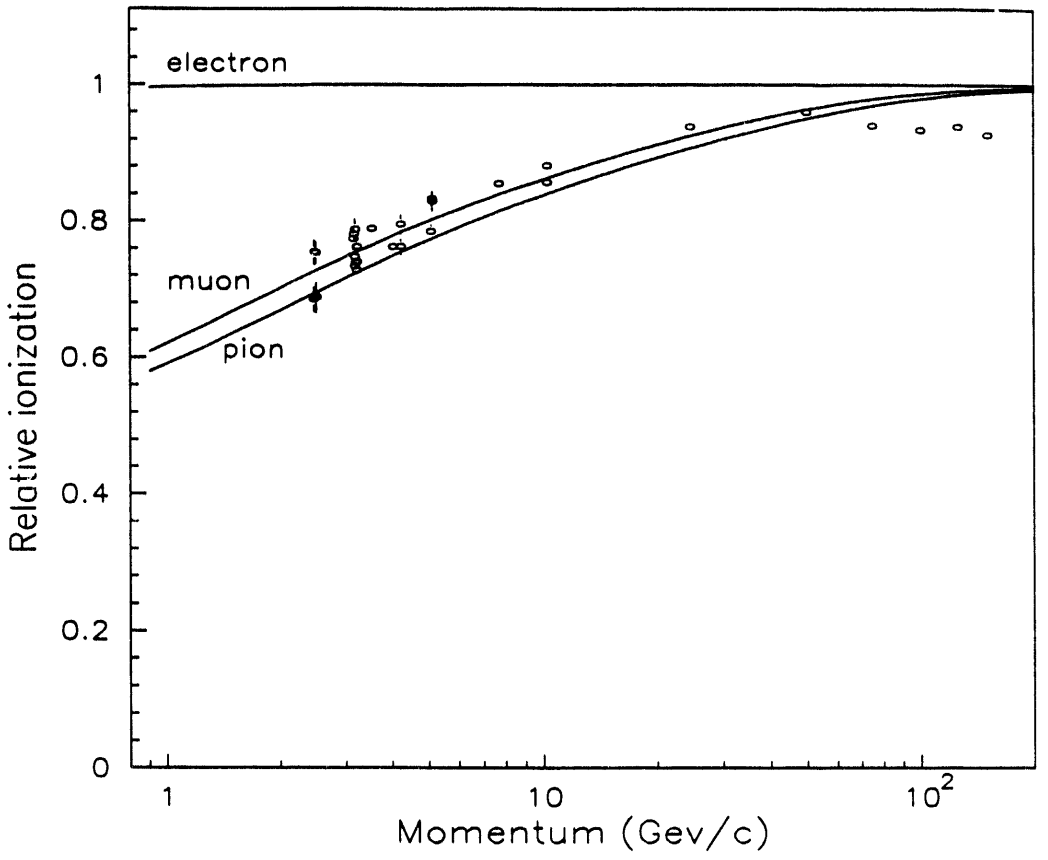

Figure 42. Measurement of relativistic rise with pions at test beam.

- The truncated pulse height distribution for the pion sample was normalized to the electron sample. A representative pulse height distribution of the electron and pion sample at 3.2 GeV is shown in Figure 41.

The results of all analyzed samples are shown in Figure 42. The data points are superimposed on the curves which are calculations of the most probable energy loss using the photo absorption model. Due to inefficiencies of the Čerenkov counters, pion and muon events could not be well separated. Thus the data is some mix of both pions and muons. The main sources of systematic errors are as follows:

1) Poor dE/dx resolution due to the limited number of pulse height samples along a track.

2) Inefficiencies of the Čerenkov counters having a direct effect on particle identification.

3) Changes in pulse height and drift velocities due to pressure fluctuations were assumed to be cancelled after normalizing pion samples to electrons.

4) PWC inefficiencies due to noisy or dead wires causing mismeasurement of track momentum.

Given the systematic uncertainties in the measurement, the data agrees well with the predictions at low energies. The two curves are shown for muons and pions which could not be separated experimentally. The spread in the data is consistent with the spread in the curves. The discrepancy seen at higher energies is thought to be due to the result of normalizing to the electron sample. Since the effect of bremsstrahlung of electrons is more probable at high energies, the result would lead to an overestimate of the most probable value of the pulse height for the electron sample. Normalizing the pion sample to the electron sample would then yield a smaller ratio than what has been predicted. The observations seem consistent with this explanation.

4.5 Simulation of 2-MIP events

A standard approach to evaluate 2-MIP event rejection against 1-MIP event acceptance efficiency is to simulate 2-MIP events using 1-MIP tracks from real data. The simulation takes advantage of the FADC cluster distribution. The data used for the simulation was taken with 50 GeV pions at NWA. Single track events were selected and two adjacent events were superimposed on each other. Each track was required to have a track segment in all three layers of the chamber. The cluster time on a given sense wire in each of the three layers for both events was determined. Using the difference in the cluster time position for a single sense wire, all sense wire clusters in the second event were moved in time to force it to occur at the same time as the first event.

The two events were superimposed by adding the FADC data for all sense wires. Tracks were again reconstructed using the simulated data sample and the truncated mean pulse heights were calculated for each event. Figure 43 shows the pulse height distribution for 1 and 2-MIP events at 70% truncation. A 2-MIP event is identified by requiring the reconstructed track to have a pulse height greater than a critical pulse height PH_c. The 1-MIP efficiency is defined as the fraction of 1-MIP events having a pulse height smaller the PH_c. The 2-MIP rejection is defined as

$$(2-\mathrm{MIP})_{\mathrm{rej}} = \frac{\#\text{ of events with Pulse Height} > PH_c}{\#\text{ of events with Pulse Height} \leq PH_c}$$

Qualitatively, it reflects the number of 2-MIP candidates successfully identified for each misidentified event. For the simulated data, the 2-MIP rejection factor was determined by using the PH_c which gives 90% 1-MIP efficiency. Figure 44 shows

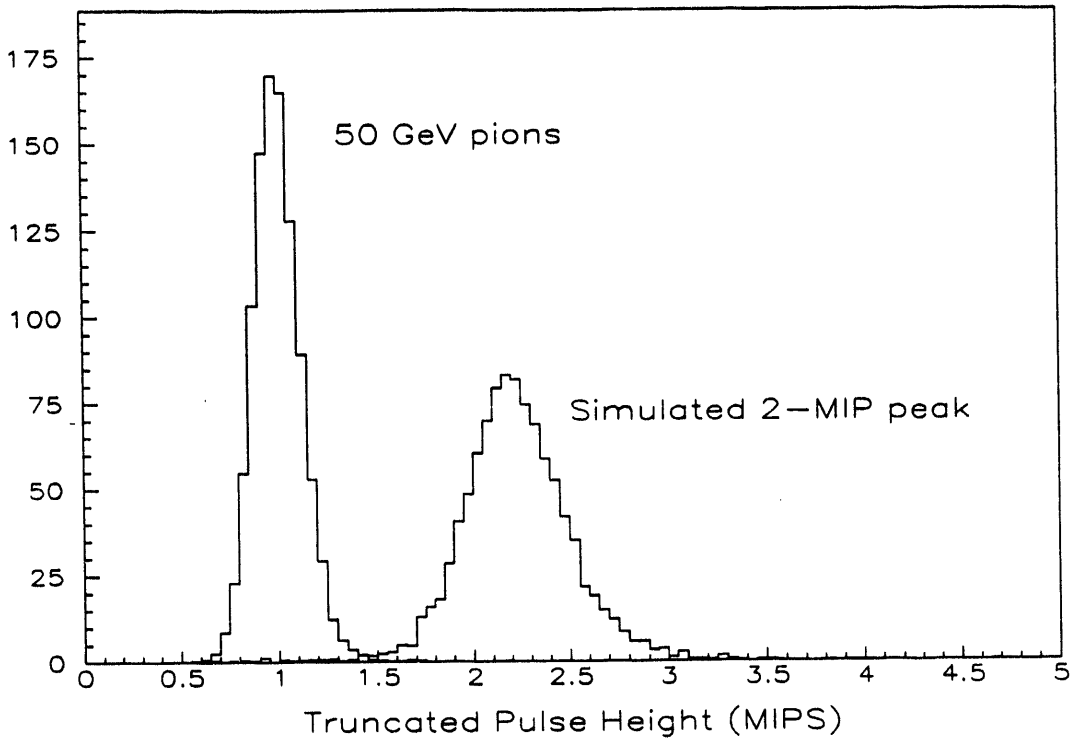

Figure 43. Simulation of 2-MIP events by overlapping 1-MIP tracks.

the rejection factor as a function of the fraction of samples retained in a given track for measurement of the effective track pulse height. The 2-MIP rejection rapidly increases with larger number of samples since the dE/dx resolution improves with the number of samples. As more samples are kept, the effect of Landau tail increases the relative overlap between 1-MIP and 2-MIP distributions resulting in lower 2-MIP rejection factor.

The number of events lying in the tail of the distribution is computed by counting the number of events beyond 10% times the peak pulse height value for each distribution. This is demonstrated in Figure 45 for both electrons and pions where the fraction of the number of events in the tail is plotted against the fraction of

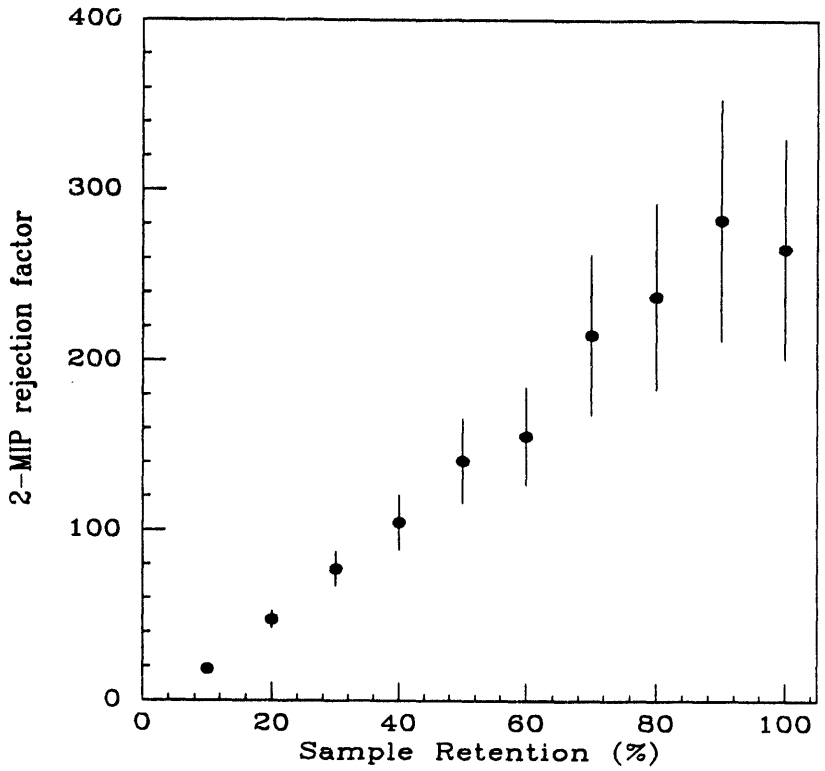

Figure 44. 2-MIP rejection factor as a function of samples retained.

samples retained for a given track. The fraction of the events in the tail region grows more rapidly for electrons than for pions due to the effect of bremsstrahlung which dominates over the Landau effect. For the pion sample, the Landau effect dominates and only a slight increase is observed when more than 75% of the samples are retained. The operating truncation factor for data analysis has been chosen to be 75% to curtail the effect of the tail when larger number of samples are retained.

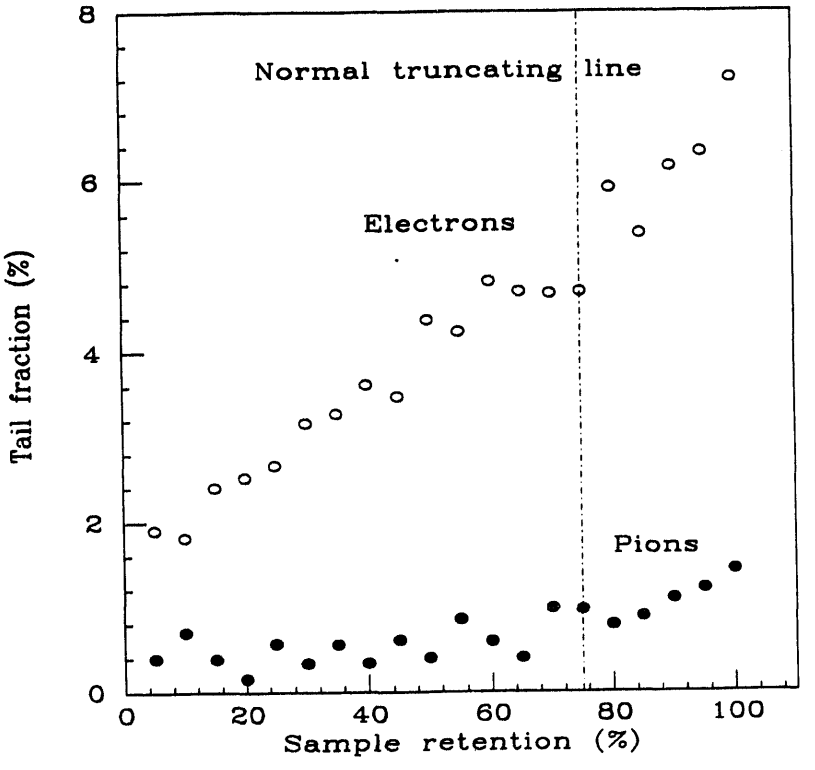

Figure 45. Pulse height distribution asymmetry as a function of samples retained.

4.6 Conversions with test beam

A photon beam was generated at the test beam as explained in section 3.2.1. Figure 46 shows a detailed layout of the relevant portions of beam line used for generating a photon beam and the experimental apparatus used to observe photon conversions to e^+e^- pairs. The pairs were produced by having an electron beam incident on target T1 and subsequently converting the radiated photon using target T2. The trigger required a veto of the counters upstream of the converting target T2 and a coincidence of the counters downstream of the target as shown in the figure. The targets T1 and T2 were 3" × 3" × 0.061" lead targets equivalent to 28%

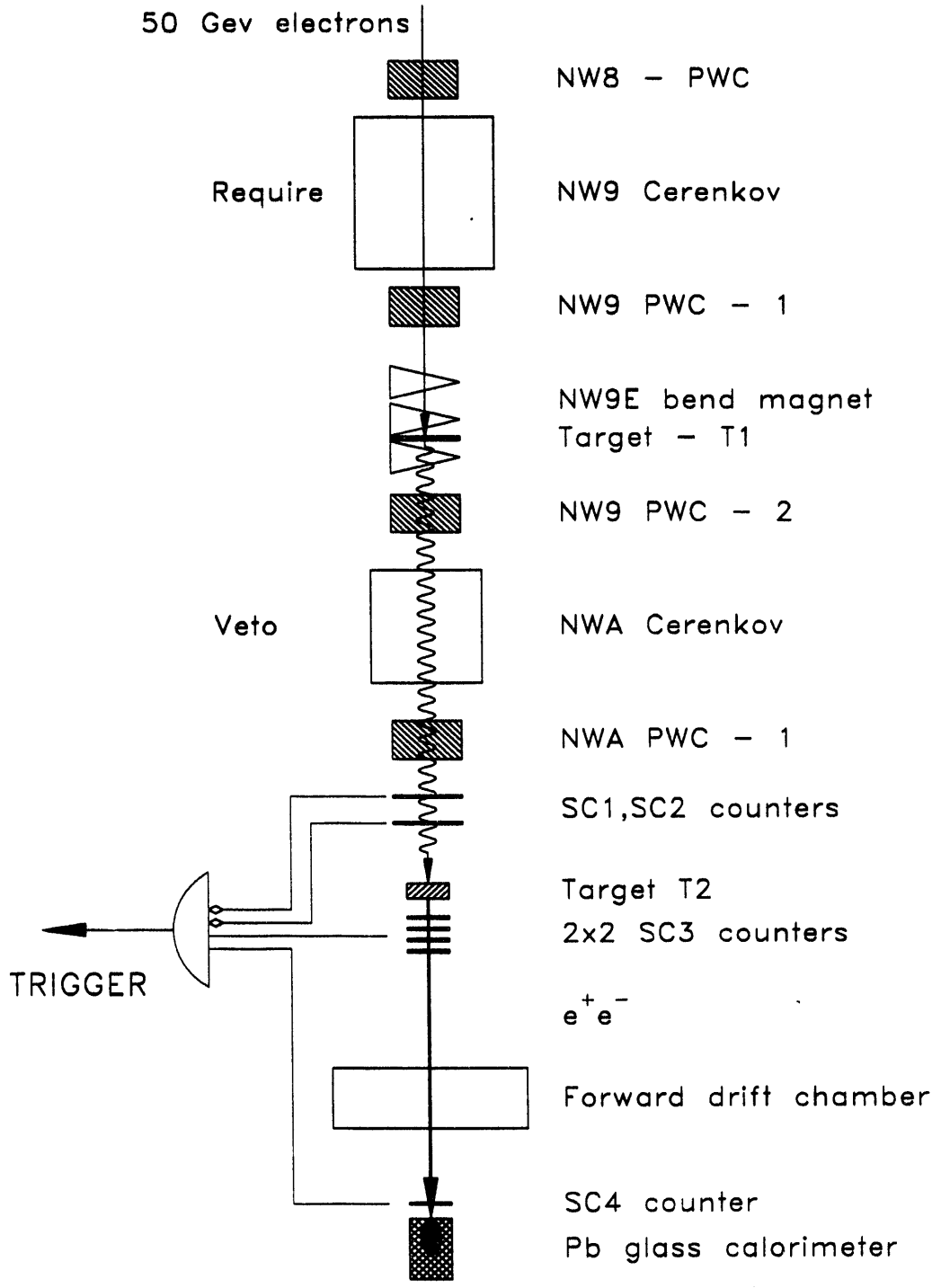

Figure 46. Experimental layout and trigger setup for conversion studies.

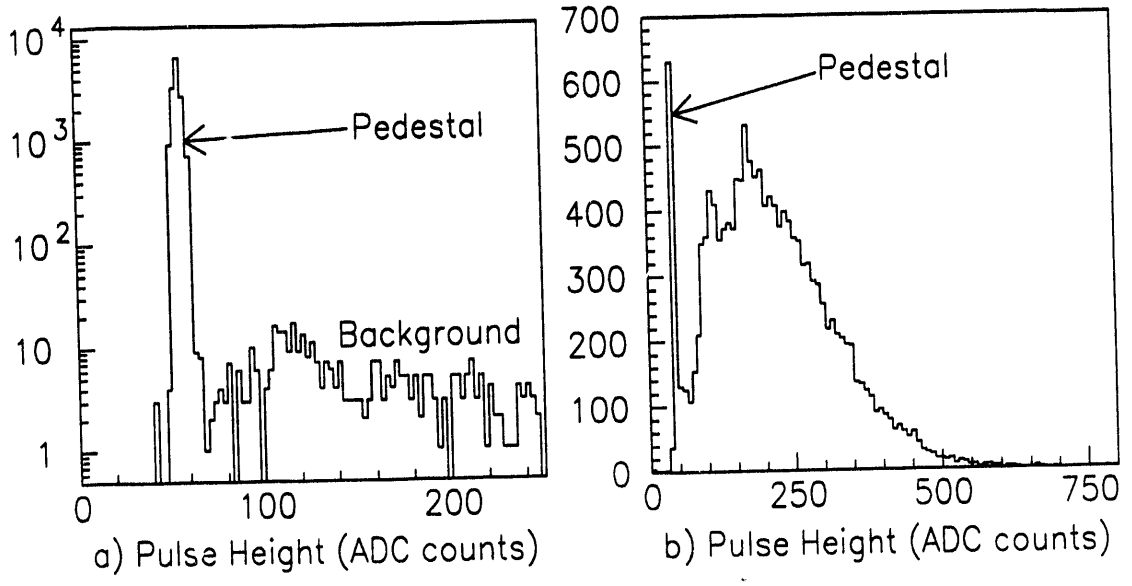

Figure 47. Čerenkov Pulse Height distribution a) Downstream (NWACC), b) Upstream (NW9CC) of the conversion target T1.

radiation length of material.

The Čerenkov counters NWACC and NW9CC were read out using a camac based system. The pressure in the NW9CC Čerenkov was set just above the pion threshold. This provided a positive identification of electrons incident on the primary target T1. The NWACC Čerenkov located downstream of T1, was set to a very high pressure to tag any charged particles which would contribute to the backgrounds. Figure 47 shows the pulse height distribution of both the Čerenkov counters. The peak at the pedestal value for the NWACC counter indicates the absence of charged particles. Events where the pulse height count in the NWACC Čerenkov counter exceeded the pedestal value were rejected. The pulse height distribution seen in the NW9CC Čerenkov counter is as expected for electrons. Events where the upstream Čerenkov had a pulse height count less than or equal to the pedestal value were

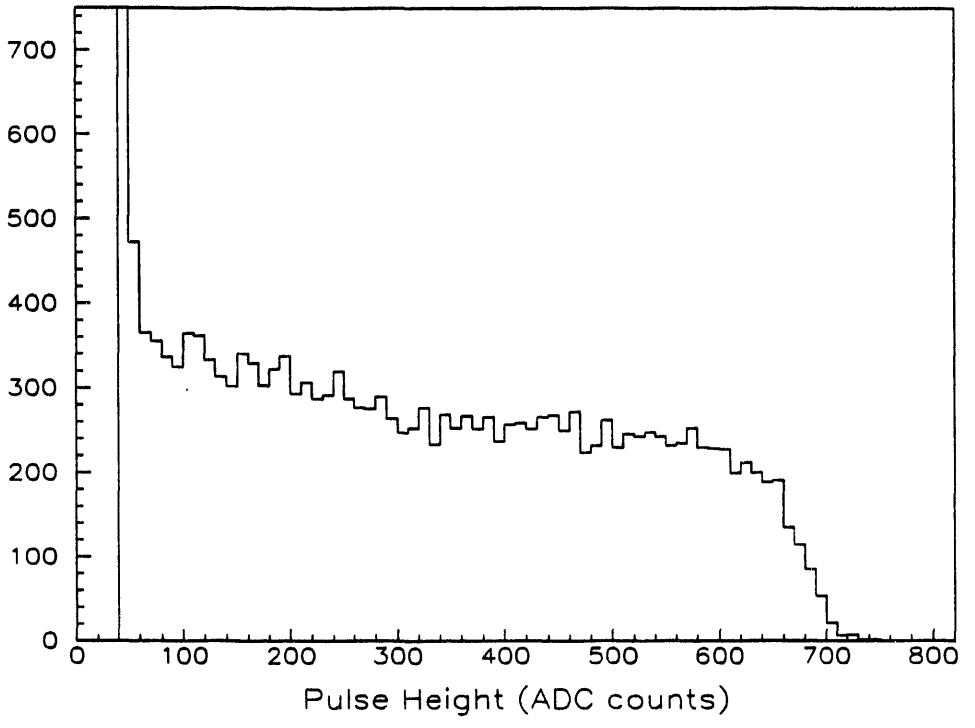

Figure 48. Gamma pulse height spectrum observed with the Lead glass.

rejected.

A lead glass calorimeter located downstream of the chamber was used to obtain the photon spectrum. Like the Čerenkov counters, the lead glass was digitized with a 10-bit LeCroy ADC and read out through the camac system. The lead glass was calibrated with electrons at various energies. A linear relationship was observed between the registered pulse height count and the electron energy up to 75 GeV. Above this the electromagnetic shower was no longer contained within the lead glass. The pulse height spectrum in the lead glass obtained with a photon beam is shown in Figure 48. A minimum energy of 2 GeV was required to be deposited in the lead glass calorimeter (see explanation below).

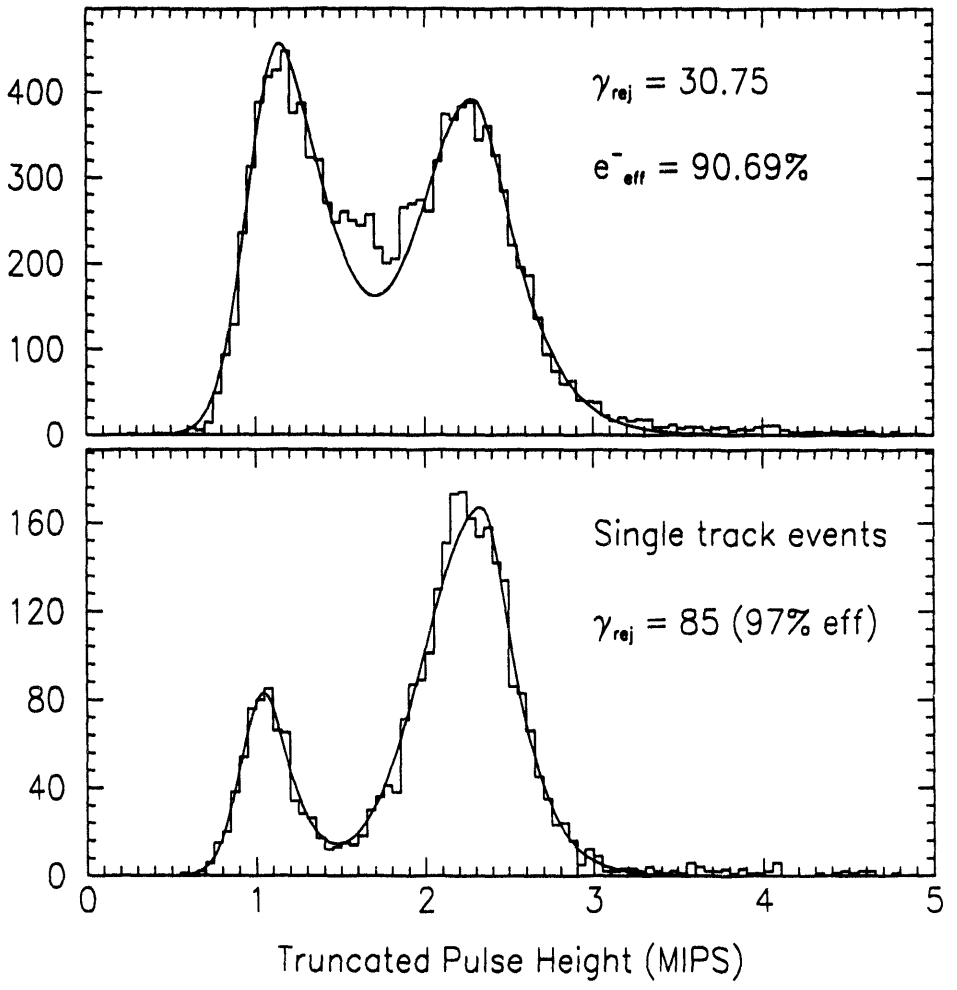

Figure 49. Pulse Height distribution with conversions at testbeam. The rejection factor improves for isolated tracks where the cell multiplicity is one (bottom figure) realtive to higher multiplicity events (top figure).

The dE/dx spectra shown in Figure 49 is obtained using the following steps.

- A similar analysis procedure as previously explained in section 3.6 was used to determine the pulse height along a track. 70% of the pulse height samples along the track were retained for dE/dx measurement.

- Events where the NWACC Čerenkov fired or the NWA9CC Čerenkov did not

fire were rejected.

- Events with less than 2 GeV energy deposited in the lead glass were rejected.
- Reconstructed tracks were extrapolated and were required to originate from within the boundaries defined by the target.

The two distributions shown in Figure 49 are with (top figure) and without (bottom figure) the multiplicity requirement in the chamber set to be one. A 2-MIP peak is clearly visible in both the distribution. The valley between the 1 and 2-MIP peaks is filled in less when the multiplicity is required to be one. The 1-MIP contribution arises from two separate processes. The first is the delta ray contribution which is associated with large energy transfers resulting in high energy recoil electrons. The effect of the delta ray production will in almost all cases result in more than a single track being seen through the chamber. The second major contribution to the 1-MIP peak comes from multiple scattering of pairs resulting from gamma conversions. This results in an observation of either one or two 1-MIP tracks being seen through the chamber. Since the multiple scattering strongly depends on the energy of the electrons resulting from gamma conversions, a minimum cut on the pulse height seen in the lead glass ensures fewer cases of multiple scattering. The effect of delta rays and multiple scattering is further reduced by requiring the presence of only one track through the chamber as depicted in Figure 49b.

The calculation for the 2-MIP rejection factor for a given 1-MIP efficiency is done by fitting each of the peaks to a separate function. With the knowledge of the functional behaviour of each of the peaks, the rejection factor is calculated. The rejection factor at 91% 1-MIP efficiency is 31 and improves significantly to 85 for

isolated tracks with a mulitiplicity equal to one.

Summarizing, the intrinsic resolution of the chamber to distinguish between 1-MIP and 2-MIP tracks as determined by the simulation technique is high. Background processes such as bremsstrahlung and multiple scattering, and high multiplicity events worsen the resolution. The same background processes are responsible for an electron to appear as a 2-MIP track as for a converted gamma to appear as a 1-MIP track in the chamber. Hence, to distinguish the contribution of these processes to the background, it was necessary to use a Monte Carlo simulation.

4.7 Capabilities of dE/dx at DØ

External physics effects contributing to the misidentification of 1-MIP and 2-MIP tracks have been studied in detail using a Monte Carlo. In this section, we shall discuss the main sources which contribute to the misidentification and evaluate the efficiency of dE/dx using the outer tracking chambers.

The offline analysis for electron identification uses the energy deposited in the electromagnetic calorimeter. If the energy deposited passes the threshold cuts, a road is formed using the eta and the phi position of the electromagnetic shower and the vertex position. The tracking chambers determine whether a track exists in the road provided. An electron is positively identified if a track is found in the supplied road and the energy lost by the particle satisfies with the definition of a 1-MIP candidate. The non existence of a track or the presence of a 2-MIP energy loss implies the presence of a γ or a π^0. The gamma conversion points in the central tracking chambers are shown as a scatter plot in Figure 50. The high density in the

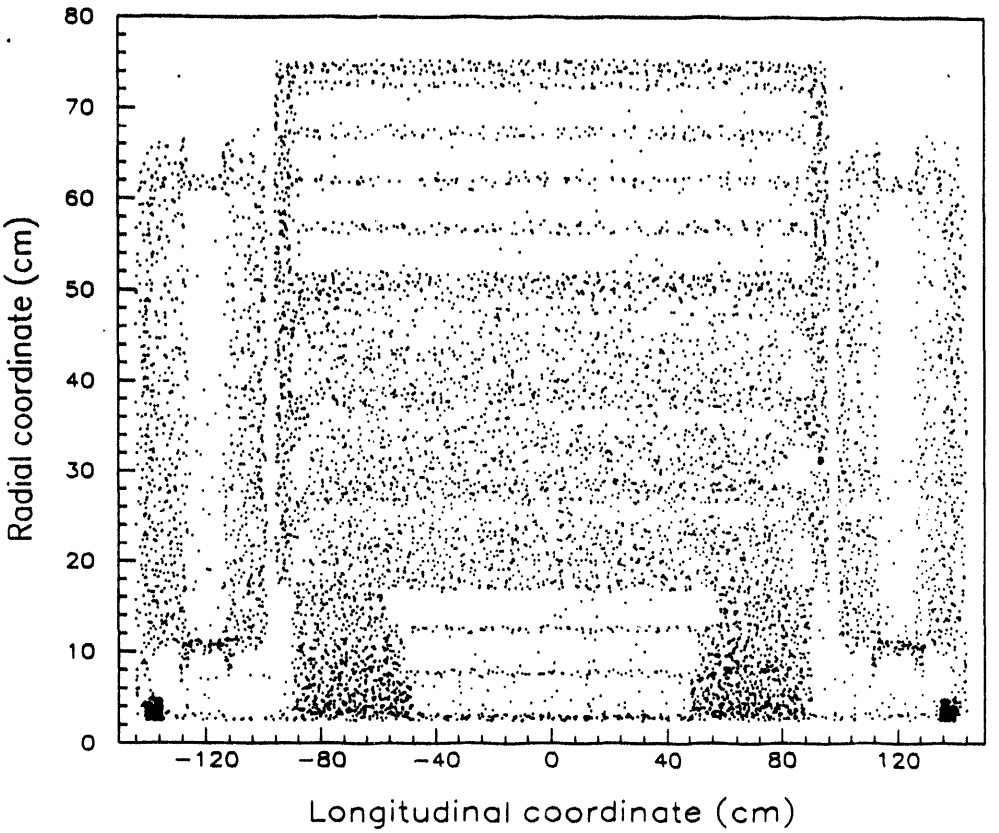

Figure 50. Points of gamma conversion in one half of the central detector obtained using a Monte Carlo simulation.

forward region is largely due to the preamplifier electronics and cables connected to the vertex chamber. The conversions in the central region primarily occur in the TRD radiator which comprises a total of 7% radiation lengths of material. Conversions at the walls of various chambers are also clearly seen.

The dE/dx Monte Carlo study described below does not take into account tracking inefficiencies or detailed analysis of shower profiles and efficiencies of the calorimeter. It also does not include information provided by the TRD and the vertex chamber which would improve the overall efficiency.

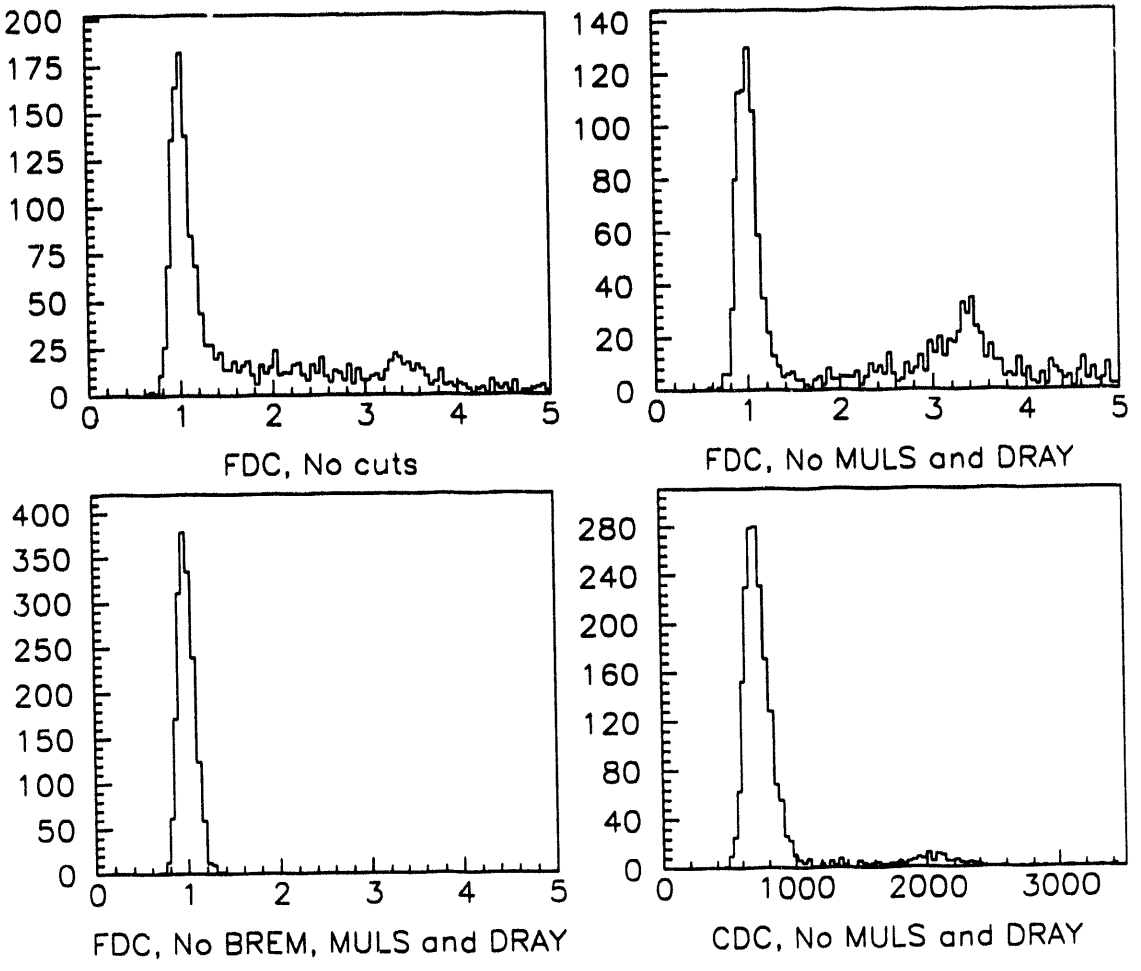

Figure 51. Effect of bremsstrahlung on electron pulse height distribution.

4.7.1 Electron identification

The DØ detector simulation in GEANT [64] has been described elsewhere [65]. The simulation includes all dead material contributions from cables and support structure that would be present in real time situation. ISAJET was used to generate single electrons originating from the vertex position and covering various detector eta slices at different electron energies. Simulated raw data was then generated by

running these electrons through the GEANT detector simulation which recorded the ionization losses in the chambers as digitized outputs. The dE/dx simulation used in GEANT was described in section 4.3. The simulated digitized outputs were subsequently analyzed by the same reconstruction programs as those used to analyze real data.

The misidentification of an electron as a gamma conversion occurs when the electron undergoes bremsstrahlung and the radiated photon converts in the material in front of the tracking chamber. At high energies, the produced pair overlap in space with the primary electron. The energy loss measured in the tracking chamber is therefore equivalent to a 3-MIP particle. Second order effects such as delta ray production and multiple scattering of the produced pair further smear the result. Figure 51 demonstrates the effect of the processes on the pulse height distribution and hence on the identification of 50 GeV electrons in the forward region. The first figure shows the raw truncated pulse height distribution in the FDC. The effect of turning off multiple scattering (MULS) and delta ray production (DRAY) is to reduce multiple tracks and second order effects which in turn reduces the 1-MIP contribution. This enhances the 3-MIP peak due to bremsstrahlung alone. Without any bremsstrahlung (BREM), the tail vanishes giving rise to a clear 1-MIP peak. The probability of an electron to radiate a photon and for the photon to subsequently convert largely depends on the amount of material which the primary electron traverses through and the energy of the electron. Thus the effect of bremsstrahlung is much reduced in the central direction as seen in the pulse height spectrum in the central drift chamber (CDC).

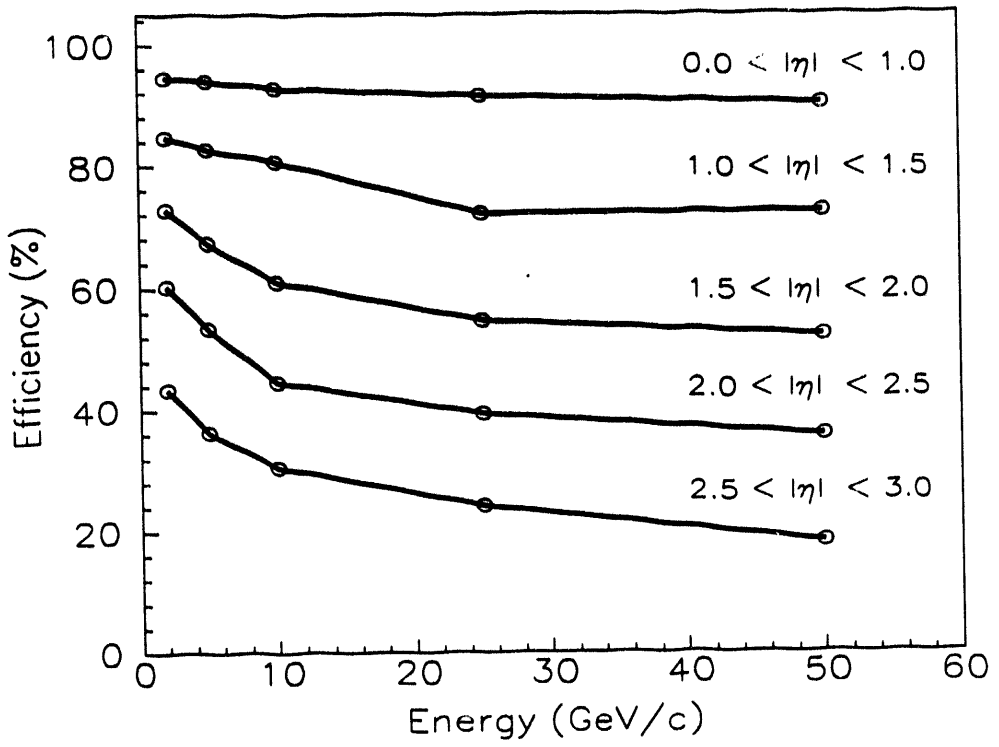

Figure 52. Electron identification efficiency using dE/dx in the outer tracking chambers as a function of the electron energy and the eta of the track.

The effect of bremsstrahlung on identification efficiency was studied by generating events at various eta slices between -3 and 3 at different electron energies. Figure 52 shows the probability that a given electron will be identified as a 1-MIP particle in the outer tracking chamber. The amount of material in front of the tracking system varies between 10% of a radiation length in the central direction to 40% in the extreme forward direction. The identification efficiency is therefore worse in the extreme forward regions since the radiation loss of an electron is proportional to E/X_0.

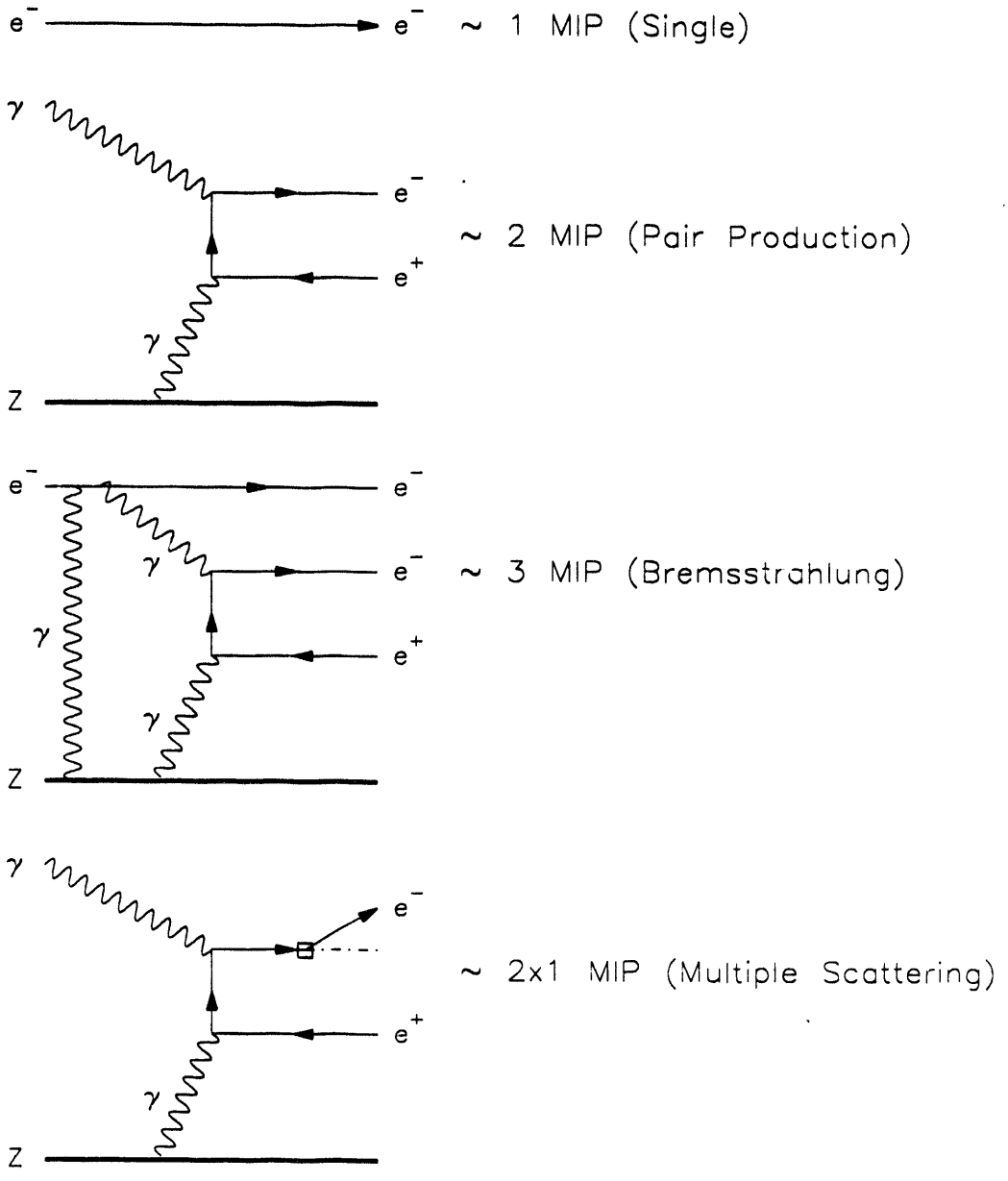

Figure 53. First order contributing processes and the equivalent energy loss measured in the tracking chambers. Second order effects, not shown in the figure, further smear the result.

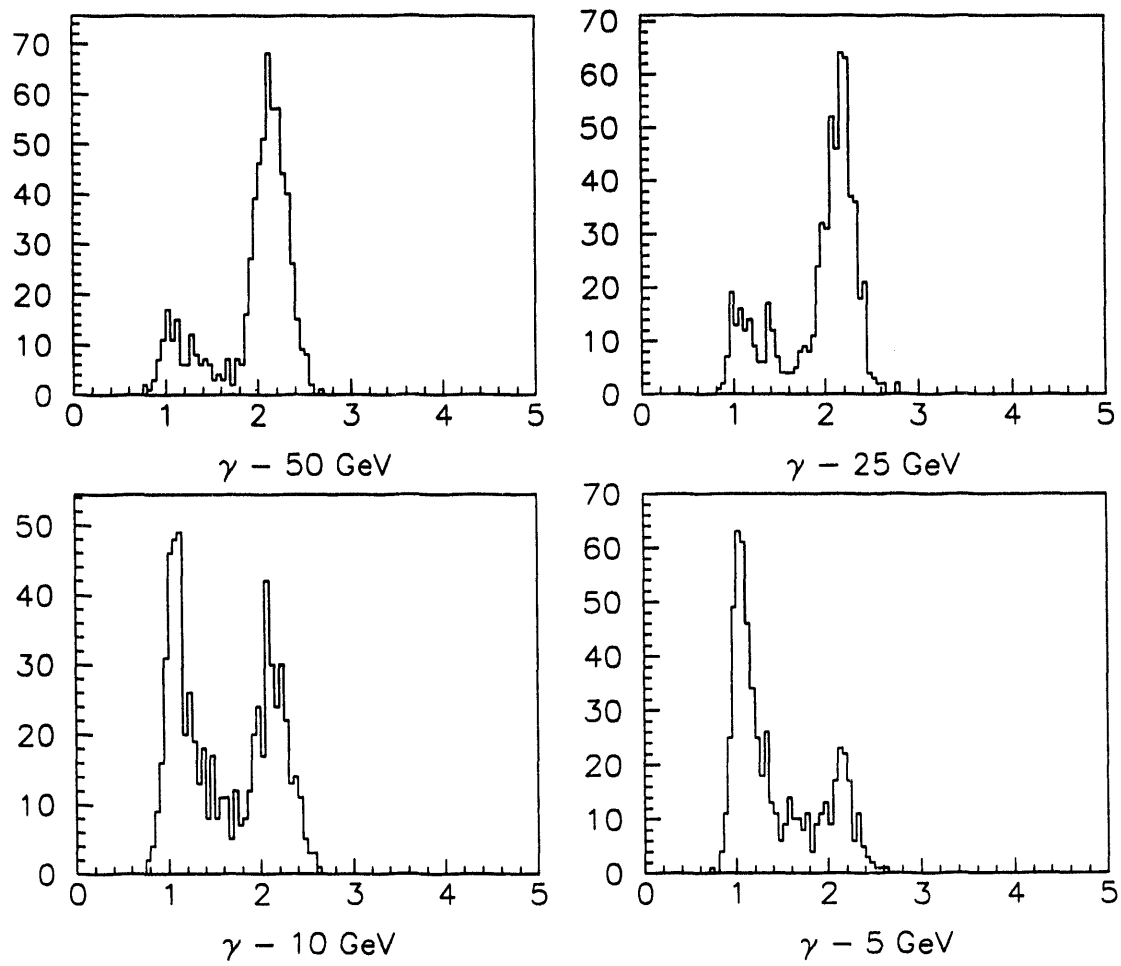

Figure 54. Effect of multiple scattering on pulse height distribution of e^+e^- pair resulting from gamma conversions in the forward region.

4.7.2 Gamma identification

Using a similar technique adopted for generating electrons, single gammas were generated at various detector eta slices with gamma energies between 2 GeV and 50 GeV. The fraction of gammas that convert before the outer tracking system depends on the eta of the track. Since there is no central magnetic field, the produced pair overlap in space for gamma energies in the GeV range. The energy loss

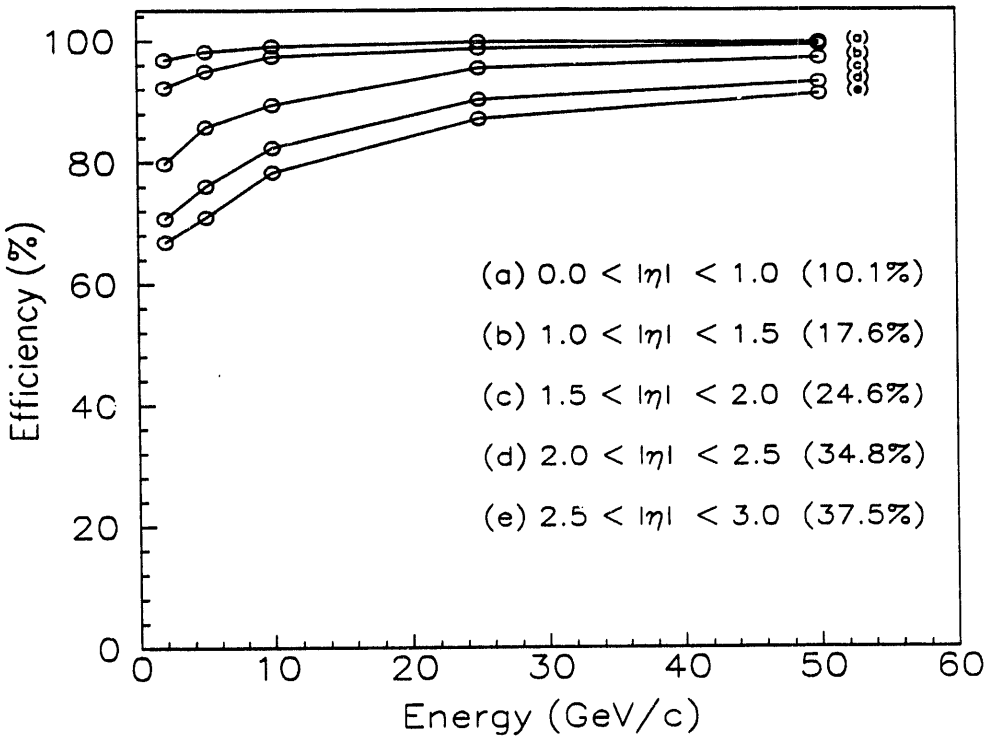

Figure 55. Gamma identification efficiency using dE/dx in the outer tracking chambers as a function of the electron energy and the eta of the track. The numbers in parenthesis show the fration of gammas which convert before the outer tracking chambers for the corresponding eta ranges.

measured in the tracking chamber for converted gammas correspond to a 2-MIP signal. Gammas can therefore be identified in the tracking chamber by an absence of a track or a presence of a 2-MIP track determined using dE/dx. The main reason for misidentification of a gamma as a 1-MIP track is due to multiple scattering of one or both members of the produced pair. Figure 53 shows the first order contributing processes for both electrons and gammas and the equivalent energy lost in the chambers.

The effect of multiple scattering is enhanced with lower gamma energy and with

an asymmetric energy distribution between the electron and positron. Second order effects such as delta ray production and radiation loss of the created pair further smear the results. Figure 54 shows the effect of multiple scattering of the produced pair for gamma energies of 5, 10, 25 and 50 GeV in the forward region. With lower gamma energies, the increase in multiple scattering causes the increase in the 1-MIP contribution. The number of gammas successfully identified by an absence of a track or a 2-MIP equivalent energy loss in the chamber is calculated as a function of the gamma energy at various eta ranges and is shown in Figure 55. The numbers in parenthesis indicates the fraction of the gammas which convert before the outer tracking for the corresponding eta ranges. The efficiency of positive identification of a gamma with energy above 20 GeV varies between 80% to 98%.

4.7.3 π^0 identification

Similar studies have been performed with the Monte Carlo on π^0 detection efficiency. Figure 56 shows the efficiency with which a π^0 can be identified successfully by requiring an absence of a track or the presence of at least one 2-MIP track in the outer tracking chambers as a function of the π^0 energy for various eta ranges. Since the π^0 decays into two gammas, the number in the parenthesis indicated the probability that at least one of the two gammas convert. The two track separation resolution of the chamber is better than the opening angle between the two gammas from a π^0 decay. Thus two 2-MIP track will be reconstructed for π^0 energies of up to 150 GeV if both the gammas convert. The efficiency is worse than what has been quoted for a single gamma due to the presence of two gammas from a π^0 decay. The asymmetric distribution of the primary π^0 energy between the two gammas can

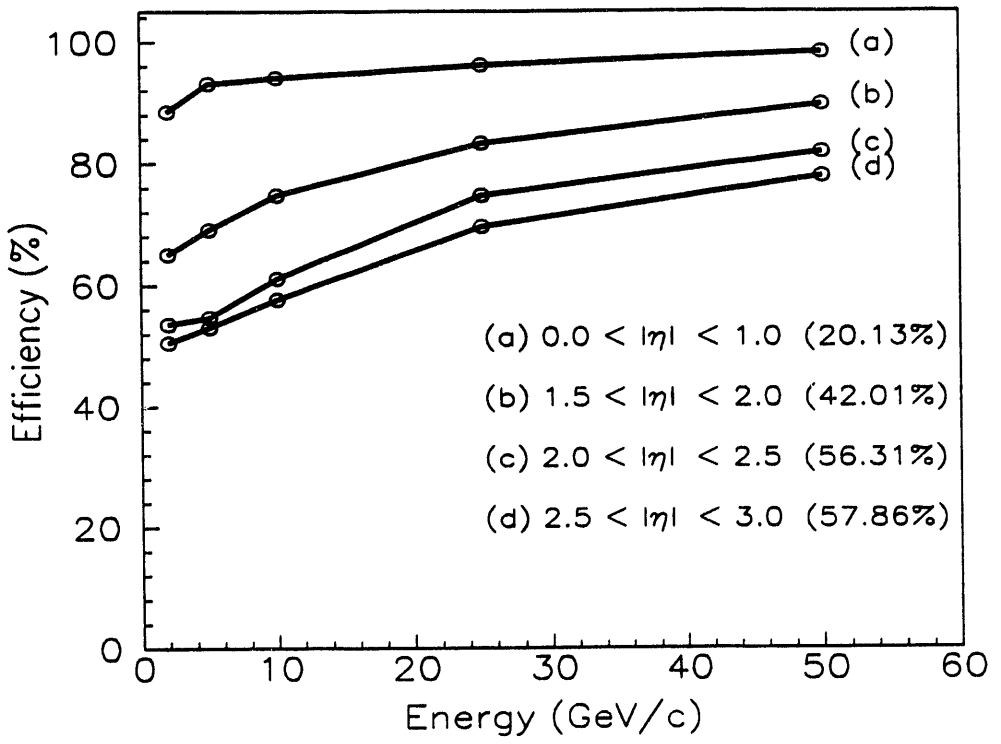

Figure 56. π^0 identification efficiency using dE/dx in the outer tracking chambers as a function of the electron energy and the eta of the track. The numbers in parenthesis show the fraction of events where at least one of the two gammas from a π^0 decay convert before the outer tracking chambers.

result in much lower gamma energies. The energy carried of by the produced pair is therefore much lower thereby increasing its probability to multiple scatter.

4.8 Backgrounds

The main backgrounds to electron identification in collider events come from isolated high P_T π^0 production which will fake an electron in the calorimeter. Figure 57 shows the charged particle P_T spectrum obtained on a sample of Monte Carlo events describing physics processes [66]. The gamma production overwhelms

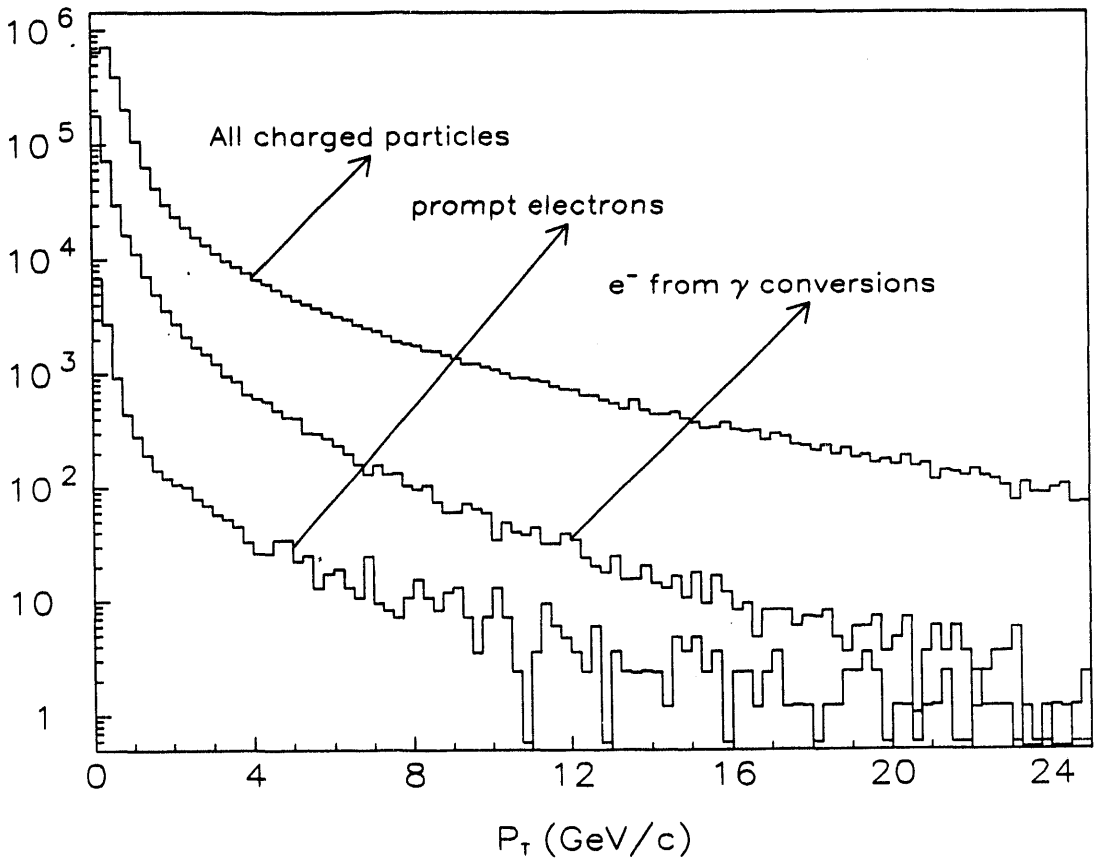

Figure 57. Monte Carlo simulation of the charged particle P_T spectrum.

the electron sample which dictates the requirement to have a good rejection against π^0 background. The figure however includes all gammas produced in an event including those within a jet. A study was performed [67] to calculate the isolated high P_T π^0 cross section on a sample of two jet final state QCD events. The study involved looking for a π^0 with P_T greater than 10 GeV outside a jet cone defined by $\Delta R = 0.4$. Figure 58 shows the isolated π^0 cross section as a function of the eta of the π^0 track. The cross section is high in the central region and is seen to fall rapidly in the forward direction due to the constraint on requiring a high P_T

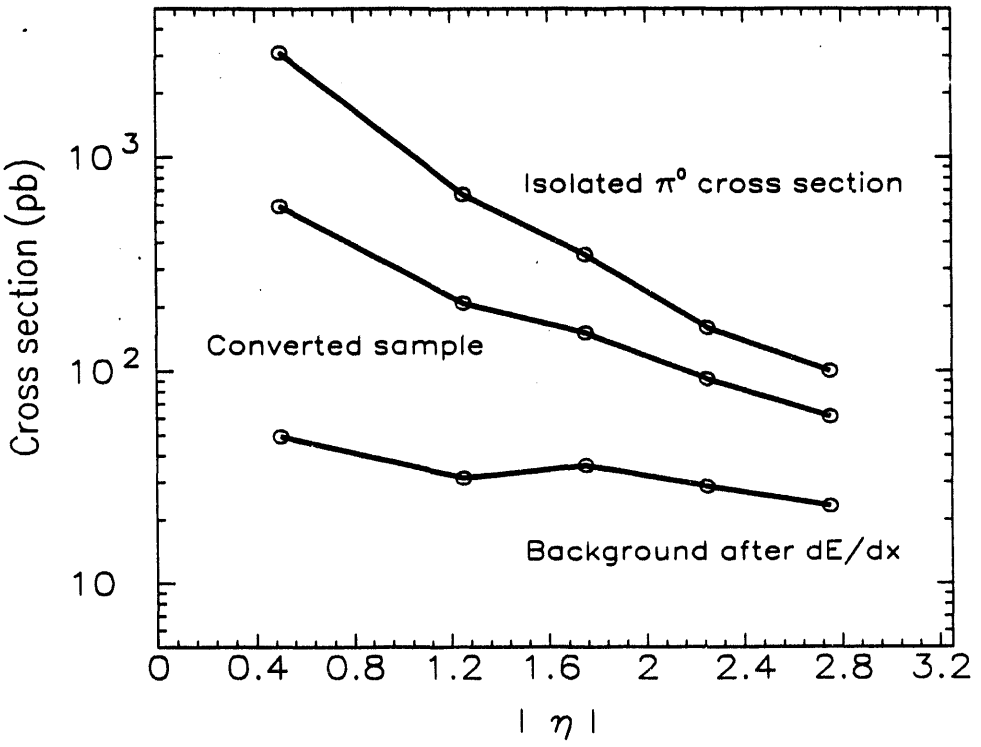

Figure 58. dE/dx rejection power on isolated π^0 production based on a sample of QCD two jet events with $E_T(\pi^0) > 10$ GeV and $\Delta R(jet) = 0.4$.

π^0. The cross section for the π^0 production where at least one of the two gammas resulting from its decay would have converted is also shown (Converted sample) in the figure. Using an average inefficiency of misidentifying a π^0 as an electron from the above described Monte Carlo study, the bottom curve reflects the background π^0 cross section after applying a dE/dx cut using the outer tracking chamber. The average background isolated π^0 with P_T greater than 10 GeV is 45 pb and is uniform over eta. The smaller π^0 cross section in the forward region compensates for the more inefficient detection of a π^0 relative to the central direction.

4.9 Conclusions

We have studied in detail the energy loss response of the forward tracking system using a test beam. The low energy response of the chamber is consistent with the predictions of the photoabsorption ionization model. A rejection factor of 30 of 2-MIP tracks is obtained with a 90% efficiency of identifying 1-MIP tracks based on observations with a photon beam and improves significantly at lower multiplicities. Using a dE/dx simulation based on the photoabsorption model, we have studied in detail the effects of various background processes contributing to misidentification of electrons and π^0 and the efficiency of detecting high P_T isolated π^0 at the collider.

Appendix A

Excitation processes in $Ar/CH_4/CO_2$ gas mixture.

The ground state configuration of the Argon atom with 18 electrons is described by the atomic configuration $1s^2, 2s^2, 2p^6, 3s^2, 3p^6$. The excitation of Argon atoms occurs with the absorption of a virtual photon due to an electromagnetic interaction with the traversing particle. The absorption of a photon with energy E_γ results in the emission of a photoelectron of energy $E_\gamma - E_j$ for $E_\gamma > E_j$ where j is the atomic shell. Table 14 lists the energy range of the absorbed photon and the number of primary electrons produced. The emission of a photoelectron results in an excited state of an Argon atom which may further eject more electrons through the Auger process, the Coster-Kronig transition or the Penning effect depending on the energy of the absorbed photon. This appendix describes the various scenarios and the number of primary electrons produced in each case.

For an absorption of a photon with energy less than the minimum binding energy of the Argon atom (15.8 eV), no primary electrons are produced.

An absorption of a photon with energy in the range ($E_{min} < E_\gamma < E_L = 248$ eV), where E_L is the minimum energy required to eject an electron from the L-shell, results in the emission of an electron from the outermost M-shell ($3s^2, 3p^6$).

$$Ar + \gamma \rightarrow Ar^+(3s^2, 3p^5) + e^-, \quad E(e^-) = E_\gamma - E_{min} \text{ eV}.$$

For an absorption of energy between 248 eV and 3206 eV, ($E_L < E_\gamma < E_K$), sufficient energy exists to eject a photoelectron from the L-shell. There are three possible decay modes corresponding to the three sub energy ranges between E_L and

E_K. We shall denote these by E_{L_1} and E_{L_2} such that $E_L < E_{L_1} < E_{L_2} < E_K$. As indicated in Table 14, $E_{L_1} = 280$ eV and $E_{L_2} = 316$ eV.

(1) An absorption of a photon with energy between E_L and E_{L_1} results in ejection of a photo electron from the 2p state. An ejection of an electron from the inner 2p shell is followed by an Auger transition, where an electron from a 3p shell drops to the vacant 2p shell with an emission of an Auger electron. The process can be described as

$$Ar + \gamma \rightarrow Ar^+(2p^5, 3p^6) + e^- \quad E(e^-) = E_\gamma - E_L$$

$$Ar^+(2p^5, 3p^6) \rightarrow Ar^{2+}(2p^6, 3p^4) + e^- \quad E(e^-) = 200 \text{ eV}$$

(2) An absorption of an electron greater than E_{L_1} but less than E_{L_2} leads to the possibility of emission of two photoelectrons, one from the L-shell, the other from the outer M-shell. The probability of this process occurring is 20%, the decay process for the remaining 80% of the time follows as indicated in step-1. The resulting excited state of Argon decays again with the emission of an Auger electron. The atomic configuration for this process can be described by

$Ar + \gamma \rightarrow Ar^{2+}(2p^5, 3p^5) + e^- + e^-$ where the two electrons have energies of $E_\gamma - E_L$ and $E_\gamma - E_M$ corresponding to the ejection from the L-shell and M-shell respectively.

$$Ar^{2+}(2p^5, 3p^5) \rightarrow Ar^{3+}(2p^6, 3p^3) + e^- \quad E(e^-) = 200 \text{ eV}.$$

(3) The energy E_{L_2} is equivalent to the energy required to eject an electron from the 2s state in Argon. The probability of such an ejection taking place is 35% provided $E_\gamma > E_{L_2}$, the decay process for the remaining 65% takes place

through the emission of an L-Auger electron as described in step-1. The configuration for this special case can be described by

$$Ar + \gamma \rightarrow Ar^{+}(2s^1, 2p^6, 3s^2, 3p^6) + e^- \quad E(e^-) = E_\gamma - E_{L_2}$$

The excited state of the Argon atom with a vacancy in the 2s shell decays to its ground state through two transitions.

$Ar^{+}(2s^1, 2p^6, 3s^2, 3p^6) \rightarrow Ar^{2+}(2s^2, 2p^5, 3s^2, 3p^6) + e^-$ which is called the Coster-Kronig transition with the energy of the electron emitted equal to 50 eV.

$Ar^{2+}(2s^2, 2p^5, 3s^2, 3p^6) \rightarrow Ar^{3+}(2s^2, 2p^6, 3s^2, 3p^4) + e^-$ which is the familiar Auger transition.

As in step-2 above, absorption of higher photon energies, may result in the ejection of an electron from the 2s state simultaneously accompanied by an ejection from an outer shell state. This has been ignored since the probability of such a transition is negligible.

An absorption of energy greater than $E_K = 3206$ eV will result in the emission of an electron from the 1s state with an energy equal to $E_\gamma - E_K$. This will in most cases be followed two Auger transitions resulting in an L-Auger electron and a K-Auger electron. The atomic transition states of these can be described similarly as for the L-shell transitions.

The excited states of Argon in cases of gas mixture can further decay by the process

$$Ar^* + X \rightarrow Ar + X^* + e^-$$

where X is another gas molecule in the gas mixture, and the * represents the excited state of the atom. The above process is known as the Penning effect. However this process is dominant when the first ionization potential of X is smaller than Argon. In the DØ gas mixture, the ionization potential of CH_4 is larger than Argon hence decay transition through this process is negligible.

References

1. M. D. Lemonick, "The Ultimate Quest." *Time magazine*, Reported by P. Elmer-DeWitt, J. M. Nash and C. Redman, (April 16, 1990), pp 50-56.

2. M. Gell-Mann, *Phys. Lett.* **8**, 214 (1964).

3. J. Ellis *et al.*, *Annual Review of Nuclear and Particle Science.* **32**, 443 (1982).

4. S. Weinberg, *Phys. Rev. Lett.* **19**, 1264 (1967).

5. G. Arnison *et al.* (UA1 Collaboration), *Phys. Lett.* **B122**, 103 (1983).

6. G. Arnison *et al.* (UA1 Collaboration), *Phys. Lett.* **B126**, 398 (1983).

7. W. Marciano and A. Sirlin, "Testing the Standard Model by Precise Determination of $W^{\pm}$ and Z Masses" *Phys. Rev.* **D29**, 945 (1984).

8. V. Barger *et al.*, "Radiative Corrections to W, Z Masses and Constraints on new Z Bosons." *Phys. Rev.* **D42**, 42 (1990).

9. J. Alitti *et al.* (UA2 Collaboration), "An Improved Determination of the Ratio of W and Z Masses at the CERN $p\bar{p}$ Collider." CERN-PPE/91-163, (1991).

10. J. Alitti *et al.* (UA2 Collaboration), "A Precise Determination of the W and Z Masses at the CERN $p\bar{p}$ Collider." *Phys. Lett.* **B241**, 150 (1990).

11. F. Abe *et al.* (CDF collaboration), "Measurement of the W-boson Mass in 1.8-TeV $p\bar{p}$ Collisions." *Phys. Rev.* **D43**, 2070 (1991).

12. M. Demarteau, (private communication).

13. P. Langacker and M. Muo, "Implications of Precision Electroweak Experiments for m_t, ρ_0, $\sin^2\theta_W$, and Grand Unification." *Phys. Rev.* **D44**, 817 (1991).

14. W. Hollik and G. Burgers, "Z^0 Physics at LEP1." **V1**, CERN 89.08 (1989).

15. F. Abe *et al.* (CDF Collaboration), "A Limit on the Top Quark from Proton-Antiproton Collisions at $\sqrt{s}$ = 1.8 TeV." FERMILAB-PUB-91-352-E, (1991).

16. D. Green and H. Lubatti *ed.*, "**Physics at Fermilab in the 1990's.**" Proceedings of the HEP Workshop, Breckenridge, Colorado, (World Scientific, New Jersey, 1989).

17. H. Baer *et al.*, "Detecting very Massive Top Quarks at the Fermilab Tevatron." *Phys. Rev.* **D43**, 54 (1990).

18. J. Cochran, "$t\bar{t} \rightarrow$ dileptons: The Background Bible." DØ internal note, 1992 (unpublished).

19. F. Paige and S. Protopopescu, "Proceedings: Summer Study on the Physics of Superconducting Supercollider." 323 (1986).

20. P. Grannis *et al.* (DØ Collaboration), "**The DØ detector at the Fermilab Collider.**" Proceedings of Les Contres de Physique de la Vallée d'Aoste, (1987); "DØ design report." DØ internal publication, 1984 (unpublished).

21. H. T. Edwards, *Ann Phys.* **35**, 605 (1985).

22. C. Brown *et al.* (DØ Collaboration), "DØ Muon System with Proportional Drift Tube Chambers." *Nucl. Instr. and Meth.* **A279**, 331 (1989).

23. P. Grannis *et al.* (DØ Collaboration), "Calorimeter Design Report." DØ internal note 512, 1987 (unpublished).

24. M. Abolins *et al.* (DØ Collaboration), "Hadron and Electron Response of Uranium Liquid Argon Calorimeter Modules for the DØ Detector." *Nucl. Instr. and Meth.* **A280**, 36 (1989).

25. A. Clark *et al.* (DØ Collaboration), "The DØ Central Tracking System." *Nucl. Instr. and Meth.* **A279**, 243 (1989).

26. A. Clark *et al.* (DØ Collaboration), "The DØ Vertex Chamber Construction and Test Results." *Nucl. Instr. and Meth.* 1992 (to be published).

27. M. Utes and M. Matulik, "The Vertex Pad Oscillation Investigation." DØ internal note 1182, 1991. (unpublished).

28. J-F. Detoeuf *et al.* (DØ Collaboration), "The DØ Transition Radiation Detector." *Nucl. Instr. and Meth.* **A265**, 157 (1988).

29. J-F Detoeuf *et al.* (DØ Collaboration), "Status of the Transition Radiation Detector for the DØ Experiment." *Nucl. Instr. and Meth.* **A279**, 310 (1989).

30. F. Feinstein, Ph.D. thesis, Univ Paris Sud, France, 1987 (unpublished).

31. A.G. Frodesen *et al.*, **"Probability and Statistics in Particle Physics."** (Columbia University Press, New York, 1979).

32. T. Behnke, Ph.D. thesis, State University of New York, Stony Brook, 1989 (unpublished).

33. D. Pizzuto, Ph.D. thesis, State University of New York, Stony Brook, 1991 (unpublished).

34. F. Sauli, "Principles of Operation of Multiwire Proportional and Drift Chambers." ATP lectures, CERN-EP 77-09 (1977).

35. D. Buchholz *et al.* (DØ Collaboration), "The use of Waveform Digitizers with Drift Chambers for DØ." *Nucl. Instr. and Meth.* **A257**, 556 (1987).

36. R. J. Yarema, "A new Preamplifier for Particle Detectors." *IEEE Trans. Nucl. Sci.* **NS33**, 933 (1986); FNAL PUB TM-1284, (1984).

37. D. Buchholz *et al.* (DØ Collaboration), "Comparison of Two Fujitsu Preamps." DØ internal note 357, 1986 (unpublished).

38. M. Rijssenbeek, "The Fujitsu MB43458 Quad Charge Amplifier." DØ internal note 563, 1987 (unpublished).

39. D. Howard, "Shaper Circuit Specification." DØ internal note, 1988 (unpublished).

40. M. Johnson *et al.* (DØ Collaboration), "A working, VME based, 106-MHz FADC Data Acquisition System for the Tracking Detectors at DØ." FERMILAB-CONF-91-350, (1991).

41. D. DeGroot, "DØ Central Tracking Zero Suppression Circuit Specification." DØ internal note 1013, 1988 (unpublished).

42. M. Shea *et al.*, "The DØ Downloading and Control System." Proceedings, Control systems for experimental physics, Villars (1987).

43. M. Utes, "DØ Central Tracking FADC Controller Module." DØ internal note 962, 1990 (unpublished).

44. K. McFarland, "Design and Testing of a Calibration System for the Level Ø Trigger at DØ." DØ internal note 840, 1989 (unpublished).

45. M. Abolins *et al.* (DØ Collaboration), "A High Luminosity Trigger Design for the Tevatron Collider Experiment in DØ." *IEEE Trans. Nucl. Sci.* **36**, 384 (1989).

46. M. Abolins *et al.* (DØ Collaboration), "The Fast Trigger for the DØ Experiment." *Nucl. Instr. and Meth.* **A289**, 543 (1990).

47. D. Cutts *et al.* (DØ Collaboration), "DØ Data Acquisition: High Speed Data Paths for DØ." DOE-ER-03130-53-mc, (April 1990).

48. D. Cutts *et al.* (DØ Collaboration), "A Microprocessor Farm Architecture for High Speed Data Acquisition and Analysis." *IEEE Trans. Nucl. Sci.* **36**, 738 (1989).

49. Digital Equipment Corporation, Maynard, Massachusetts.

50. R. Avery *et al.*, "Results of TØ Studies." DØ internal note, 1992 (unpublished).

51. R. Lipton, "1990 Test Beam Performance and Studies." DØ internal note 1076, 1991 (unpublished).

52. R. Fernow, **"Introduction to Experimental Particle Physics."** (Cambridge University Press, 1986).

53. P. Bhat, "Proposed NW Beamline Upgrade for DØ Test Beam Load-2." DØ internal note 1104, 1991 (unpublished).

54. J. Bantly, Ph.D. thesis, Northwestern University, 1992 (unpublished).

55. J. Va'vra, "High Resolution Drift Chambers." CERN EF/84-17, (1984).

56. A. H. Walenta *et al.* (Brookhaven Natl. Lab.), "Measurement of Ionization Loss in the Region of Relativistic Rise for Noble and Molecular Gases." *Nucl. Instr. and Meth.* **A161**, 45 (1979).

57. R. Tilden and M. Utes, "The Canary Prescaler Card." DØ internal note 1066, 1990 (unpublished).

58. Particle data group, "Review of Particle Properties." *Phys. Lett.* **B239**, III.13 (1990).

59. W. Allison and J. Cobb, "Relativistic Charged Particle Identification by Energy Loss." *Annual Review of Nuclear and Particle Science.* **30**, 253 (1980).

60. F. Lapique and F. Piuz, "Simulation of the Measurement by Primary Cluster Counting of the Energy Lost by a Relativistic Ionizing Particle in Argon." *Nucl. Instr. and Meth.* **175**, 297 (1980).

61. G. Lynch, "Measurement of Energy Loss in TPC." TPC-LBL 81-6, 903 (1981).

62. H. Maccabee and D. Papworth, *Phys. Lett.* **A30**, 241 (1969).

63. M. Shapiro, Ph.D. thesis, Lawrence Berkeley Laboratory, LBL-18820 1984.

64. R. Brun *et al.*, "**GEANT3.**" Fermilab Pub. DD/EE/84-1, (1987).

65. Q. Li and R. Raja, "DØ GEANT: Overview and Detector Simulation." DØ internal note, 1990 (unpublished).

66. N. Graf, (private communication).

67. C. Klopfenstein, (private communication).

DATE
FILMED
5/16/94
END